

---

# TAO GENERAL DIFFERENTIAL AND DIFFERENCE: THEORY AND APPLICATION

---

Linmi Tao\*✉, Ruiyang Liu\*, Donglai Tao, Wu Xia, Feilong Ma, Jingmao Cui

Department of Computer Science and Technology, BNRist, Tsinghua University  
Key Lab of Pervasive Computing, Ministry of Education of China  
Beijing 100084, China

\*Co-first author.

✉Corresponding author. E-mail: linmi@tsinghua.edu.cn

## ABSTRACT

Modern numerical analysis is executed on discrete data, of which numerical difference computation is one of the cores and is indispensable. Nevertheless, difference algorithms have a critical weakness in their sensitivity to noise, which has long posed a challenge in various fields including signal processing. Difference is an extension or generalization of differential in the discrete domain. However, due to the finite interval in discrete calculation, there is a failure in meeting the most fundamental definition of differential, where  $dy$  and  $dx$  are both infinitesimal (Leibniz) or the limit of  $dx$  is 0 (Cauchy). In this regard, the generalization of differential to difference does not hold. To address this issue, we depart from the original derivative approach, construct a finite interval-based differential, and further generalize it to obtain the difference by convolution. Based on this theory, we present a variety of difference operators suitable for practical signal processing. Experimental results demonstrate that these difference operators possess exceptional signal processing capabilities, including high noise immunity.

**Keywords** Numerical Analysis · Signal Processing · Differential/Difference-by-Convolution

**Contents**

<b>1</b>	<b>Tao General Differential</b>	<b>3</b>
1.1	Tao Derivative . . . . .	3
1.2	Tao General Differential: Differential-by-Convolution . . . . .	5
1.3	Tao General Differential Operator . . . . .	9
1.3.1	Linear Kernel Function . . . . .	9
1.3.2	Exponential Kernel Function . . . . .	10
1.3.3	Gaussian Kernel Function . . . . .	11
1.3.4	Landau Kernel Function . . . . .	12
1.3.5	Weibull Kernel Function . . . . .	12
1.3.6	Fourier Transform Verification . . . . .	13
1.4	TGD Calculation Examples . . . . .	13
1.5	Constraints and Counterexamples . . . . .	14
<b>2</b>	<b>Tao General Differential of Multivariate Function</b>	<b>20</b>
2.1	Directional Derivative of Multivariate Function . . . . .	20
2.2	Directional TGD and Rotational Construction Method . . . . .	20
2.3	Rotational Constructed 2D Directional TGD Operators . . . . .	21
2.4	Partial TGD and Orthogonal Construction Method . . . . .	25
2.5	2D TGD Calculation Examples . . . . .	27
<b>3</b>	<b>Tao General Difference of Discrete Signal</b>	<b>33</b>
3.1	One-Dimensional Discrete TGD . . . . .	33
3.2	One-Dimensional Discrete TGD Operators . . . . .	36
3.3	High-Dimensional Discrete TGD and Operators . . . . .	38
<b>4</b>	<b>The Application of TGD in Signal Denoise</b>	<b>45</b>
4.1	TGD-Based Signal Denoise Algorithm . . . . .	45
4.2	Experiments and Analysis . . . . .	47
4.2.1	Qualitative Experiments . . . . .	47
4.2.2	Quantitative Experiments . . . . .	51
4.2.3	Ablation Experiments . . . . .	53
<b>5</b>	<b>The Application of TGD in Computer Vision</b>	<b>56</b>
5.1	First-order TGD-based Image Edge Detection . . . . .	57
5.2	Second-order TGD-based Image Edge Detection . . . . .	60
5.3	TGD-based 3D Edge Detection . . . . .	63
<b>6</b>	<b>Conclusion and Outlook</b>	<b>70</b>

## 1 Tao General Differential

In the Calculus, the derivative is defined as the limit:

$$f'(x_0) = \lim_{\Delta x \rightarrow 0} \frac{f(x_0 + \Delta x) - f(x_0)}{\Delta x}. \quad (1)$$

Formula (1) depicts properties of smooth functions, but fails on non-smooth functions that are commonly observed in real systems. Consequently, various types of generalized derivatives have been proposed to describe the properties of these non-smooth functions [1, 2, 3, 4, 5]. These generalized derivatives are equivalent to the traditional derivative  $f'(x_0)$  at each differentiable point  $x_0$  of the function  $f$ . And, for other points that the derivative cannot deal with, the generalized derivatives provide a set of scalars or vectors that depict the change in  $f(x)$  at non-differentiable points. Typically, Lanczos proposed “differentiation-by-integration” and introduced Lanczos Derivative (LD) in the following form [3, 4, 5]:

$$\begin{aligned} f'_{\text{LD}}(x_0) &= \lim_{W \rightarrow 0} \frac{3}{2W^3} \int_{-W}^W t f(x_0 + t) dt \\ &= \lim_{W \rightarrow 0} \frac{3}{2W^3} \left( \int_0^W t f(x_0 + t) dt - \int_0^W t f(x_0 - t) dt \right) \end{aligned} \quad (2)$$

Teruel further extended LD by substituting  $t$  with  $t^k$  in Formula (2), and giving a new class of LD [6]:

$$\begin{aligned} f'_{\text{LD}}(x_0; k) &= \lim_{W \rightarrow 0} \frac{k+2}{2W^{k+2}} \int_{-W}^W t^k f(x_0 + t) dt \quad \{k = 2a + 1 \mid a \in \mathbf{Z}^+\} \\ &= \lim_{W \rightarrow 0} \frac{k+2}{2W^{k+2}} \left( \int_0^W t^k f(x_0 + t) dt - \int_0^W t^k f(x_0 - t) dt \right) \end{aligned} \quad (3)$$

Hicks proposed that the approximation of LD can be seen as averaging the derivative over a small marginal interval  $[x_0 - W, x_0 + W]$  around the point of differentiation  $x_0$  [7]. This average might be understood as a weighted average with a weight function  $w$ :

$$\begin{aligned} f'(x_0) &\approx \lim_{W \rightarrow 0} \int_{-W}^W w(t) f'(x_0 + t) dt \\ \text{where } &\int_{-W}^W w(t) dt = 1 \text{ and } w(t) > 0. \end{aligned} \quad (4)$$

Following Hicks, Liptaj presented some interesting non-analytic weight functions for LD [8].

From Leibniz to Lanczos, then Liptaj, the evolution of the Calculus is evident in its progressive development and perfection over the centuries. Nonetheless, this perfect theory is unsuitable for modern numerical computation. In discrete systems, numerical computation occurs within a finite interval, which renders Calculus’s foundations of infinitesimal and limit unsuitable. To address this issue, this paper transcends the bound of infinitesimal and limit to develop a theory of derivative and difference on a finite interval. This theory propels the Calculus toward modern numerical computation.

### 1.1 Tao Derivative

Here, we propose that  $t^k$  in extended LD can be further extended by a family of function  $w(t)$  with a parameter  $W > 0$  that satisfies the following **Normalization Constraint (C1)**:

$$\begin{cases} \int_0^W w(t) dt = 1 \\ w(t) > 0 & t \in (0, W] \\ w(t) = 0 & t \in (-\infty, 0] \cup (W, +\infty) \end{cases} \quad (5)$$

Furthermore, we define a new generalized derivative, **Tao Derivative (TD)**, of any Lebesgue integrable function  $f$  as:

$$f'_{\text{TD}}(x_0; w, W) \triangleq \lim_{W \rightarrow 0} \frac{\int_0^W f(x_0 + t)w(t) dt - \int_0^W f(x_0 - t)w(t) dt}{2 \int_0^W tw(t) dt}. \quad (6)$$

Noticing that Formula (2) and (3) can be obtained by specifying  $w(t)$  with  $2t/W^2$  and  $(k+1)t^k/W^{k+1}$ , respectively. Thus, TD defined by Formula (6) is the general form of LD.

$$\begin{aligned} f'_{\text{TD}}(x_0; \frac{2t}{W^2}, W) &= f'_{\text{LD}}(x_0) \\ f'_{\text{TD}}(x_0; \frac{(k+1)t^k}{W^{k+1}}, W) &= f'_{\text{LD}}(x_0; k) \end{aligned} \quad (7)$$

It is proved that, at each differentiable point  $x_0$  of  $f$ , the TD result of Formula (6) is equivalent to the traditional derivative specified in Formula (1).

**Theorem 1.** *Suppose that  $f$  is a  $C^1$  continuous function defined on a neighborhood of point  $x_0$ , and  $w(t)$  is a function satisfying Normalization Constraint (Formula (5)) with a parameter  $W > 0$ .  $f'_{\text{TD}}(x_0; w, W)$  given by Formula (6) equals to  $f'(x_0)$  given by Formula (1).*

*Proof.*

$$\begin{aligned} f'_{\text{TD}}(x_0; w, W) &= \lim_{W \rightarrow 0} \frac{\int_0^W f(x_0 + t)w(t) dt - \int_0^W f(x_0 - t)w(t) dt}{2 \int_0^W tw(t) dt} \\ &= \lim_{W \rightarrow 0} \frac{\int_0^W (f(x_0 + t) - f(x_0 - t))w(t) dt}{2 \int_0^W tw(t) dt} \quad (\text{Taylor's Formula}) \\ &= \lim_{W \rightarrow 0} \frac{\int_0^W ((f(x_0) + tf'(x_0) + O(t^2)) - (f(x_0) - tf'(x_0) + O(t^2)))w(t) dt}{2 \int_0^W tw(t) dt} \\ &= \lim_{W \rightarrow 0} \frac{\int_0^W (2tf'(x_0))w(t) dt}{2 \int_0^W tw(t) dt} \\ &= f'(x_0) \lim_{W \rightarrow 0} \frac{2 \int_0^W tw(t) dt}{2 \int_0^W tw(t) dt} \\ &= f'(x_0). \end{aligned}$$

□

The Leibniz Rule of differentiation is applicable to TD as well. Specifically, the following theorem holds:

**Theorem 2.** *Suppose that  $f$  and  $g$  are both  $C^1$  continuous functions defined on a neighborhood of point  $x_0$ , and  $w(t)$  is a function satisfying Normalization Constraint (Formula (5)) with a parameter  $W > 0$ . We have  $(f \cdot g)'_{\text{TD}}(x_0; w, W) = f'(x_0)g(x_0) + g'(x_0)f(x_0)$ , or in short,  $(f \cdot g)'_{\text{TD}} = f'g + g'f$ .*

*Proof.* According to Taylor's Formula, for  $f$  and  $g$  on a neighborhood of  $x_0$ ,  $t \in [0, W)$  and  $W \rightarrow 0$ , we have:

$$\begin{aligned} f(x_0 + t) &= f(x_0) + tf'(x_0) + O(t^2) \\ g(x_0 + t) &= g(x_0) + tg'(x_0) + O(t^2). \end{aligned} \quad (8)$$

Then:

$$f(x_0 + t)g(x_0 + t) - f(x_0 - t)g(x_0 - t) = 2t(f'g + g'f) + O(t^2). \quad (9)$$

Finally, we can apply Formula (9) to the definition of  $(f \cdot g)'_{\text{TD}}$ :

$$\begin{aligned} (f \cdot g)'_{\text{TD}} &= \lim_{W \rightarrow 0} \frac{\int_0^W f(x_0 + t)g(x_0 + t)w(t) dt - \int_0^W f(x_0 - t)g(x_0 - t)w(t) dt}{2 \int_0^W tw(t) dt} \\ &= \lim_{W \rightarrow 0} \frac{\int_0^W (f(x_0 + t)g(x_0 + t) - f(x_0 - t)g(x_0 - t)) w(t) dt}{2 \int_0^W tw(t) dt} \end{aligned}$$

$$\begin{aligned}
 &= \lim_{W \rightarrow 0} \frac{\left(2 \int_0^W tw(t) dt\right) (f'g + g'f) + O\left(\int_0^W t^3w(t) dt\right)}{2 \int_0^W tw(t) dt} \\
 &= f'g + g'f.
 \end{aligned}$$

□

Combining Theorem 1 and 2, we can immediately get the following corollary:

**Corollary 1.** *Suppose that  $f$  and  $g$  are both  $C^1$  continuous functions defined on a neighborhood of point  $x_0$ , and  $w(t)$  is a function satisfying Normalization Constraint (Formula (5)) with a parameter  $W > 0$ . We have  $(f \cdot g)'_{TD}(x_0; w, W) = f'_{TD}(x_0; w, W)g(x_0) + g'_{TD}(x_0; w, W)f(x_0)$ , or in short,  $(f \cdot g)'_{TD} = f'_{TD}g + g'_{TD}f$ .*

Similarly, we express our second-order Tao Derivative of a Lebesgue integrable function  $f$  as follows:

$$f''_{TD}(x_0; w, W) \triangleq \lim_{W \rightarrow 0} \frac{\int_0^W f(x_0 + t)w(t) dt + \int_0^W f(x_0 - t)w(t) dt - 2f(x_0) \int_0^W w(t) dt}{\int_0^W t^2w(t) dt} \quad (10)$$

where  $w(t)$  is a continuous function with a parameter  $W > 0$ , satisfying the Normalization Constraint given by Formula (5).

It can be further proved that, at each differentiable point  $x_0$  of  $f$ , the second-order TD is equivalent to the traditional second-order derivative of  $f$ .

**Theorem 3.** *Suppose  $f$  is a  $C^2$  continuous function defined on a neighborhood of point  $x_0$ , and  $w(t)$  is a function satisfying Normalization Constraint (Formula (5)) with a parameter  $W > 0$ .  $f''_{TD}(x_0; w, W)$  given by Formula (10) equals to  $f''(x_0)$ , namely*

$$f''(x_0) = \lim_{\Delta x \rightarrow 0} \frac{f'(x_0 + \Delta x) - f'(x_0)}{\Delta x}. \quad (11)$$

*Proof.*

$$\begin{aligned}
 f''_{TD}(x_0; w, W) &= \lim_{W \rightarrow 0} \frac{\int_0^W f(x_0 + t)w(t) dt + \int_0^W f(x_0 - t)w(t) dt - 2f(x_0) \int_0^W w(t) dt}{\int_0^W t^2w(t) dt} \\
 &= \lim_{W \rightarrow 0} \frac{\int_0^W (f(x_0 + t) + f(x_0 - t) - 2f(x_0))w(t) dt}{\int_0^W t^2w(t) dt} \quad (\text{Taylor's Formula}) \\
 &= \lim_{W \rightarrow 0} \frac{\int_0^W (t^2 f''(x_0) + O(t^3))w(t) dt}{\int_0^W t^2w(t) dt} \\
 &= f''(x_0) \lim_{W \rightarrow 0} \frac{\int_0^W t^2w(t) dt}{\int_0^W t^2w(t) dt} \\
 &= f''(x_0).
 \end{aligned}$$

□

## 1.2 Tao General Differential: Differential-by-Convolution

Generalized derivative is intended for the calculation of non-smooth functions with  $W \rightarrow 0$ , and is developed to finite difference [9, 10] for the calculation of the discrete numerical difference in discrete processing. However, in modern discrete systems, discrete signals are produced over a certain time, space, or spatiotemporal interval [11]. In other

words,  $W$  does not tend toward 0. This creates a gap between the theory of generalized derivative and the practice of discrete processing with regard to the derivative interval. It is essential to study differential over a finite interval ( $W > 0$ ) as the basis for establishing difference within that interval, which we call *General Differential* and *General Difference* relatively.

In order to implement differential computation in a certain interval  $[x_0 - W, x_0 + W]$ , we construct first- and second-order **Tao General Differential** (TGD) by extending the integration interval of TD defined in Formula (6) and (10), respectively:

$$f'_{\text{TGD}}(x_0; w, W) \triangleq \frac{\int_0^W f(x_0 + t)w(t) dt - \int_0^W f(x_0 - t)w(t) dt}{2 \int_0^W tw(t) dt} \quad (12)$$

$$f''_{\text{TGD}}(x_0; w, W) \triangleq \frac{\int_0^W f(x_0 + t)w(t) dt + \int_0^W f(x_0 - t)w(t) dt - 2f(x_0) \int_0^W w(t) dt}{\int_0^W t^2w(t) dt} \quad (13)$$

where  $w$  satisfies Normalization Constraint (Formula (5)). Here, we call  $w(t)$  as the *kernel function*, and  $W$  as the *kernel size* of TGD, respectively.

Through the following transformation of Formula (12), it is evident that TGD can be abbreviated to a convolution form:

$$\begin{aligned} f'_{\text{TGD}}(x_0; w, W) &= C_1 \left( \int_{-W}^0 f(x_0 + t)(-w(-t)) dt + \int_0^W f(x_0 + t)w(t) dt \right) \\ &= C_1(T * f)(x_0) \end{aligned} \quad (14)$$

where  $C_1$  is the normalization constant, and  $T(t)$  is defined as the *First-order Tao General Differential Operator* (1st-order TGD operator):

$$C_1 = \frac{1}{2 \int_0^W tw(t) dt} \quad (15)$$

$$T(t) = \begin{cases} w(-t) & -W \leq t < 0, \\ -w(t) & 0 < t \leq W, \\ 0 & \text{otherwise.} \end{cases} \quad (16)$$

Similarly, Formula (13) can also be abbreviated to a convolution form:

$$\begin{aligned} f''_{\text{TGD}}(x_0; w, W) &= C_2 \left( \int_{-W}^W f(x_0 + t)w(|t|) dt - 2f(x_0) \int_0^W w(t) dt \right) \\ &= C_2(R * f)(x_0) \end{aligned} \quad (17)$$

where  $C_2$  is the normalization constant, and  $R(t)$  is defined as the *Second-order Tao General Differential Operator* (2nd-order TGD operator):

$$C_2 = \frac{1}{\int_0^W t^2w(t) dt} \quad (18)$$

$$R(t) = \begin{cases} w(|t|) - 2\delta(t) \int_0^W w(t) dt & -W \leq t \leq W, \\ 0 & \text{otherwise.} \end{cases} \quad (19)$$

where  $\delta$  is Dirac delta function [12].

And it is clear that:

$$\begin{aligned} \int_{-\infty}^{\infty} T(t) dt &= \int_{-W}^W T(t) dt = 0 \\ \int_{-\infty}^{\infty} R(t) dt &= \int_{-W}^W R(t) dt = 0 \end{aligned} \quad (20)$$

which means that for a constant function, its TGD value is constantly 0.

Formula (14) and (17) illustrate the Differential-by-Convolution, which presents a novel definition of *General Differential*. This mode calculates the TGD by convolving the function  $f$  with the operators. Moreover, the linearity of the convolution calculation verifies the linearity of TGD, that is, the TGD of any linear combination of functions equals the same linear combination of the TGD of the functions:

$$\begin{aligned} (af + bg)'_{\text{TGD}} &= af'_{\text{TGD}} + bg'_{\text{TGD}} \\ (af + bg)''_{\text{TGD}} &= af''_{\text{TGD}} + bg''_{\text{TGD}} \end{aligned} \quad (21)$$

where  $a$  and  $b$  are real numbers.

In principle, many functions satisfying Normalization Constraint (Formula (5)) can be applied to TGD. However, the TGD calculation should be stable to the function  $f$  in practice. Specifically, for signal processing, the difference operators should accurately capture changes in signals in the spatiotemporal domain, and have a proper high-frequency response while suppressing noise in the frequency domain. We start with defining the unbiasedness of Tao General Differential, which mathematically describes the requirement that the calculated difference robustly fits the signal change.

**Definition 1.** (*Unbiasedness of TGD*)  $f'_{\text{TGD}}$  is unbiased within  $W_T$ , if  $\exists W_T > 0$ , s.t.  $\forall W_1, W_2, 0 < W_2 < W_1 \leq W_T$ , for arbitrary  $w_1(t) \in \mathbb{E}_{W_1}$  and  $w_2(t) \in \mathbb{E}_{W_2}$  holds that if  $f'_{\text{TGD}}(x_1; w_2, W_2) > f'_{\text{TGD}}(x_2; w_2, W_2)$  then  $f'_{\text{TGD}}(x_1; w_1, W_1) > f'_{\text{TGD}}(x_2; w_1, W_1)$ .  $\mathbb{E}_W$  denotes the family of suitable kernel functions  $w$  with kernel size  $W$ .

As a necessary condition for preserving the definition of unbiasedness in the differential calculation, we introduce the following constraint for the kernel function  $w(t)$  in TGD.

**Monotonic Constraint (C2):** the kernel function  $w(t)$  is monotonic decreasing within  $(0, W]$ .

**Theorem 4.** *Monotonic Constraint (C2) is the necessary condition for the Unbiasedness of TGD.*

*Proof.* Let  $f(x) = \delta(x)$ , the Dirac delta function [12]. According to Formula (14), for any  $W_1, 0 < W_1 \leq W_T$  and  $w_1 \in \mathbb{E}_{W_1}$  we have

$$\begin{aligned} f'_{\text{TGD}}(x; w_1, W_1) &= C_1(T * \delta)(x) = C_1T(x) \\ &= \begin{cases} C_1w_1(-x) & -W_1 \leq x < 0, \\ -C_1w_1(x) & 0 < x \leq W_1, \\ 0 & \text{otherwise.} \end{cases} \end{aligned} \quad (22)$$

where  $C_1$  is a constant positive number.

Without loss of generosity, we only discuss the case of  $0 < x_2 < x_1 \leq W_1$ . Let  $W_2 = (x_1 + x_2)/2$  and arbitrary  $w_2 \in \mathbb{E}_{W_2}$ , we have  $0 < x_2 < W_2 < x_1 \leq W_1$  and

$$\begin{aligned} f'_{\text{TGD}}(x_2; w_2, W_2) &= -C_2w_2(x_2) < 0 \\ f'_{\text{TGD}}(x_1; w_2, W_2) &= 0 \end{aligned} \quad (23)$$

where  $C_2$  is also a constant positive number. So we have:

$$f'_{\text{TGD}}(x_1; w_2, W_2) > f'_{\text{TGD}}(x_2; w_2, W_2). \quad (24)$$

According to Definition 1, we have:

$$-C_1w_1(x_1) = f'_{\text{TGD}}(x_1; w_1, W_1) > f'_{\text{TGD}}(x_2; w_1, W_1) = -C_1w_1(x_2). \quad (25)$$

Thus  $\forall x_1, x_2, 0 < x_2 < x_1 \leq W_1$  and  $w_1 \in \mathbb{E}_{W_1}, 0 < w_1(x_1) < w_1(x_2)$ , a.k.a.  $w(t)$  is a monotonic decreasing function within  $(0, W]$ .  $\square$

It is mentioned that the kernel function of LD and extended LD are  $2t/W^2$  and  $(k+1)t^k/W^{k+1}$  respectively. Though Normalization Constraint holds, violating Monotonic Constraint shows that they are not suitable for TGD. Contrary, Gaussian function  $G(t; \sigma)$  can fit both Normalization Constraint and Monotonic Constraint when  $t > 0$ , and be a good kernel function of TGD.

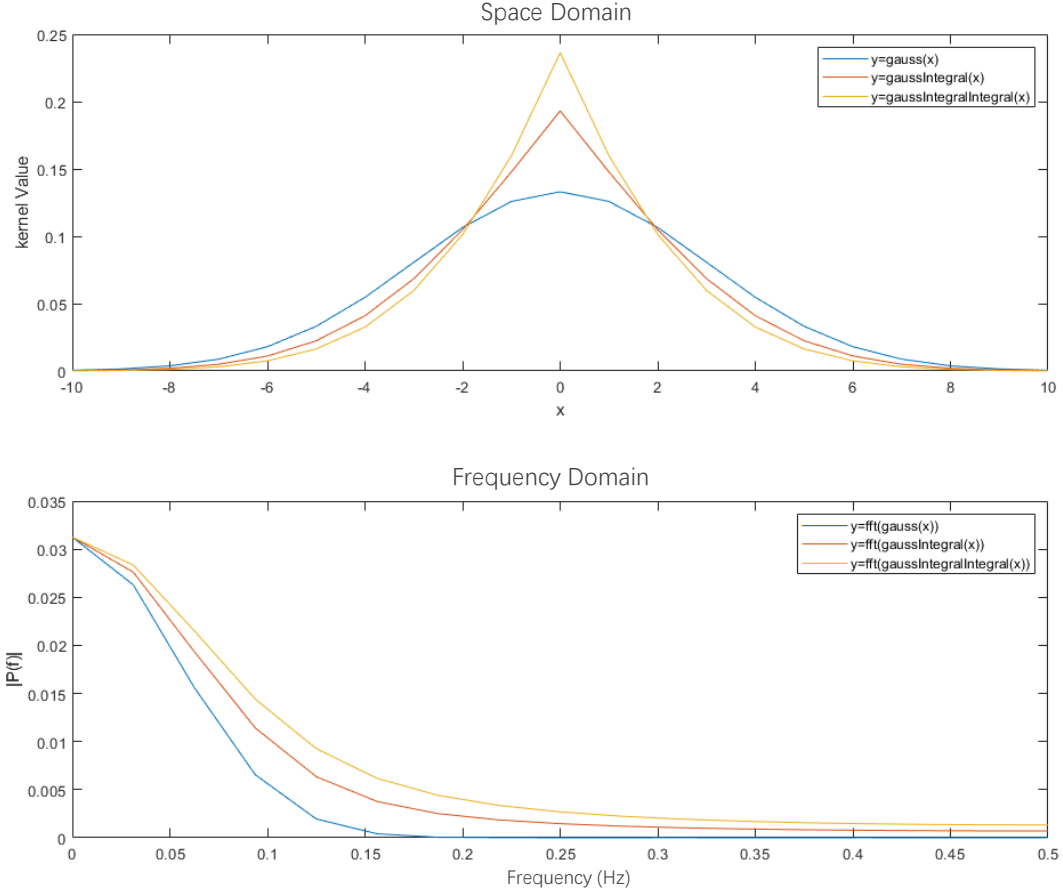


Figure 1: The low-pass filters with high-frequency suppression, the integral and second integral of Gaussian function, as well as their Fourier transform. Notice that the Gaussian filter is presented as a conventional low-pass filter, and all the functions in the figure are normalized to a sum of 1.

In frequency domain, we define the 1st-order smooth operator  $S_T$  and 2nd-order smooth operator  $S_R$  by integrating 1st-order TGD operator  $T$  once and 2nd-order TGD operator  $R$  twice, as follows:

$$\begin{aligned}
 S_T(x) &\triangleq \begin{cases} \int_{-\infty}^x w(-t) dt & x < 0 \\ \int_{-\infty}^0 w(-t) dt + \int_0^x -w(t) dt & x \geq 0 \end{cases} \\
 S_R(x) &\triangleq \begin{cases} \int_{-\infty}^x \left( \int_{-\infty}^u w(-t) dt \right) du & x < 0 \\ \int_{-\infty}^x \left( \int_{-\infty}^0 w(-t) dt + \int_0^u w(t) dt \right) du & x \geq 0 \end{cases}
 \end{aligned} \tag{26}$$

According to the *first fundamental theorem of the calculus*<sup>1</sup> [13, 14], we get both  $S'_T(x)$  and  $S''_R(x)$  when  $x$  is not equal to 0. Noting that  $S'_T(0)$  and  $S''_R(0)$  do not exist. If we add  $S'_T(0) = 0$  and  $S''_R(0) = -2\delta(0)$ , then  $S'_T = T$  and  $S''_R = R$  always hold.

Human visual edge perception benefits from precise localization and robust high-frequency response. People can perceive slope edges and capture fine textures in images, like the text being read, which comprises numerous square

<sup>1</sup>Let  $f$  be a continuous real-valued function defined on a closed interval  $[a, b]$ . Let  $F$  be the function defined, for all  $x$  in  $[a, b]$ , by

$$F(x) = \int_a^x f(t) dt.$$

Then  $F$  is uniformly continuous on  $[a, b]$  and differentiable on the open interval  $(a, b)$ , and  $F'(x) = f(x)$  for all  $x$  in  $(a, b)$ .

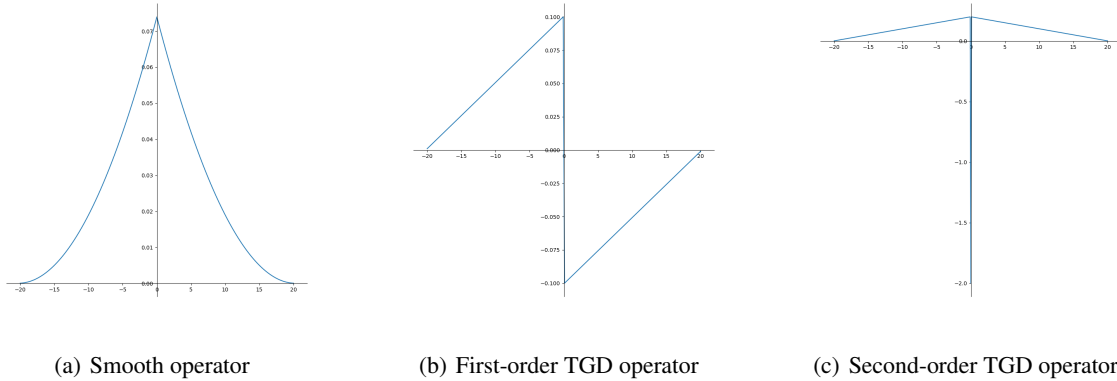


Figure 2: The smooth operator, first- and second-order TGD operators constructed based on the linear kernel function.

wave edges with high spatial frequency. This phenomenon highlights the need for TGD operators that provide a full-frequency response to signals, consistent with the edge detection capability in human vision system.

TGD is proposed for calculating the rate of change in a certain interval, which responds well to the low-frequency components of the function, while suppressing the high-frequency components. To achieve full-frequency response, TGD aims to construct low-pass filters  $S_T$  and  $S_R$  with suppressing in high-frequency instead of a cutoff frequency (Figure 1). This contradiction seems irreconcilable, and the smoothing filters are actually traditionally bad low-pass filters, i.e., low-pass filters with high-frequency leakage. It is characterized by a high cutoff frequency, but the response at the high-frequency end is much smaller than at the low-frequency end. Meanwhile, observations show that the noise energy is generally much smaller compared with signal energy, despite the presence of unavoidable sensor noise in the actual signal. Therefore, the weak high-frequency response in the smoothing filter can both suppress weak high-frequency noise and detect the strong high-frequency signal, achieving a balance. The third constraint that the kernel function  $w(t)$  should meet emerges:

**Full-frequency Constraint (C3): Both  $S_T$  and  $S_R$  are low-pass filters with high frequency suppression.**

It is worth pointing out that if  $S_T$  satisfies the Full-frequency Constraint, then the 2nd-order smooth operator  $S_R$ , whose kernel function  $w$  corresponds to the  $S_T$ , also satisfies the Full-frequency Constraint. Therefore, we concentrate on determining whether  $S_T$  adheres to the Full-frequency Constraint in later sections, and use  $S$  to simplify the representation of  $S_T$ , namely the smooth operator.

In summary, we introduce two constraints that kernel function  $w$  should meet in TGD: Monotonic Constraint in the spatiotemporal domain and Full-Frequency Constraint in the frequency domain. These constraints serve as beneficial supplements to Normalization Constraint. In the following, we first provide examples of specific kernel functions and operators that fulfill all three constraints, and then demonstrate their exceptional performance in signal processing.

### 1.3 Tao General Differential Operator

There are various functions meeting the three constraints we introduce for TGD, which can serve as kernel function  $w$  for constructing TGD operators. Here, we present five representative examples of the kernel function  $w$ .

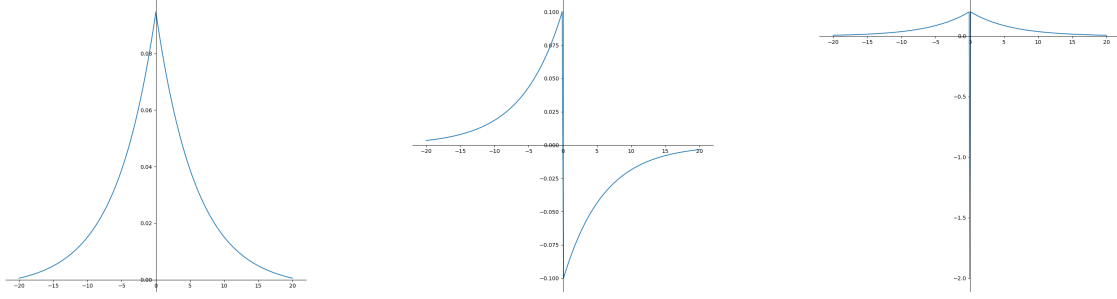
#### 1.3.1 Linear Kernel Function

Linear function is the simplest kernel function (Formula (27)), which is controlled by the parameters  $k$  and  $c$ . The constraints are satisfied when  $k > 0$  and  $c < 0$ . And  $c \lesssim -kW$ , which forces the function value converging to 0 at the window boundary.

$$\text{Line}(x) = -kx - c, \quad x \in (0, W]. \quad (27)$$

By normalization we have:

$$\int_0^W (-kx - c) dx = 1.$$



(a) Smooth operator

(b) First-order TGD operator

(c) Second-order TGD operator

Figure 3: The smooth operator, first- and second-order TGD operators constructed based on the exponential kernel function.

The first- and second-order TGD operators constructed with the linear kernel function are:

$$T_{\text{line}}(x) = \begin{cases} kx - c & x \in [-W, 0) \\ 0 & x = 0 \\ kx + c & x \in (0, W] \end{cases} \quad (28)$$

$$R_{\text{line}}(x) = \begin{cases} -k|x| - c & x \in [-W, 0) \cup (0, W] \\ -2\delta(0) \int_0^W (-kx - c) dx & x = 0 \end{cases} \quad (29)$$

By integrating over the first-order TGD operator, the relative smooth operator is polynomial (Formula (30)), where  $p \gtrsim -\frac{k}{2}W^2 - cW$ , which forces the filter function converging to 0 at the window boundary.

$$S_{\text{line}}(x) = \begin{cases} \frac{k}{2}x^2 - cx + p & x \in [-W, 0) \\ p & x = 0 \\ \frac{k}{2}x^2 + cx + p & x \in (0, W] \end{cases} \quad (30)$$

Figure 2 shows, from left to right, the smooth operator, the first- and second-order TGD operators constructed on the linear kernel function.

### 1.3.2 Exponential Kernel Function

The exponential function can also be used as a kernel function, which is controlled by the parameters  $k$  and  $\delta$ , where  $k > 0, \delta > 0$  (Formula (31)). It has a good property that the exponential kernel function is the same family as its integral, which means the relative smooth operator is also exponential.

$$\text{Exp}(x) = ke^{-|x|/\delta^2}, \quad x \in (0, W]. \quad (31)$$

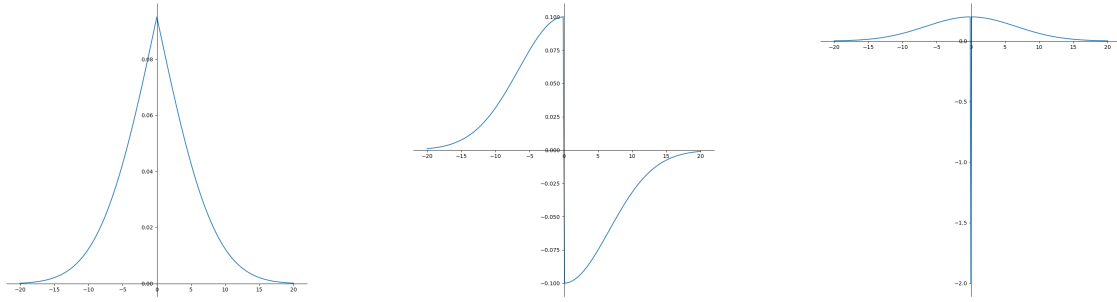
Coefficient  $k$  controls normalization, and by normalization we have:

$$\int_0^W (ke^{-x/\delta^2}) dx = 1.$$

The first- and second-order TGD operators constructed with exponential function are:

$$T_{\text{exp}}(x) = \begin{cases} ke^{-|x|/\delta^2} & x \in [-W, 0) \\ 0 & x = 0 \\ -ke^{-|x|/\delta^2} & x \in (0, W] \end{cases} \quad (32)$$

$$R_{\text{exp}}(x) = \begin{cases} ke^{-|x|/\delta^2} & x \in [-W, 0) \cup (0, W] \\ -2\delta(0) \int_0^W (ke^{-x/\delta^2}) dx & x = 0 \end{cases} \quad (33)$$



(a) Smooth operator

(b) First-order TGD operator

(c) Second-order TGD operator

Figure 4: The smooth operator, first- and second-order TGD operators constructed based on the Gaussian kernel function.

The integral of an exponential function is still an exponential function, which follows that the corresponding smooth operator is exponential, as follows, where  $a, b, p$  are the parameters.

$$S_{\text{exp}}(x) = \begin{cases} ae^{-b|x|} + p & x \in [-W, 0) \\ a + p & x = 0 \\ ae^{-b|x|} + p & x \in (0, W] \end{cases} \quad (34)$$

Figure 3 shows, from left to right, the smooth operator, the first- and second-order TGD operators constructed on the exponential kernel function.

### 1.3.3 Gaussian Kernel Function

Gaussian function itself does not satisfy the Full-frequency Constraint when used as a smooth operator, and its first- as well as second-order derivatives cannot be used as the kernel function of TGD. However, Gaussian function with mean value 0 can be used as a kernel function (Formula (35)), which is controlled by the parameters  $k$  and  $\delta$ , where  $k > 0$  and  $\delta > 0$ . Usually,  $W = 3\delta$  is taken so as to contain more than 97% of the information of the Gaussian.

$$\text{Gaussian}(x) = ke^{-x^2/2\delta^2}, \quad x \in (0, W]. \quad (35)$$

Coefficient  $k$  controls normalization, and by normalization we have:

$$\int_0^W (ke^{-x^2/2\delta^2}) dx = 1.$$

The first- and second-order TGD operators constructed with Gaussian function are:

$$T_{\text{gaussian}}(x) = \begin{cases} ke^{-x^2/2\delta^2} & x \in [-W, 0) \\ 0 & x = 0 \\ -ke^{-x^2/2\delta^2} & x \in (0, W] \end{cases} \quad (36)$$

$$R_{\text{gaussian}}(x) = \begin{cases} ke^{-x^2/2\delta^2} & x \in [-W, 0) \cup (0, W] \\ -2\delta(0) \int_0^W (ke^{-x^2/2\delta^2}) dx & x = 0 \end{cases} \quad (37)$$

The integral of the Gaussian function is the error function of Gaussian, denoted by  $\text{erf}(x)$ . And the smooth operator can be expressed as:

$$S_{\text{gaussian}}(x) = \begin{cases} k(1 + \text{erf}(x/\sqrt{2}\delta)) & x \in [-W, 0) \\ k & x = 0 \\ k(1 - \text{erf}(x/\sqrt{2}\delta)) & x \in (0, W] \end{cases} \quad (38)$$

Figure 4 shows, from left to right, the smooth operator, the first- and second-order TGD operators constructed on the Gaussian kernel function.

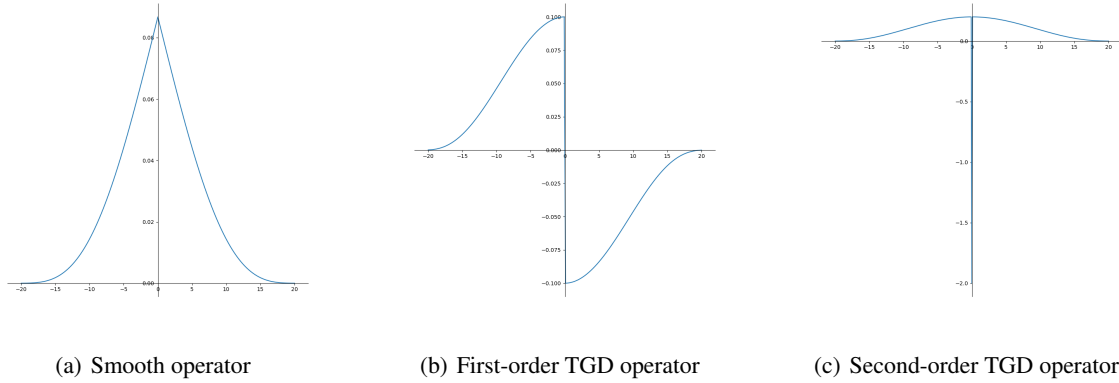


Figure 5: The smooth operator, first- and second-order TGD operators constructed based on the Landau kernel function.

### 1.3.4 Landau Kernel Function

In fact, many classic kernel functions can be used in TGD. Landau kernel function is a classic function used to prove Weierstrass approximation theorem [15]. In Landau function (Formula (39)),  $c, \tau, n$  are the parameters, in which  $\tau \gtrsim W$  is designed to ensure the function follows the constraints of TGD.

$$\text{Landau}(x) = c(1 - x^2/\tau^2)^n, \quad x \in (0, W). \quad (39)$$

Coefficient  $c$  controls normalization. And by normalization we have:

$$\int_0^W (c(1 - x^2/\tau^2)^n) dx = 1.$$

The first- and second-order TGD operators constructed with Landau kernel function are:

$$T_{\text{landau}}(x) = \begin{cases} c(1 - x^2/\tau^2)^n & x \in [-W, 0) \\ 0 & x = 0 \\ -c(1 - x^2/\tau^2)^n & x \in (0, W] \end{cases} \quad (40)$$

$$R_{\text{landau}}(x) = \begin{cases} c(1 - x^2/\tau^2)^n & x \in [-W, 0) \cup (0, W] \\ -2\delta(0) \int_0^W (c(1 - x^2/\tau^2)^n) dx & x = 0 \end{cases} \quad (41)$$

Although it is difficult to write expressions for the integration of Landau kernel, we can approximate the smooth operator by using numerical integration and symmetric transformation.

$$S_{\text{landau}}(x) = \begin{cases} \int_{-W}^x (c(1 - t^2/\tau^2)^n) dt & x \in [-W, 0] \\ S_{\text{landau}}(-x) & x \in (0, W] \end{cases} \quad (42)$$

Figure 5 shows, from left to right, the smooth operator, the first- and second-order TGD operators constructed on the Landau kernel function.

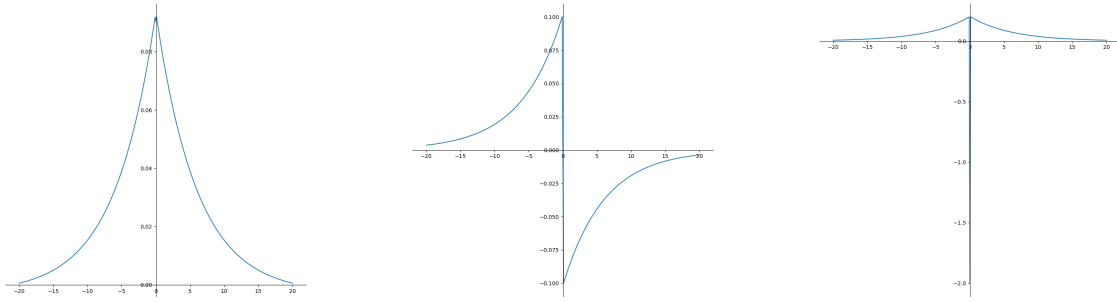
### 1.3.5 Weibull Kernel Function

In addition to the aforementioned kernel functions, TGD can also use probability density functions as kernel functions, which are usually integrable and finite in energy. Besides Gaussian, we provide an additional example, the Weibull distribution function [16, 17], with its parameters  $k$  and  $\lambda$ . When  $k \in (0, 1]$ , Weibull distribution functions satisfy the constraints and are used as the kernel function of TGD.

$$\text{Weibull}(x) = \frac{ck}{\lambda} \left(\frac{x}{\lambda}\right)^{k-1} e^{-\left(\frac{x}{\lambda}\right)^k}, \quad x \in (0, W], k \in (0, 1]. \quad (43)$$

Coefficient  $c$  controls normalization. And by normalization we have:

$$\int_0^W \left(\frac{ck}{\lambda} \left(\frac{x}{\lambda}\right)^{k-1} e^{-\left(\frac{x}{\lambda}\right)^k}\right) dx = 1.$$



(a) Smooth operator

(b) First-order TGD operator

(c) Second-order TGD operator

Figure 6: The smooth operator, first- and second-order TGD operators constructed based on the Weibull distribution.

The first- and second-order TGD operators constructed with Weibull distribution function are:

$$T_{\text{weibull}}(x) = \begin{cases} \frac{ck}{\lambda} \left(-\frac{x}{\lambda}\right)^{k-1} e^{-\left(-\frac{x}{\lambda}\right)^k} & x \in [-W, 0) \\ 0 & x = 0 \\ -\frac{ck}{\lambda} \left(\frac{x}{\lambda}\right)^{k-1} e^{-\left(\frac{x}{\lambda}\right)^k} & x \in (0, W] \end{cases} \quad (44)$$

$$R_{\text{weibull}}(x) = \begin{cases} \frac{ck}{\lambda} \left(\frac{|x|}{\lambda}\right)^{k-1} e^{-\left(\frac{|x|}{\lambda}\right)^k} & x \in [-W, 0) \cup (0, W] \\ -2\delta(0) \int_0^W \left(\frac{ck}{\lambda} \left(\frac{x}{\lambda}\right)^{k-1} e^{-\left(\frac{x}{\lambda}\right)^k}\right) dx & x = 0 \end{cases} \quad (45)$$

The smooth operator can be obtained by approximation using numerical integration and symmetric transformation.

$$S_{\text{weibull}}(x) = \begin{cases} \int_{-W}^x \left(\frac{ck}{\lambda} \left(\frac{|t|}{\lambda}\right)^{k-1} e^{-\left(\frac{|t|}{\lambda}\right)^k}\right) dt & x \in [-W, 0] \\ S_{\text{weibull}}(-x) & x \in (0, W] \end{cases} \quad (46)$$

Figure 6 shows, from left to right, the smooth operator, the first- and second-order TGD operators constructed on the Weibull distribution.

### 1.3.6 Fourier Transform Verification

The five kernel functions we introduced already satisfy both the Normalization Constraint and the Monotonic Constraint. Fourier transform analysis (Figure 7) reveals that their smooth operators have a full-frequency response or higher cut-off frequencies compared to the Gaussian smooth operator of the same kernel width. Additionally, these smooth operators have a much smaller response in the high-frequency range, compared to the low-frequency range, indicating adherence to the Full-frequency Constraint.

## 1.4 TGD Calculation Examples

We visualize the TGD calculations of smooth and non-smooth functions to provide an intuitive understanding of TGD. In these experiments, we utilize the Gaussian kernel function and its corresponding TGD operators.

Figure 8.a and 8.b demonstrate the traditional derivative and TGD results for smooth continuous signals, such as Sine and Gaussian functions, respectively. Despite the difference in their respective values, the derivative and TGD results show a positive relationship, which is a good embodiment of *Unbiasedness*. Figure 8.c and 8.d depict the outcomes where a small amount of Gaussian noise is added to the original function, which is barely perceptible to the human eye. It is observed that the traditional derivative is significantly distorted by the added noise, whereas TGD, computed over a certain interval, exhibits strong noise suppression capabilities.

We further extend our analysis from smooth functions to non-smooth functions, such as the square-wave and slope signals, which commonly occur in discrete systems. Figure 9 compares the derivative and TGD results. For the square-wave signal, the derivative values are absent or infinite at the edges of the square-wave and zero elsewhere, resulting in the visualization of two impulse signals. TGD characterizes this variation as meaningful finite values, and

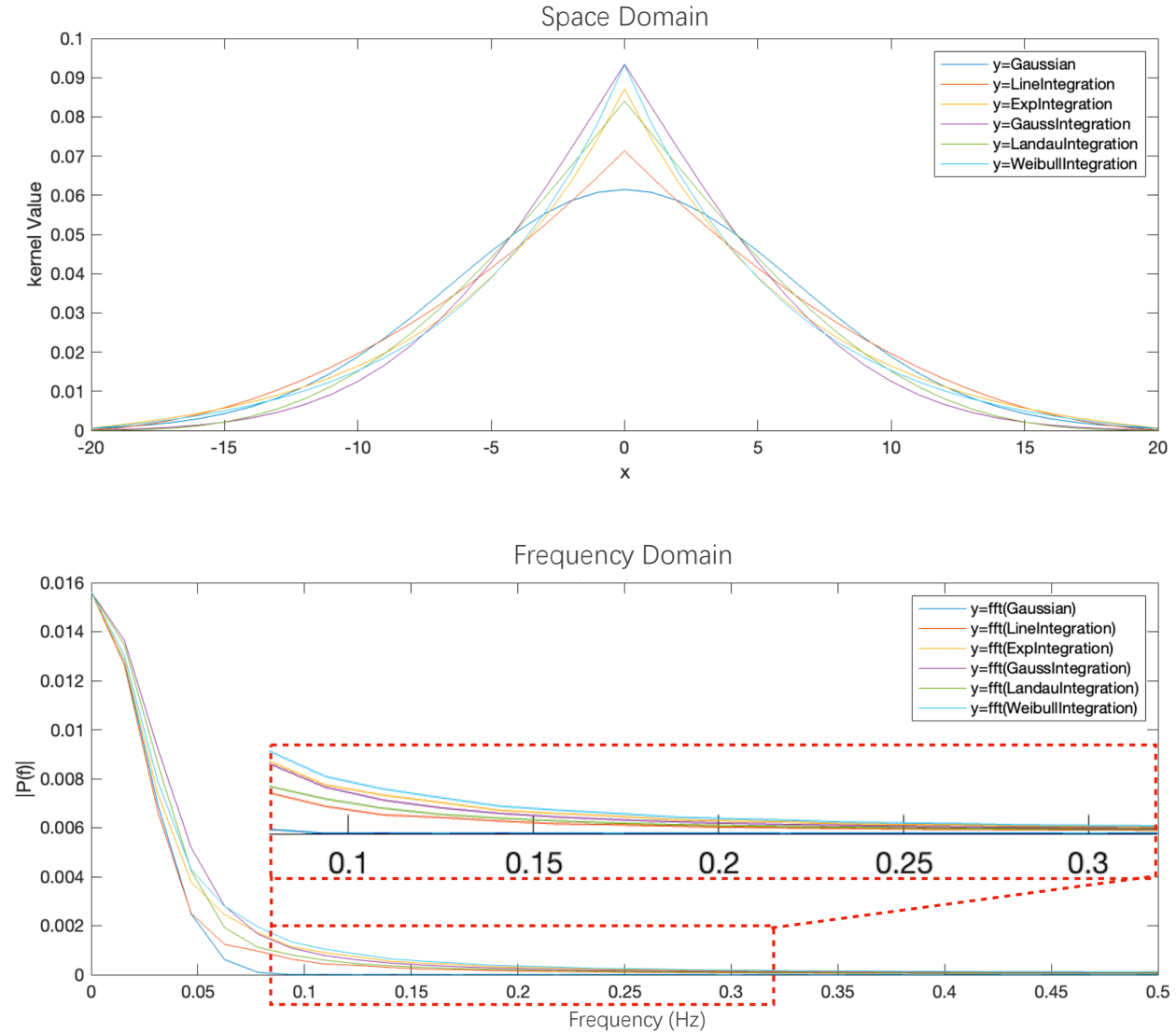


Figure 7: Comparison of Gaussian smooth operator with smooth operators generated by the introduced five kernel functions, as well as their Fourier transform. The introduced smooth operators all have a higher cut-off frequency than Gaussian, and the response of the high-frequency part is much smaller than the low-frequency part.

the extreme points of TGD align with the edges of the square-wave, where the signal changes fastest. For the slope signal, the derivatives are constant within a certain range, whereas TGD indicates the center of the ramp as the point of maximum TGD value. To test their noise resistance, We intentionally add a small amount of noise to both signals. While the traditional finite derivative method is sensitive to noise, TGD demonstrates robustness against it (Figure 9.c and 9.d).

These experiments demonstrate that TGD can effectively characterize the change rate of non-smooth functions with high stability and noise tolerance. And TGD exhibits a remarkable capability to capture signal changes.

### 1.5 Constraints and Counterexamples

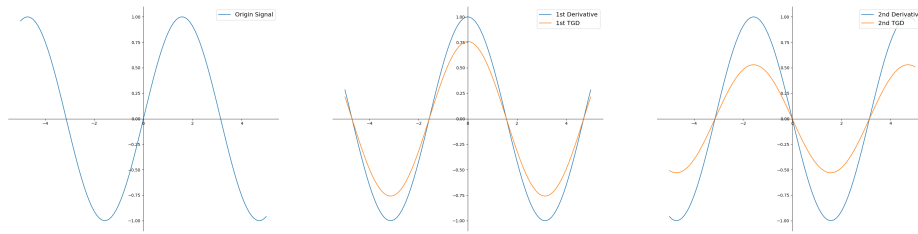
Although TGD operators that satisfy the proposed constraints have demonstrated superior properties in differential calculations, we present a few counterexamples for a better understanding of the constraints.

As the first counterexample, we remove the limit symbol in Lanczos Derivative (Formula (2)). Lanczos employs  $w(t) = 2t/W^2$  as the kernel function, which is a single-increasing function on  $(0, W]$  and does not meet the Monotonic

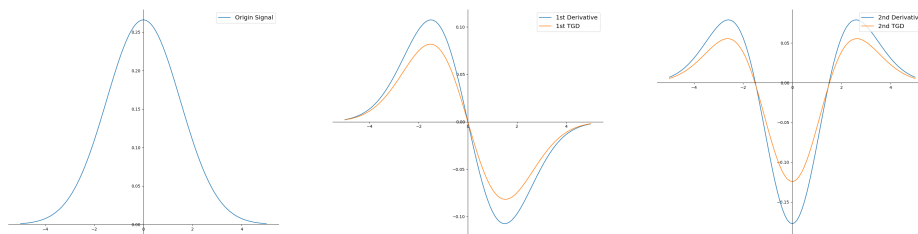
Constraint. Figure 10.a displays the corresponding 1st-order TGD operator and smooth operator when choosing  $w(t) = 2t/W^2$  as the kernel function.

As the second counterexample, we consider Gaussian filtering and differential calculation, which is a conventional technique in signal processing. In Figure 1, we have emphasized that the Gaussian filter is a low-pass filter and fails to satisfy the Full-Frequency Constraint. This indicates that the first- and second-order derivatives of Gaussian are not suitable as a kernel function of TGD. Additionally, Figure 10.b displays the corresponding 1st-order TGD operator and smooth operator when choosing the first- and second-order derivatives of Gaussian as the kernel function.

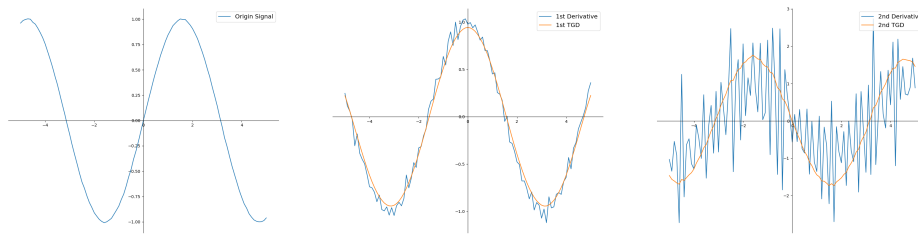
Figure 11 compares the outcomes calculated for a single square-wave signal and a continuous square-wave signal. Notably, when considering a single square-wave signal, the extreme points of both Extend LD and Gaussian-Smooth-Difference fail to determine the edges of the square-wave. Hence, their way of detecting signal changes is incorrect. This error worsens when working with continuous square-wave signals. the LD method severely violates Monotonic Constraint and causes significant shifts in extreme points. On the other hand, Gaussian smoothing amalgamates high-frequency signals, compromising the identification of high-frequency variations and ultimately detecting changes only at two ends of the signal. In contrast, TGD meets both the Monotonic and Full-Frequency Constraints, and accurately identifies and locates high-frequency changes. Therefore, TGD can provide a reliable representation of signal changes that constitutes a stable foundation for various gradient-based downstream tasks in signal processing.



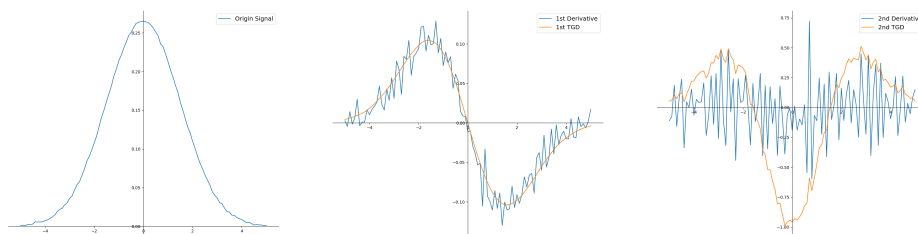
(a) Sin signal



(b) Gaussian signal

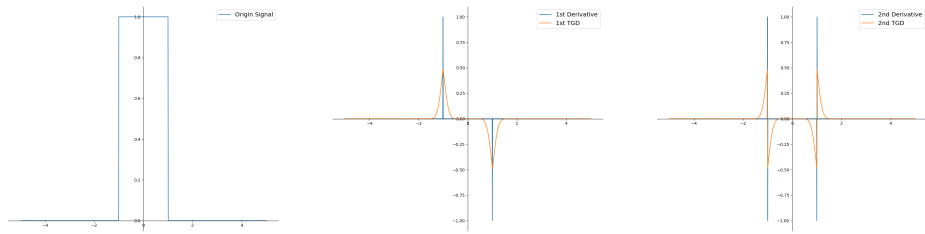


(c) Sin signal with noise

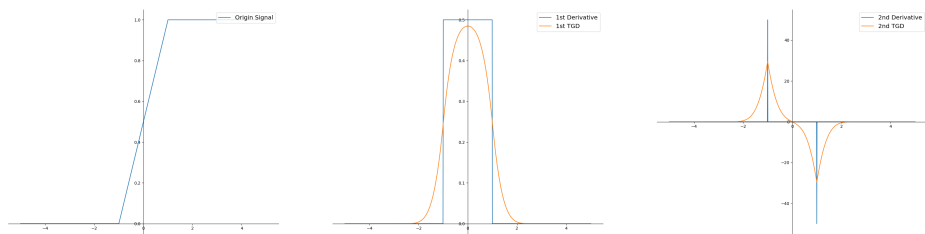


(d) Gaussian signal with noise

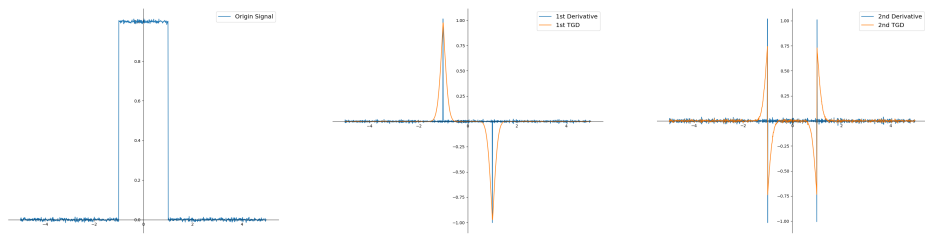
Figure 8: Comparison of derivative and TGD results of smooth continuous signal and noise signal. From left to right, the origin signal, the first-order derivative (blue) and TGD (orange), the second-order derivative (blue) and TGD (orange). For better visualization, we have scaled the TGD results.



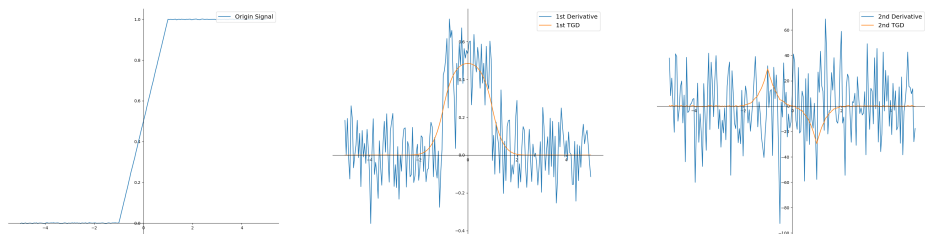
(a) Square-wave signal



(b) Slope signal

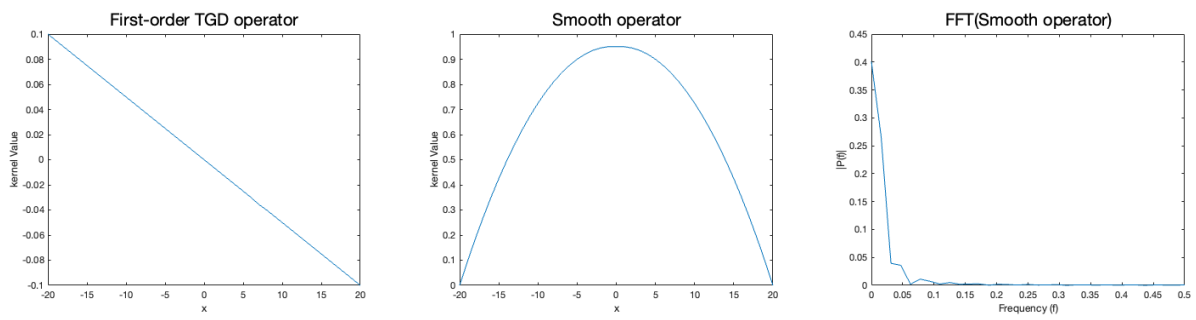


(c) Square-wave signal with noise

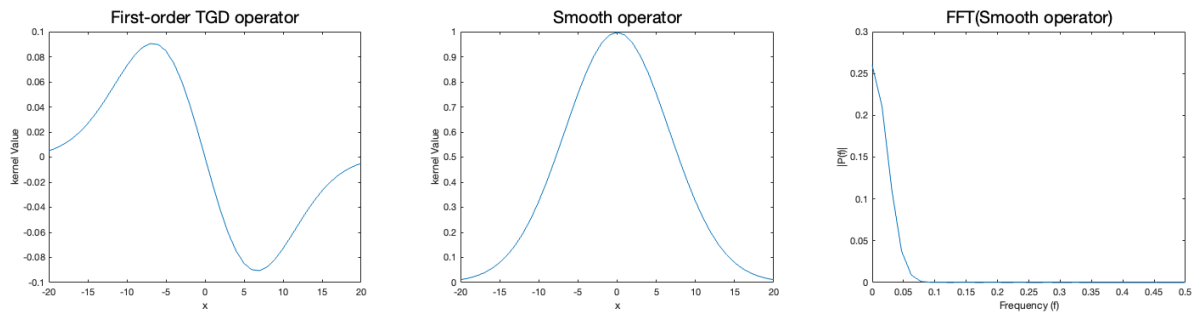


(d) Slope signal with noise

Figure 9: Comparison of derivative and TGD results of non-smooth continuous signal and noise signal. From left to right, the origin signal, the first-order derivative (blue) and TGD (orange), the second-order derivative (blue) and TGD (orange). For better visualization, we have scaled the TGD results.

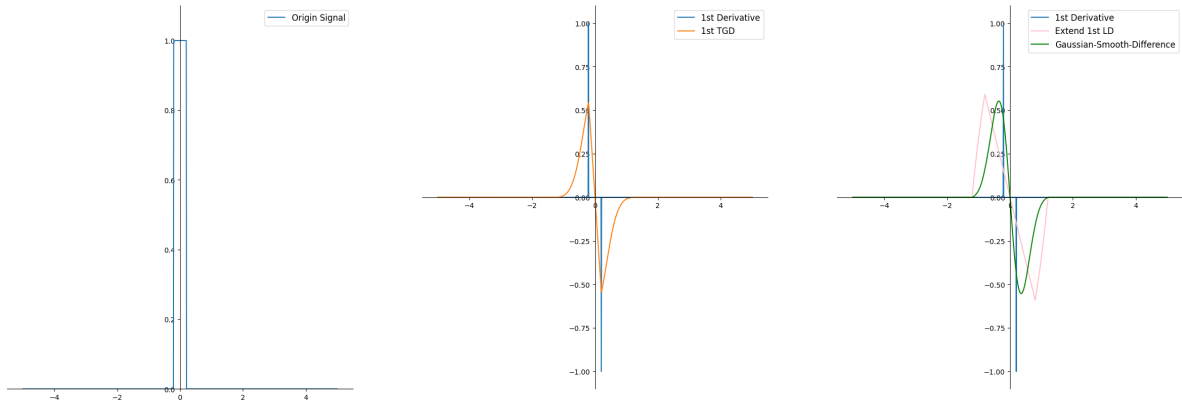


(a) Remove limit symbol of Lanczos Derivative

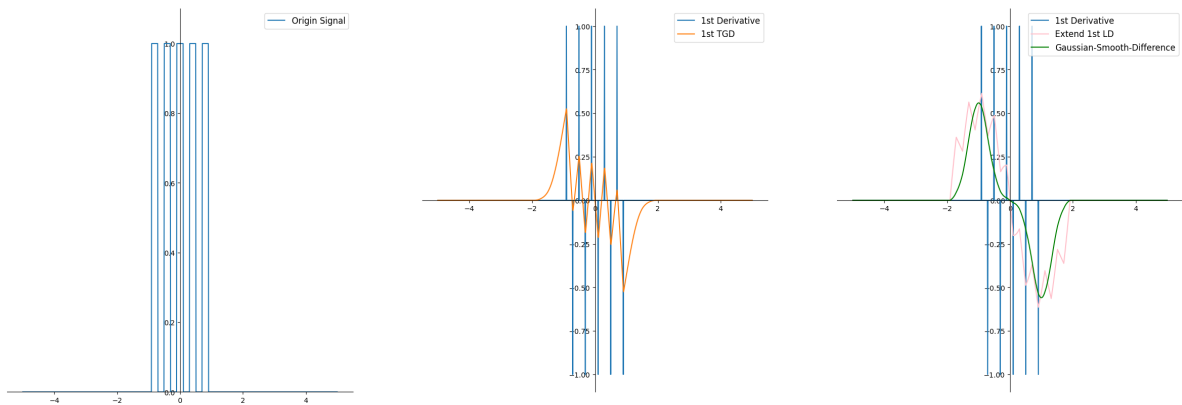


(b) Select Gaussian function as the smooth operator

Figure 10: Examples of operators that do not satisfy the constraint  $C2$  and/or  $C3$ .



(a) Square-wave signal



(b) Continue square-wave signal

Figure 11: Comparison of TGD, extend 1st LD, and Gaussian smoothing before difference results of square-wave signals. For better visualization, we have scaled the results.

## 2 Tao General Differential of Multivariate Function

### 2.1 Directional Derivative of Multivariate Function

In multivariate calculus, the directional derivative represents the instantaneous rate of change of a multivariate function with respect to a particular direction vector  $\mathbf{v}$  at a given differentiable point  $\mathbf{x}$ . The rate of change is interpreted as the velocity of the function moving through  $\mathbf{x}$  in the direction of  $\mathbf{v}$ . This concept generalizes the partial derivative, where the rate of change is calculated along one of the curvilinear coordinate curves [18].

The directional derivative of a  $n$ -variate function  $f(\mathbf{x}) = f(x_1, x_2, \dots, x_n)$  along with a vector  $\mathbf{v} = (v_1, v_2, \dots, v_n)$  is defined by the limit [19]:

$$\frac{\partial f}{\partial \mathbf{v}}(\mathbf{x}) = \lim_{h \rightarrow 0} \frac{f(\mathbf{x} + h\mathbf{v}) - f(\mathbf{x})}{h}. \quad (47)$$

In the follow-up description,  $\mathbf{v}$  is with respect to an arbitrary nonzero vector after normalization, i.e.,  $\|\mathbf{v}\| = 1$ . Thus we know the calculation of the partial derivative of a variable  $x_i$  is equivalent to finding the directional derivative of  $\mathbf{v} = (0, \dots, 0, 1, 0, \dots, 0)$ . And for a smooth function  $f$ , the Formula (47) is equivalent to the following equation:

$$\frac{\partial f}{\partial \mathbf{v}}(\mathbf{x}) = \lim_{h \rightarrow 0} \frac{f(\mathbf{x} + h\mathbf{v}) - f(\mathbf{x} - h\mathbf{v})}{2h}. \quad (48)$$

If a 1D TGD operator is used to perform the 1D TGD calculation at the point  $\mathbf{x}$  along the direction of the unit vector  $\mathbf{v}$  within an interval of length  $2W$  centered at  $\mathbf{x}$ , the mathematical expression can be written in the following form by replacing scalar with vector in Formula (12):

$$f'_{\text{TGD}}(\mathbf{x}; w, W, \mathbf{v}) \triangleq \frac{\int_0^W f(\mathbf{x} + t\mathbf{v}) w(t) dt - \int_0^W f(\mathbf{x} - t\mathbf{v}) w(t) dt}{2 \int_0^W tw(t) dt}, \quad (49)$$

The traditional directional derivative calculation (Formula (47)) yields stable derivative values since  $h$  tends to 0. The 1D TGD expands the calculation interval in one dimension, however, the function values and included noise are inherently coupled in all dimensions. As a result, TGD results become sensitive not only to function values but also to noise around the direction  $\mathbf{v}$ . For instance, both function value and noise could change significantly when  $\mathbf{v}$  deflects by a tiny angle. This scenario is akin to a circle with a small central angle, but the larger the radius of the circle, the farther the two points on the corresponding circumference are from each other. Large variations in the calculated values can cause instability in calculating TGD. Consequently, the expanded derivative interval (Formula (49)) in the direction  $\mathbf{v}$  is insufficient in representing the directional TGD of multivariate functions.

### 2.2 Directional TGD and Rotational Construction Method

To ensure computational stability, the calculation interval of TGD needs to be further extended in all dimensions. In more detail, we weighted average the values of the 1D TGD of all directions whose acute angle is to  $\mathbf{v}$ . Initially, we define  $\mathbb{S}_{\mathbf{v}}$  as the set of all unit vectors whose angle with  $\mathbf{v}$  is acute:

$$\mathbb{S}_{\mathbf{v}} \triangleq \{\mathbf{y} \mid \|\mathbf{y}\| = 1, 0 < \mathbf{v} \cdot \mathbf{y} \leq 1\}, \quad (50)$$

where  $\|\cdot\|$  denotes the modulus length. As  $\|\mathbf{v}\| = \|\mathbf{y}\| = 1$ ,  $\mathbf{v} \cdot \mathbf{y} = \frac{\mathbf{v} \cdot \mathbf{y}}{\|\mathbf{v}\| \cdot \|\mathbf{y}\|}$  indicates the cosine similarity of  $\mathbf{v}$  and  $\mathbf{y}$ .

Based on this, we define the **First-order Directional TGD of Multivariate Function** as the weighted average of the first-order TGD in directions where the angle with the target direction is acute:

$$\begin{aligned} \frac{\partial_{\text{TGD}} f}{\partial \mathbf{v}}(\mathbf{x}) &\triangleq \frac{\int_{\mathbb{S}_{\mathbf{v}}} f'_{\text{TGD}}(\mathbf{x}; w, W, \mathbf{y})(\mathbf{x}) \tilde{w}(\arccos(\mathbf{v} \cdot \mathbf{y})) dS}{\int_{\mathbb{S}_{\mathbf{v}}} \tilde{w}(\arccos(\mathbf{v} \cdot \mathbf{y})) dS} \\ &= K_1 (\tilde{T}_{\mathbf{v}} * f)(\mathbf{x}), \end{aligned} \quad (51)$$

where  $dS$  denotes the differential element, i.e., the arc length element in the 2D case and the area element in the 3D case. And  $\arccos(\mathbf{v} \cdot \mathbf{y})$  represents the angle between  $\mathbf{v}$  and  $\mathbf{y}$ .  $K_1$  is the normalization factor:

$$K_1 = \frac{1}{2 \int_0^W tw(t) dt} \cdot \frac{1}{\int_{\mathbb{S}_{\mathbf{v}}} \tilde{w}(\arccos(\mathbf{v} \cdot \mathbf{y})) dS}. \quad (52)$$

$\tilde{w}(\theta)$  is the **rotation weight function** defined in  $(-\frac{\pi}{2}, \frac{\pi}{2})$ . And it is an non-negative even function monotonically non-increasing when  $\theta \geq 0$  and satisfies the normalization condition  $\int_{-\frac{\pi}{2}}^{\frac{\pi}{2}} \tilde{w}(\theta) d\theta = 1$ . For example, we can take

cosine function  $\tilde{w}(\theta) = c \cos(\theta)$  where  $c$  is the normalization factor. At this point, the above computational model (Formula (51)) retains the Differential-by-Convolution mode, that is, the convolution of the multivariate function  $f$  with the multivariate **first-order directional TGD operator**  $\tilde{T}_{\mathbf{v}}$ .

$$\tilde{T}_{\mathbf{v}}(\mathbf{t}) = \begin{cases} T(\|\mathbf{t}\|) \tilde{w}(\arccos(\cos(\mathbf{v}, \mathbf{t}))) & 0 < \cos(\mathbf{v}, \mathbf{t}) \leq 1, \|\mathbf{t}\| \leq W \\ T(-\|\mathbf{t}\|) \tilde{w}(\arccos(\cos(\mathbf{v}, \mathbf{t})) - \pi) & -1 \leq \cos(\mathbf{v}, \mathbf{t}) < 0, \|\mathbf{t}\| \leq W \\ 0 & \cos(\mathbf{v}, \mathbf{t}) = 0, \|\mathbf{t}\| \leq W \text{ or } \|\mathbf{t}\| > W \end{cases} \quad (53)$$

where  $T$  is the 1D first-order TGD operator (see Section 1.3 for specific examples),  $\|\cdot\|$  denotes the modulus length,  $\cos(\mathbf{v}, \mathbf{t}) = \frac{\mathbf{v} \cdot \mathbf{t}}{\|\mathbf{v}\| \|\mathbf{t}\|}$  indicates the cosine similarity of  $\mathbf{v}$  and  $\mathbf{t}$ , and  $\arccos(\cos(\mathbf{v}, \mathbf{t}))$  denotes the angle between  $\mathbf{v}$  and  $\mathbf{t}$ .

Similarly, we define the **Second-order Directional TGD of Multivariate Function** as the weighted average of the second-order TGD in directions where the angle with the target direction is acute.

$$f''_{\text{TGD}}(\mathbf{x}; w, W, \mathbf{v}) \triangleq \frac{\int_0^W f(\mathbf{x} + t\mathbf{v})w(t)dt + \int_0^W f(\mathbf{x} - t\mathbf{v})w(t)dt - 2f(\mathbf{x})\int_0^W w(t)dt}{\int_0^W t^2w(t)dt} \quad (54)$$

$$\begin{aligned} \frac{\partial^2_{\text{TGD}} f}{\partial \mathbf{v}^2}(\mathbf{x}) &\triangleq \frac{\int_{\mathbb{S}_{\mathbf{v}}} f''_{\text{TGD}}(\mathbf{x}; w, W, \mathbf{y}) \tilde{w}(\arccos(\mathbf{v} \cdot \mathbf{y})) dS}{\int_{\mathbb{S}_{\mathbf{v}}} \tilde{w}(\arccos(\mathbf{v} \cdot \mathbf{y})) dS} \\ &= K_2(\tilde{R}_{\mathbf{v}} * f)(\mathbf{x}), \end{aligned} \quad (55)$$

where  $dS$  denotes the differential element. And  $\arccos(\mathbf{v} \cdot \mathbf{y})$  represents the angle between  $\mathbf{v}$  and  $\mathbf{y}$ .  $K_2$  is the normalization factor:

$$K_2 = \frac{1}{\int_0^W t^2w(t)dt} \cdot \frac{1}{\int_{\mathbb{S}_{\mathbf{v}}} \tilde{w}(\arccos(\mathbf{v} \cdot \mathbf{y})) dS} \quad (56)$$

All the definitions of mathematical symbols are consistent with the first-order case. And, the above computational model (Formula (55)) is equivalent to the convolution of the multivariate function  $f$  with the multivariate **second-order directional TGD operator**  $\tilde{R}_{\mathbf{v}}$ .

$$\tilde{R}_{\mathbf{v}}(\mathbf{t}) = \begin{cases} R(\|\mathbf{t}\|) \tilde{w}(\arccos(\cos(\mathbf{v}, \mathbf{t}))) & 0 < \cos(\mathbf{v}, \mathbf{t}) \leq 1, \|\mathbf{t}\| \leq W \\ R(-\|\mathbf{t}\|) \tilde{w}(\arccos(\cos(\mathbf{v}, \mathbf{t})) - \pi) & -1 \leq \cos(\mathbf{v}, \mathbf{t}) < 0, \|\mathbf{t}\| \leq W \\ 0 & \cos(\mathbf{v}, \mathbf{t}) = 0, \|\mathbf{t}\| \leq W \text{ or } \|\mathbf{t}\| > W \end{cases} \quad (57)$$

where  $R$  is the 1D second-order TGD operator (see Section 1.3 for specific examples),  $\|\cdot\|$  denotes the modulus length,  $\cos(\mathbf{v}, \mathbf{t}) = \frac{\mathbf{v} \cdot \mathbf{t}}{\|\mathbf{v}\| \|\mathbf{t}\|}$  indicates the cosine similarity of  $\mathbf{v}$  and  $\mathbf{t}$ , and  $\arccos(\cos(\mathbf{v}, \mathbf{t}))$  represents the angle between  $\mathbf{v}$  and  $\mathbf{t}$ .

Since the construction of  $\tilde{T}_{\mathbf{v}}$  and  $\tilde{R}_{\mathbf{v}}$  involves combining one-dimensional TGD operators with rotation weights  $\tilde{w}$ , this construction method is called the **Rotational Construction Method**. Moreover, both  $\tilde{T}_{\mathbf{v}}$  and  $\tilde{R}_{\mathbf{v}}$  demonstrate symmetry, and their integrals amount to 0. Consequently, the TGD value remains constant at 0 for constant functions:

$$\int \tilde{T}_{\mathbf{v}}(\mathbf{t})d\mathbf{t} = \int \tilde{R}_{\mathbf{v}}(\mathbf{t})d\mathbf{t} = 0 \quad (58)$$

Despite the complexity of the mathematical formula, the directional TGDs defined by Formula (51) and (55) are still *Differential-by-Convolution*, and the actual calculation process is quite simple and efficient. Due to the unbiasedness of TGD, the normalization constants ( $K_1$  and  $K_2$ ) are usually negligible in practical applications, allowing us to calculate the directional TGD through a convolution after obtaining the operators ( $\tilde{T}_{\mathbf{v}}$  and  $\tilde{R}_{\mathbf{v}}$ ). In subsequent sections, we shall give examples of 2D and 3D directional TGD operators.

### 2.3 Rotational Constructed 2D Directional TGD Operators

We instantiate 2D directional TGD operators by employing various weight functions in the rotational constructed method. Without loss of generality, we consider the directional TGD at the  $x$ -direction, where the angle variable  $\theta$  is measured from the positive direction of the  $x$ -axis. The rotation weight  $\tilde{w}(\theta)$  is aimed at decreasing the weight as the rotation angle increases, which can be achieved by a variety of functions, such as the constant, linear, cosine, and exponential functions. Each function has a different rate of decrease as  $\theta$  increases, with the fastest decreasing being the exponential function, and the slowest and simplest being the constant function. In general, the constructed

TGD operators exhibit anisotropy and decrease as  $\theta$  increases. This property allows for proper characterization of the function in a particular direction.

$$\tilde{w}_{\text{constant}}(\theta) = 1/\pi \quad \theta \in (-\pi/2, \pi/2), \quad (59)$$

$$\tilde{w}_{\text{linear}}(\theta) = c(-|\theta| + \pi) \quad \theta \in (-\pi/2, \pi/2), \quad (60)$$

$$\tilde{w}_{\text{cos}}(\theta) = c \cos \theta \quad \theta \in (-\pi/2, \pi/2), \quad (61)$$

$$\tilde{w}_{\text{exp}}(\theta) = ce^{-|\theta|} \quad \theta \in (-\pi/2, \pi/2), \quad (62)$$

where  $c$  is the normalization factor such that constraint  $\int_{-\pi/2}^{\pi/2} \tilde{w}(\theta) d\theta = 1$  is satisfied. Recall that when using the Gaussian kernel function (Section 1.3.3), we have:

$$T_{\text{gaussian}}(x) = \begin{cases} ke^{-x^2/2\delta^2} & x \in [-W, 0) \\ 0 & x = 0 \\ -ke^{-x^2/2\delta^2} & x \in (0, W] \end{cases}$$

$$R_{\text{gaussian}}(x) = \begin{cases} ke^{-x^2/2\delta^2} & x \in [-W, 0) \cup (0, W] \\ -2\delta(0) & x = 0 \end{cases}$$

Combining the rotation weights  $\tilde{w}(\theta)$  and the 1D TGD operators  $T_{\text{gaussian}}(x)$  and  $R_{\text{gaussian}}(x)$ , the 2D TGD operators  $\tilde{T}_x(x, y)$  and  $\tilde{R}_x(x, y)$  can be constructed as follows:

$$\tilde{T}_x(x, y) = \begin{cases} T_{\text{gaussian}}(\sqrt{x^2 + y^2}) \tilde{w}\left(\arccos\left(\frac{x}{\sqrt{x^2 + y^2}}\right)\right) & x > 0, \sqrt{x^2 + y^2} \leq W \\ 0 & x = 0, \sqrt{x^2 + y^2} \leq W \\ T_{\text{gaussian}}(-\sqrt{x^2 + y^2}) \tilde{w}\left(\arccos\left(\frac{-x}{\sqrt{x^2 + y^2}}\right)\right) & x < 0, \sqrt{x^2 + y^2} \leq W \end{cases} \quad (63)$$

$$\tilde{R}_x(x, y) = \begin{cases} R_{\text{gaussian}}(\sqrt{x^2 + y^2}) \tilde{w}\left(\arccos\left(\frac{x}{\sqrt{x^2 + y^2}}\right)\right) & x > 0, \sqrt{x^2 + y^2} \leq W \\ -2\delta(0) & x = y = 0 \\ 0 & x = 0, y \in [-W, 0) \cup (0, W] \\ R_{\text{gaussian}}(-\sqrt{x^2 + y^2}) \tilde{w}\left(\arccos\left(\frac{-x}{\sqrt{x^2 + y^2}}\right)\right) & x < 0, \sqrt{x^2 + y^2} \leq W \end{cases} \quad (64)$$

Based on the TGD operators  $\tilde{T}_x$  and  $\tilde{R}_x$ , the 2D directional TGD operators  $\tilde{T}_\theta$  and  $\tilde{R}_\theta$  with the angle  $\theta$  between the difference direction and the  $x$ -axis, can be obtained by the coordinate rotation operation.

$$\begin{bmatrix} x' \\ y' \end{bmatrix} = \begin{bmatrix} \cos \theta & \sin \theta \\ -\sin \theta & \cos \theta \end{bmatrix} \begin{bmatrix} x \\ y \end{bmatrix}$$

$$\begin{aligned} \tilde{T}_\theta(x, y) &= \tilde{T}_x(x', y') \\ \tilde{R}_\theta(x, y) &= \tilde{R}_x(x', y') \end{aligned} \quad (65)$$

Figure 12 displays the 2D first-order TGD operators  $\tilde{T}_\theta$  based on the Gaussian kernel function and their projection diagram, and Figure 13 shows the 2D second-order TGD operators  $\tilde{R}_\theta$  based on the Gaussian kernel function and their projection diagram, where  $\tilde{w}(\theta)$  chooses constant, linear, cosine, and exponential functions, respectively. The figures feature examples of the 0° and 45° derivation directions. The projection diagram demonstrates that the operator energy is primarily concentrated in the differential direction.

In Figure 14, the positive part of the second-order TGD operator is enlarged for presentation convenience. Of particular interest is the demonstration that this operator performs TGD calculations in the differential direction, while approximately Gaussian integrals filtering (Figure 1) in the orthogonal direction, thereby suppressing noise during TGD calculation. This indicates that the 2D TGD is filtered in its orthogonal direction to suppress the noise while calculating the TGD. The two together make the TGD calculation stable to function values as well as noise, highlighting the practicality of this method in real-world applications. This property can be extended to the first- and second-order directional TGD of general multivariate functions.

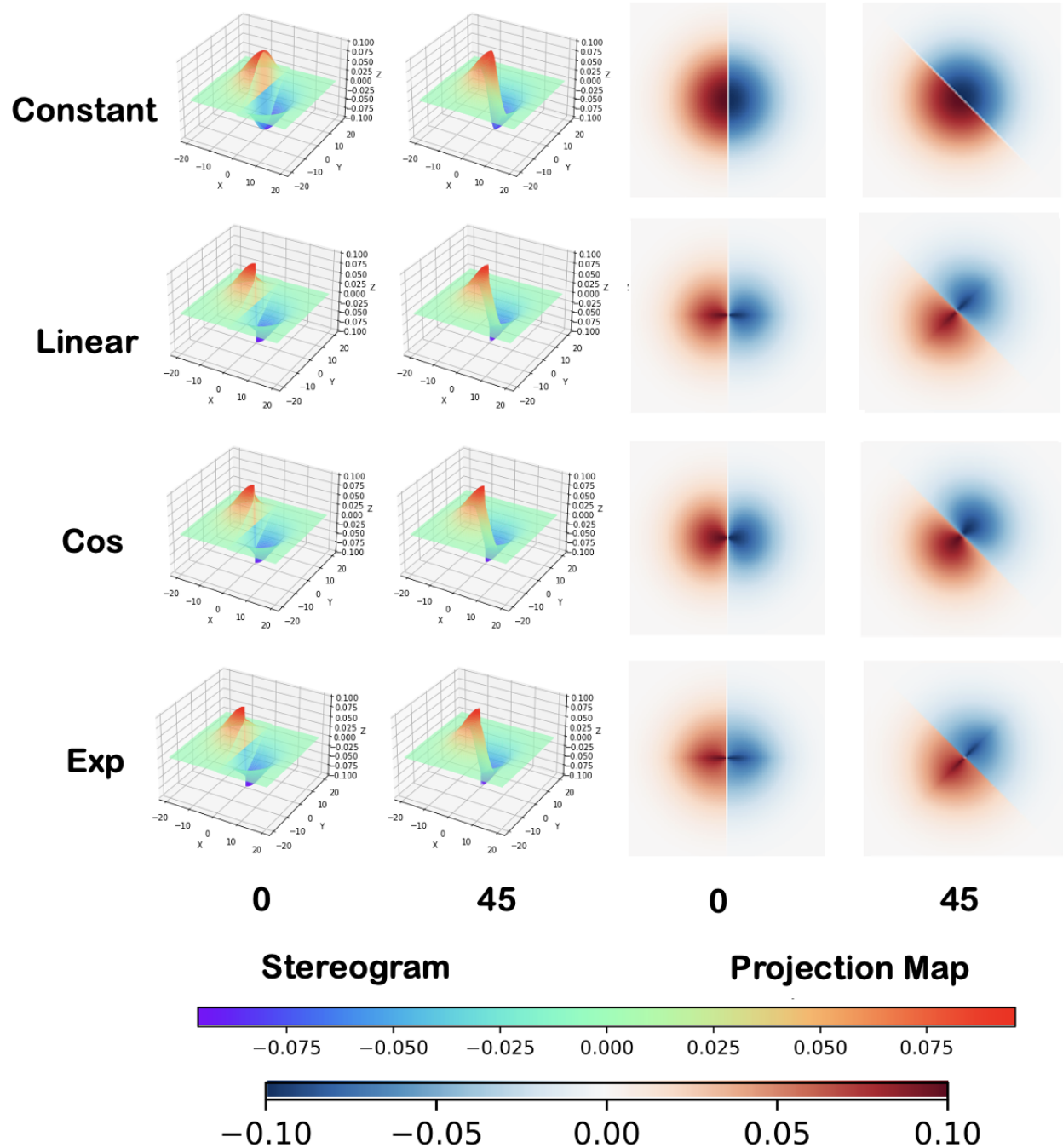


Figure 12: The 2D first-order directional TGD operator  $\tilde{T}_v$  and its projection map. Gaussian kernel function is used, and the derivation directions include  $0^\circ$  and  $45^\circ$ ,  $\tilde{w}(\theta)$  for constant, linear, cosine, and exponential functions, respectively.

In mathematics, the Laplace operator is a differential operator defined as the divergence of the gradient of a function in Euclidean space. The Laplacian is invariant under all Euclidean transformations: rotations and translations. The Laplacian appears in differential equations that describe various physical phenomena, hence its extensive application in scientific modeling. Additionally, in computer vision, the Laplace operator has proven useful for multiple tasks, including blob and edge detection [20, 21, 22].

When we take a constant function in the rotation weight (Formula (59)), and add the definitions  $\tilde{w}_{\text{constant}}(\pi/2) = \tilde{w}_{\text{constant}}(-\pi/2) = 1/\pi$ , then the 2D second-order TGD operator becomes an isotropic operator with rotational

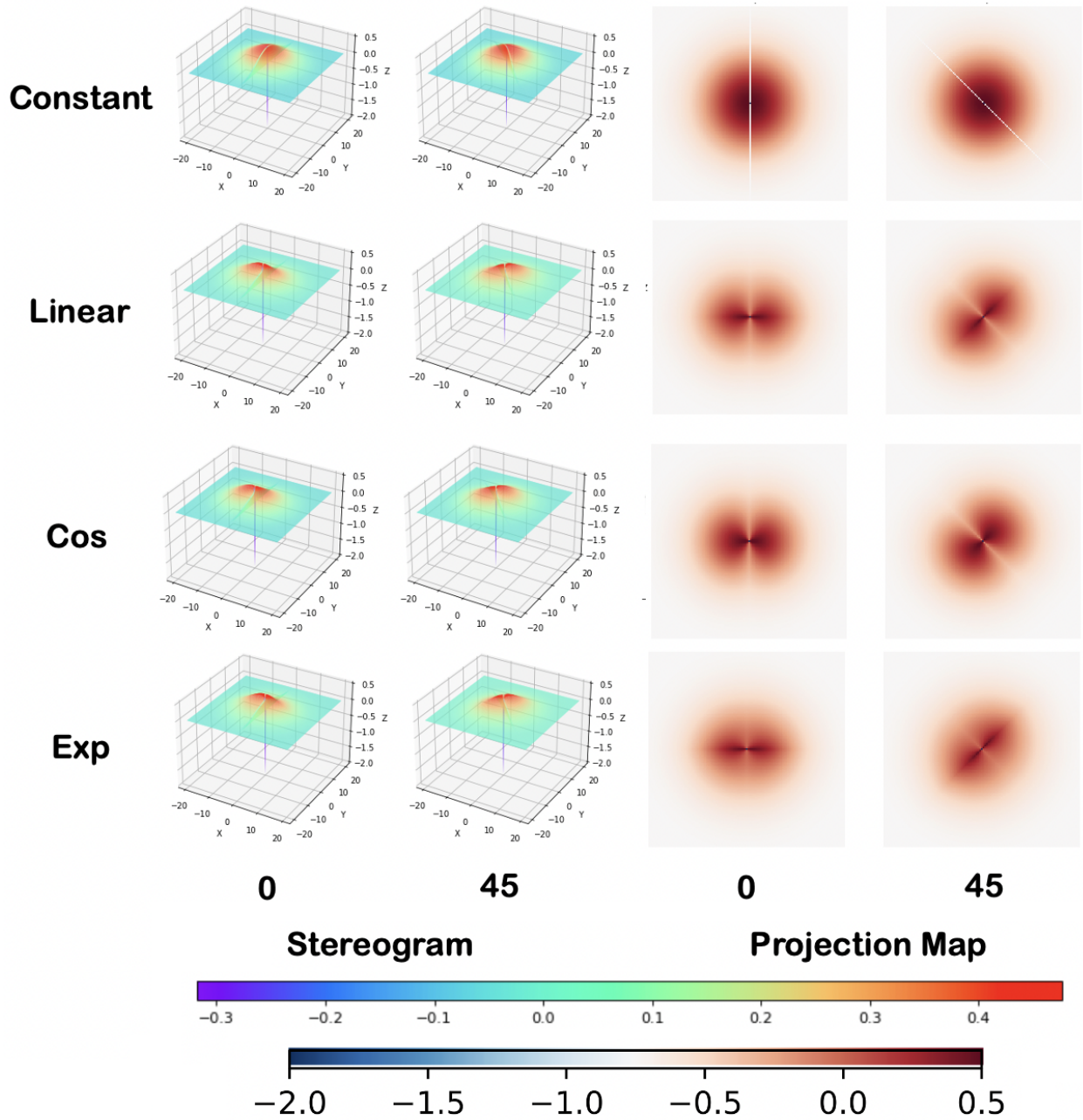


Figure 13: The 2D second-order directional TGD operator  $\tilde{R}_v$  and its projection map. Gaussian kernel function is used, and the derivation directions include  $0^\circ$  and  $45^\circ$ ,  $\tilde{w}(\theta)$  for constant, linear, cosine, and exponential functions, respectively.

invariance. We notice that these operators conform to the definition of the Laplace operator and take various forms depending on the employed kernel functions. We collectively refer to them as **Laplace of TGD (LoT) operators**.

$$\text{LoT}(x, y) = \begin{cases} R(\sqrt{x^2 + y^2}) \tilde{w}_{\text{constant}}\left(\arccos\left(\frac{|x|}{\sqrt{x^2 + y^2}}\right)\right) & 0 < \sqrt{x^2 + y^2} \leq W \\ -2\delta(0) & x = y = 0 \end{cases} \quad (66)$$

It is worth noting that the LoT operator still satisfies the integral of 0, which indicates that for a constant function, its Laplace TGD is constant and equal to 0.

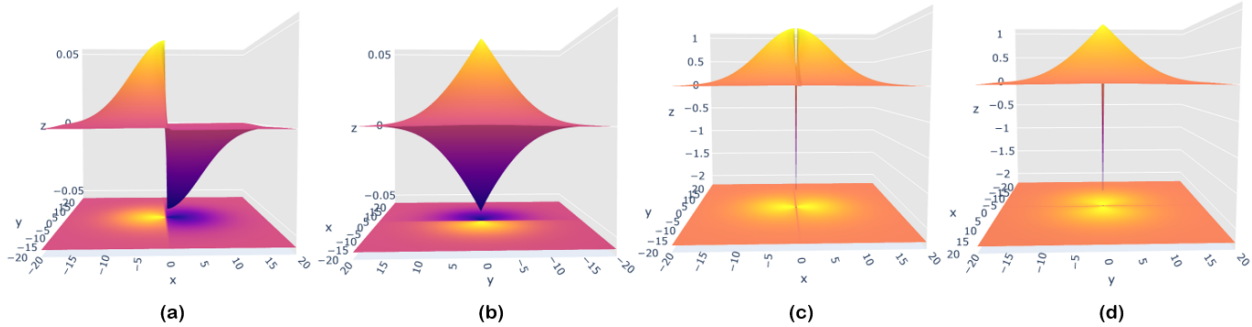


Figure 14: The cross-sections of 2D first- and second-order directional TGD operators: (a) for the first-order operator derivative-direction cross-section, (b) for the first-order operator orthogonal-direction cross-section, (c) for the second-order operator derivative-direction cross-section, and (d) for the second-order operator orthogonal-direction cross-section.

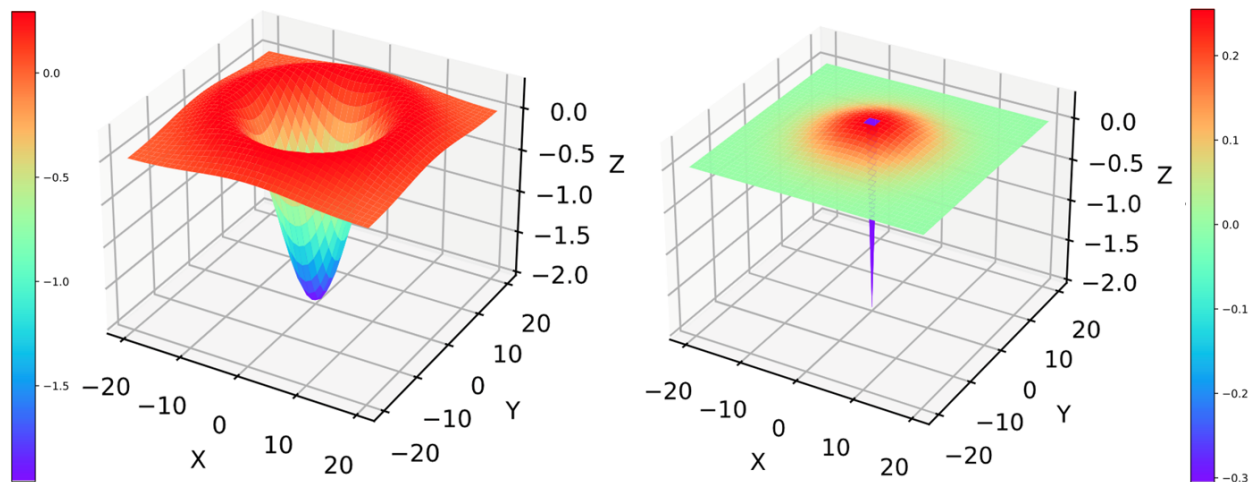


Figure 15: LoG (Laplace of Gaussian) operator (Left) and LoT (Laplace of TGD) operator (Right) constructed with Gaussian kernel function.

Figure 15 shows the 2D LoG as well as the LoT operator constructed using a Gaussian kernel function. Both operators are normalized to have a minimum value of  $-2$ . Although they share a commonality in being created using Gaussian functions, they differ in the distribution of negative values. With the LoG operator, the negative values are concentrated around the center, and the maximum positive values are far from the center. In contrast, with the LoT operator, negative values are only in the center, and the maximum positive values are next to the center. This difference embodies the Monotonic Constraint, which, in the theory of TGD, ensures that the zero-crossing positions of difference values (where the original signal changes fastest locally) obtained using the LoT operator are unbiased.

The rotational construction method can also be utilized to construct multivariate directional TGD operators. The constructed operator is expressed in dense high-dimensional convolution kernel, which is the high dimensional directional *Differential-by-Convolution*.

## 2.4 Partial TGD and Orthogonal Construction Method

For calculating the TGD of high dimensional functions efficiently, we introduce a simple and intuitive way of constructing operators, called the **Orthogonal Construction Method**. Figure 12-14 demonstrate that the 2D TGD operator performs general differential calculation in the differential direction and low-pass filtering based on a convex function in the orthogonal direction. This suggests that the 2D TGD computes the 1D TGD in its differential direction while filtering in its orthogonal direction to suppress noise. Therefore, we define the **2D orthogonal TGD operators**

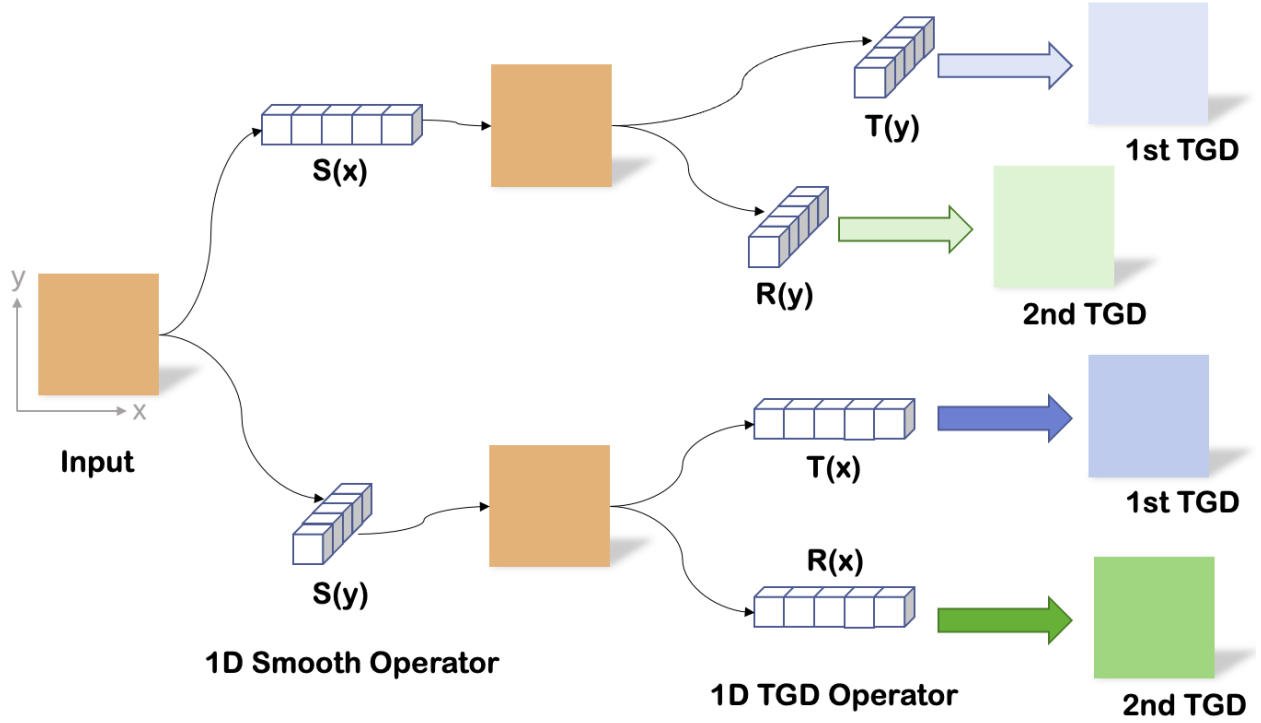


Figure 16: The decomposition diagram of the convolution calculation process of an image and 2D TGD operators obtained by the orthogonal construction method.

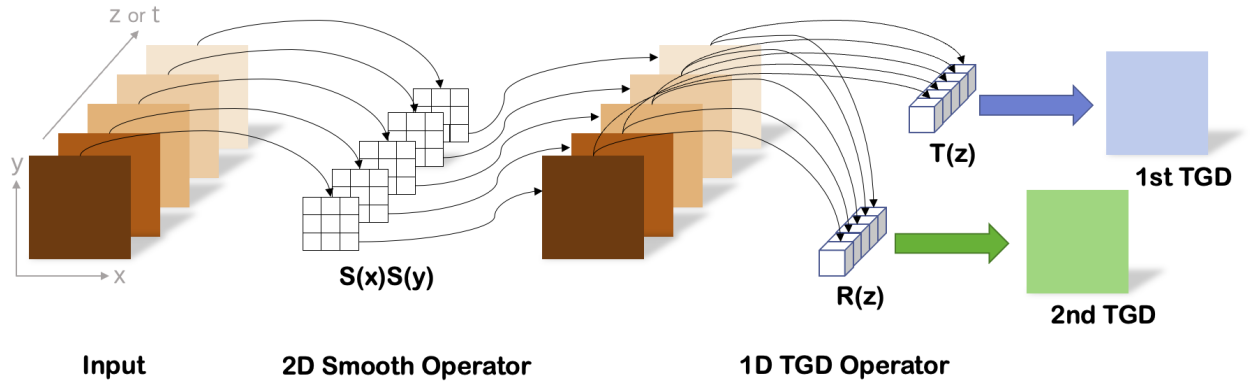


Figure 17: The decomposition diagram of the convolution calculation process of a series of images and 3D TGD operators obtained by the orthogonal construction method.

as follows (Figure 16):

$$\begin{aligned}\tilde{T}_{x\perp}(x, y) &\triangleq T(x) \cdot S(y) \\ \tilde{R}_{x\perp}(x, y) &\triangleq R(x) \cdot S(y)\end{aligned}\quad (67)$$

where  $T(x)$  is the 1D first-order TGD operator,  $R(x)$  is the 1D second-order TGD operator, and  $S(x)$  is the 1D smooth operator (see Section 1.3).

Similarly, the multivariate **orthogonal TGD operators** are defined as follows (Figure 17):

$$\begin{aligned}\tilde{T}_{x_i\perp}(x_1, \dots, x_{i-1}, x_i, x_{i+1}, \dots, x_n) &\triangleq S(x_1) \dots S(x_{i-1})T(x_i)S(x_{i+1}) \dots S(x_n) \\ \tilde{R}_{x_i\perp}(x_1, \dots, x_{i-1}, x_i, x_{i+1}, \dots, x_n) &\triangleq S(x_1) \dots S(x_{i-1})R(x_i)S(x_{i+1}) \dots S(x_n)\end{aligned}\quad (68)$$

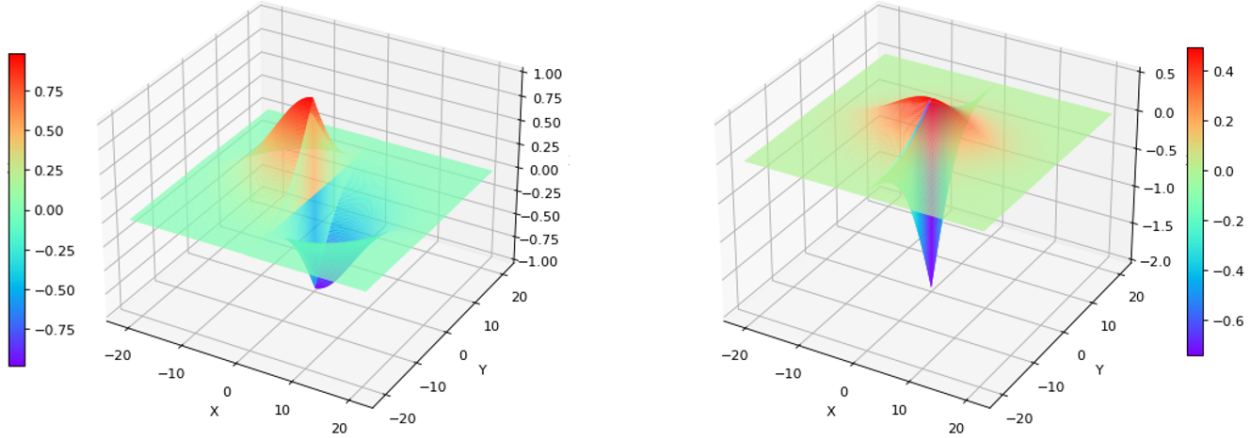


Figure 18: 2D first- and second-order TGD operators based on the orthogonal construction method. Gaussian kernel function is used for both TGD and filtering.

Based on Formula (20), it is easy to deduce that the orthogonal TGD operator satisfies an integral of 0:

$$\begin{aligned} \int \dots \int \tilde{T}_{x_i \perp}(x_1, \dots, x_{i-1}, x_i, x_{i+1}, \dots, x_n) dx_1 \dots dx_n &= 0 \\ \int \dots \int \tilde{R}_{x_i \perp}(x_1, \dots, x_{i-1}, x_i, x_{i+1}, \dots, x_n) dx_1 \dots dx_n &= 0 \end{aligned} \quad (69)$$

which means that the TGD value is constant to 0 for constant functions.

The multivariate TGD operators constructed via the orthogonal construction method perform TGD calculations along the coordinate axes, which is referred to as **partial TGD**, corresponding to the conventional partial derivative. It is, however, practical to construct TGD operators in any direction by employing coordinate rotation (Formula (65)).

Figure 18 illustrates the visualization results of the 2D first- and second-order TGD operators created using the orthogonal construction method. Compared to the TGD operators produced with the rotational construction method (Figure 12 and Figure 13), the first-order TGD operator remains practically unaltered, while the second-order TGD operator changes from having only one negative value at the origin to comprising a line, which is perpendicular to the differential direction and negative at the center. Furthermore, Figure 19 displays the cross-sections and contours of the 3D first- and second-order TGD operators in the  $z$ -direction, generated by the orthogonal construction method.

It is worth pointing out that the convex smooth operator can be approximated using a traditional Gaussian filter. Consider the operator obtained by the rotational construction method, and suppose the TGD kernel function uses Gaussian and the rotation weight  $\tilde{w}(\theta)$  is taken as a constant. In that case, the filter function in the orthogonal direction can be approximated using a Gaussian function. In practice, the smooth operator in the orthogonal construction method can be implemented using a variety of functions based upon specific needs.

The use of orthogonal operators brings about decoupling between dimensions, allowing each dimension to operate independently. This means that the 1D TGD is computed exclusively in the differential direction while filtering occurs in all orthogonal directions. The resulting decoupling enhances the speed of convolution computation while enhancing efficiency. Figure 16 and Figure 17 show decomposition diagrams detailing the convolution calculation process of the 2D and 3D TGD operators, respectively, constructed using the orthogonal construction method. In the 2D TGD computation, the 2D convolution can be split into two 1D convolutions. And in the 3D TGD calculation process, the dense 3D convolution can be divided into two parts: a 2D filtering and a 1D convolution.

## 2.5 2D TGD Calculation Examples

We provide intuitive visualizations of the computational outputs of 2D TGD based on smooth and non-smooth functions, aimed at facilitating an enhanced comprehension of high-dimensional TGD. In comparison with the partial derivatives, we utilize the orthogonal TGD operators (Figure 18). Furthermore, we present results obtained from the LoT operator. In all these experiments, TGD operators are constructed with the Gaussian kernel function.

Figure 20.a shows the 2D Gaussian signal and the computational results with respect to traditional partial derivative and partial TGD. For better visualization, we have scaled the results. Despite the difference in values of derivative and

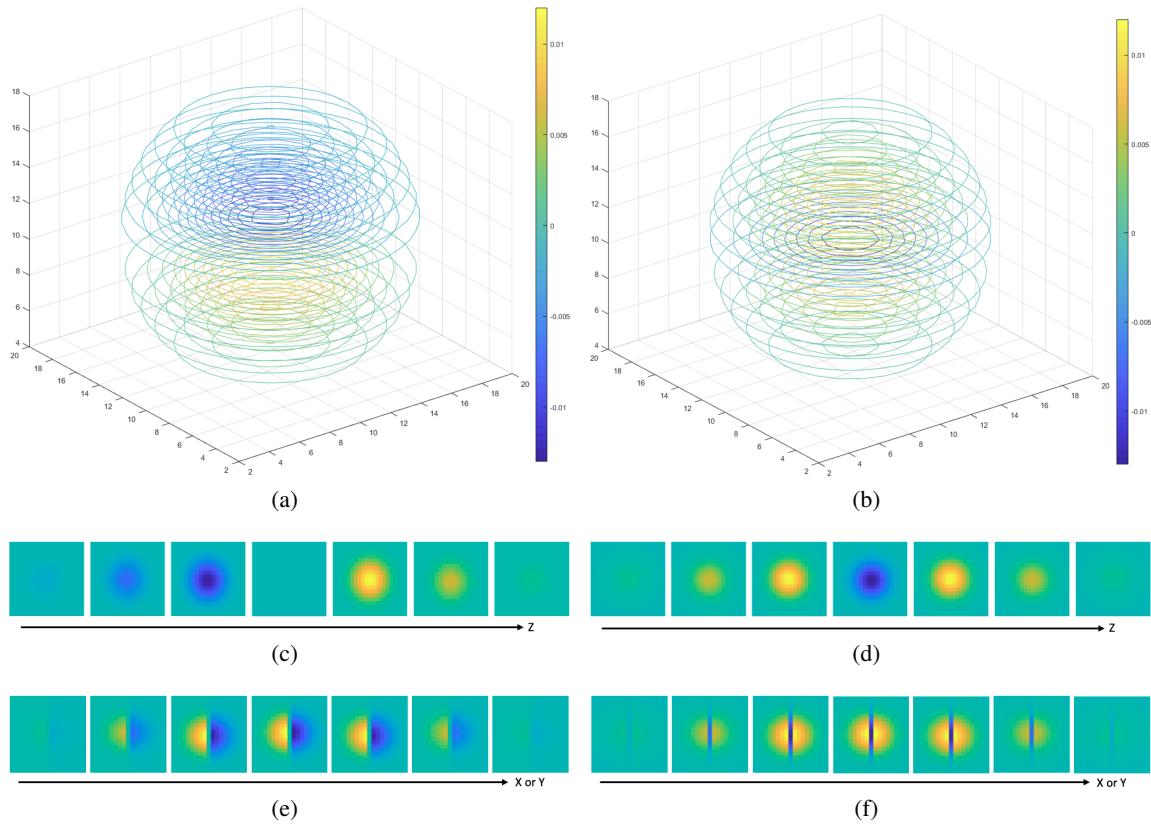
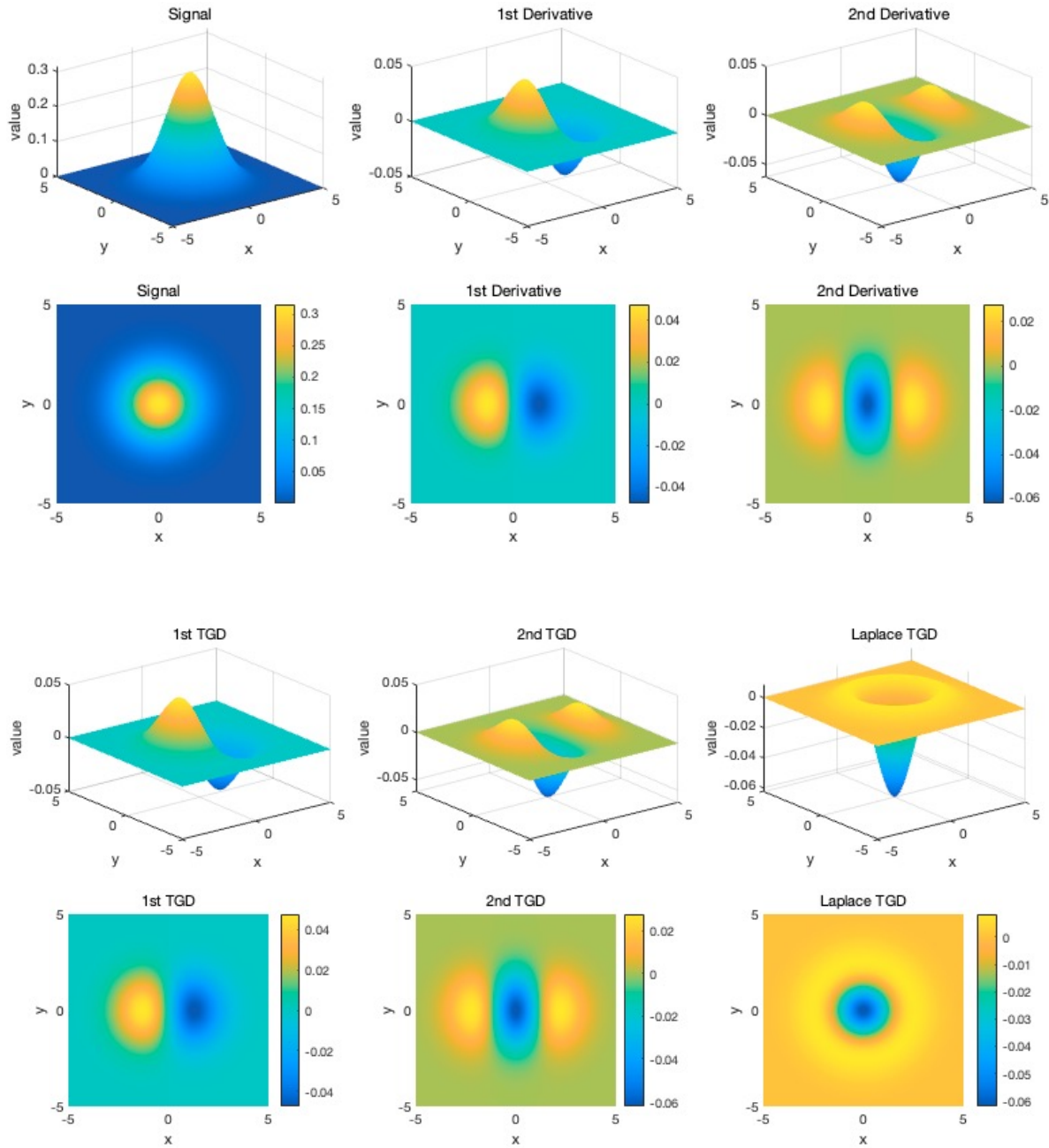


Figure 19: Schematic diagrams of 3D first- and second-order z-directional TGD operators obtained by the orthogonal construction method: (a) a contour plot of the vertical z-directional cross-section of the first-order operator; (b) a contour plot of the vertical z-directional cross-section of the second-order operator; (c) a vertical z-directional cross-section of the second-order operator; (d) a vertical z-directional cross-section of the first-order operator; (e) a vertical x-(or y)-directional cross-section of the first-order operator; (f) a second-order operator vertical x-(or y)-direction cross-sectional diagram. Gaussian kernel function is used for both TGD and filtering.

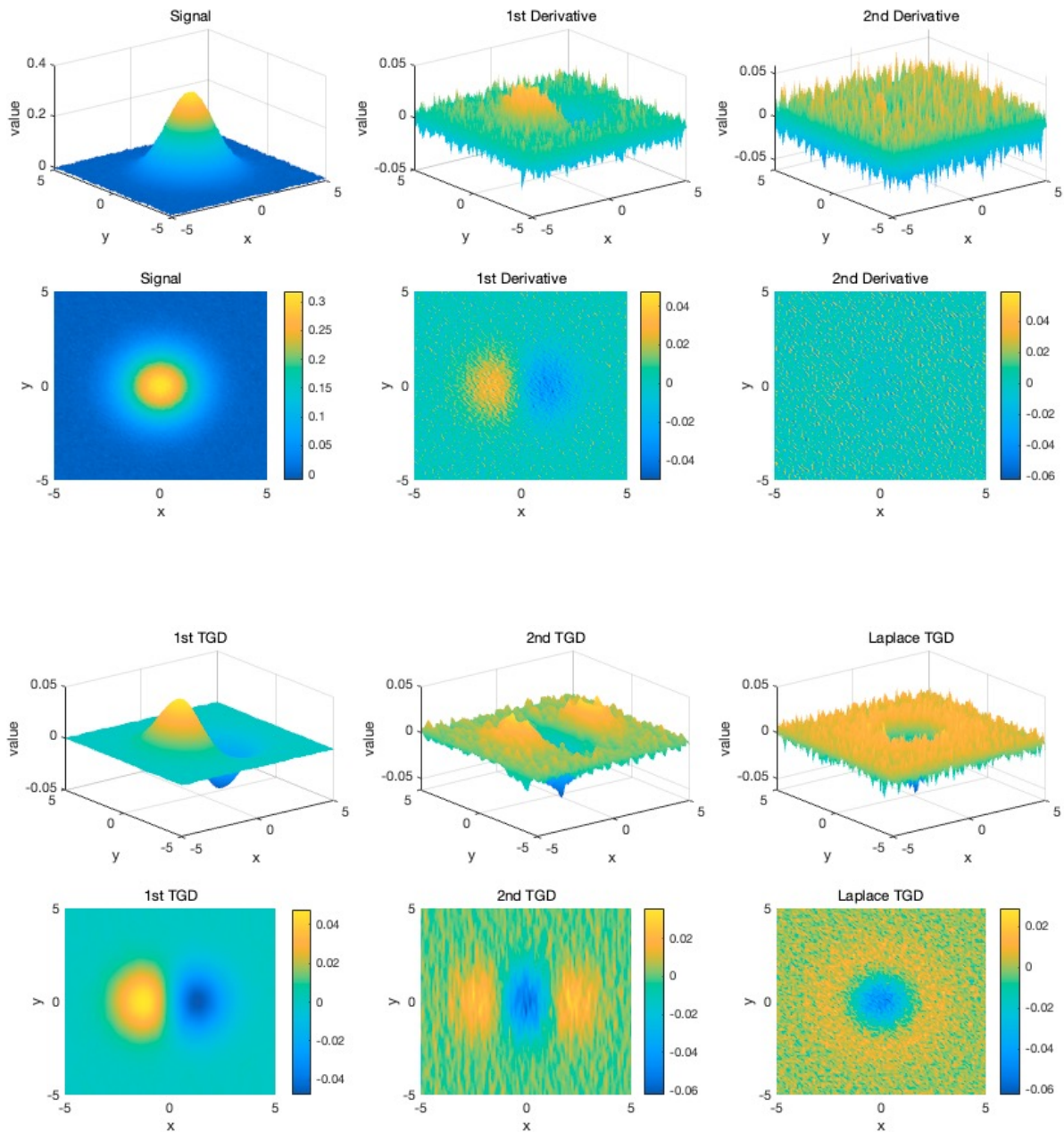
TGD, they are positively related, demonstrating *Unbiasedness*. By convolving the original Gaussian signal with the LoT operator, we obtain the Laplace TGD result for the 2D Gaussian, which is known as the “Laplacian of Gaussian” in computer vision. As shown in Figure 20.b, when we add a small amount of Gaussian noise, which is hardly visible in the original function, it has a drastic effect on the traditional derivative results. In contrast, the results calculated by TGD within a certain interval depict an exceptional ability to suppress noise.

We further extend the experiments from smooth functions to non-smooth functions. Figure 20.c displays the comparison of partial derivative and TGD results for a 2D square-wave signal. Since we calculate the partial derivatives in the  $x$ -direction, the derivative values are absent or infinite at the left and right edges of the square-wave and zero elsewhere. While in TGD results, there is a certain range of non-zero and meaningful values, which is caused by the fact that the operators have a certain size. Notably, the location of extreme points in the first-order TGD and the zero-crossing points in the second-order TGD remain precisely unchanged compared to the location of steps in the signal. Convolution of the square-wave signal with the LoT operator yields its Laplace TGD result, where zero-crossing points indicate exact positions of steps in the signal. These results demonstrate that TGD can precisely characterize the signal changes. Figure 20.d further highlights the noise resistance within non-smooth functions in TGD calculation.

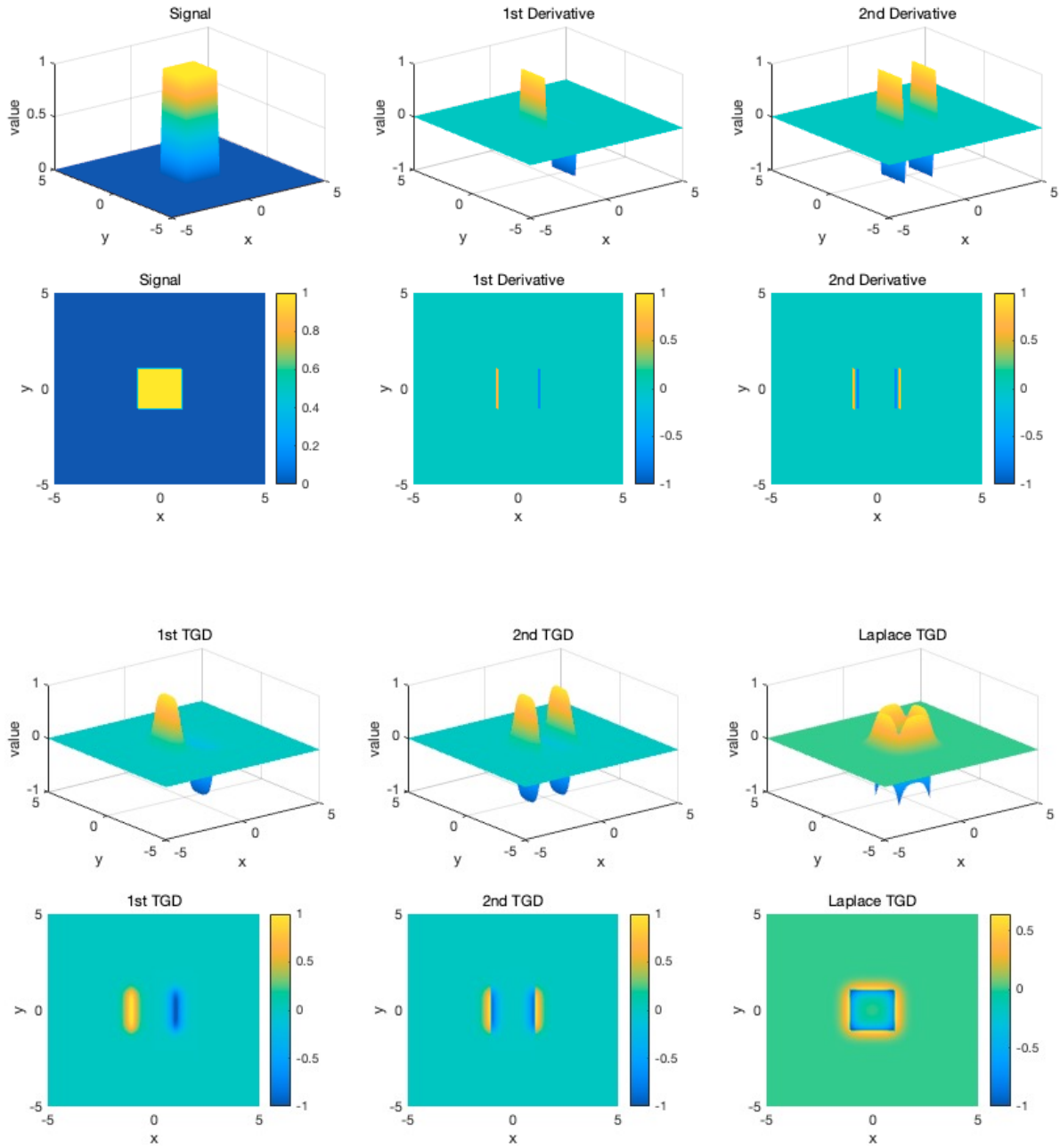
The experiments conducted illustrate the versatility of the *General Differential* in high-dimensional differential calculations of both smooth and non-smooth functions. The overall performance is stable and insensitive to noise. Additionally, TGD has proven to possess an excellent ability to characterize changes in real signals.



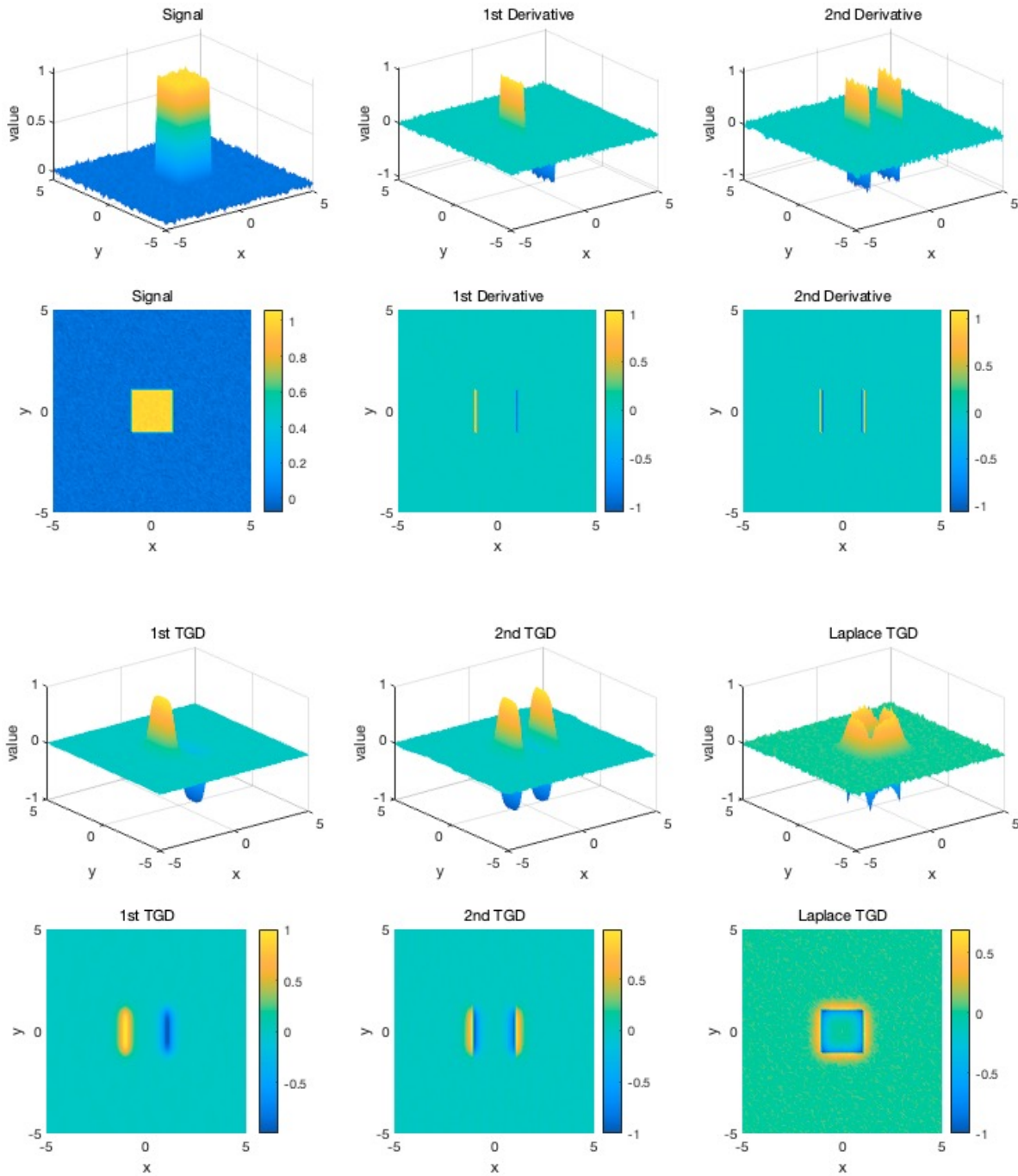
(a) 2D Gaussian signal



(b) 2D Gaussian signal with noise



(c) 2D square signal



(d) 2D square signal with noise

Figure 20: Comparison of partial derivative and partial TGD results of 2D smooth and non-smooth functions with/without noise. For better visualization, we have scaled the results and show both the 3D visualization (Up) and the projection map (Down) relatively.

### 3 Tao General Difference of Discrete Signal

#### 3.1 One-Dimensional Discrete TGD

In modern discrete systems, a discrete signal is denoted as  $X(n)$ , where  $n$  is an integer. The signal results from the sampling or discretization of a continuous signal  $f(x)$  over a certain time, space, or spatiotemporal interval. A one-dimensional discrete signal is written as:

$$X(n) = f(n\Delta), \tag{70}$$

where  $\Delta > 0$  is a discrete step known as the *sampling interval*. Without loss of generality, we set the sampling interval  $\Delta = 1$  in the following text to facilitate the expression.

Differential calculus necessitates continuous functions. However, in practice, obtaining the original continuous signal from a discrete signal is unachievable without additional information. Traditionally, the 1st- and 2nd-order central difference of the discrete signal is calculated among the neighboring points based on the definition of derivative (Formula (1)):

$$\begin{aligned} X'(n) &= \frac{X(n+1) - X(n-1)}{2} \\ X''(n) &= X(n+1) - 2X(n) + X(n-1) \end{aligned} \tag{71}$$

Notably, in discrete systems, sampling requires a certain interval for energy accumulation, and the values obtained reflect the “mean value” of the signal within the sampling interval. In short,  $\Delta x \rightarrow 0$  does not exist in discrete systems.

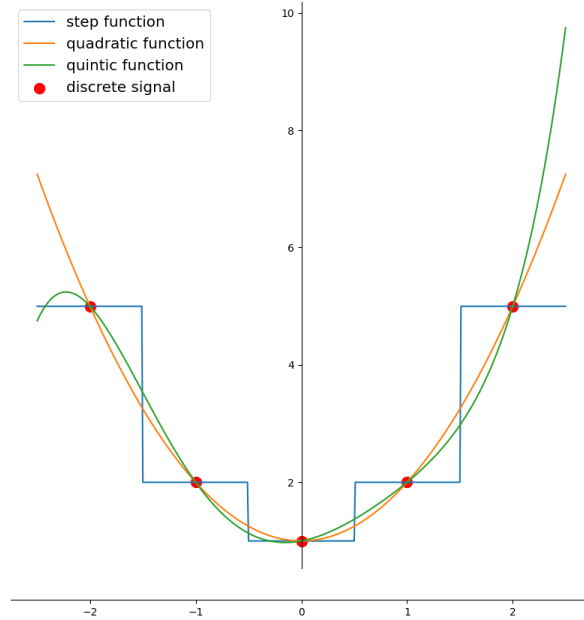


Figure 21: Different functions fitted to the discrete function for transforming it to continuous.

Consequently, when calculating the TGD of a discrete signal, we convert the discrete function into continuous by treating it as a continuous step function (blue curve in Figure 21), instead of fitting a smooth function based on a few discrete points (orange and green curves in Figure 21). This approach aligns more closely with the key properties of a discrete signal.

$$\hat{f}(x) \triangleq X(n) \quad x \in \left(n - \frac{1}{2}, n + \frac{1}{2}\right] \tag{72}$$

It should be noted that the step function is not suitable for fitting discrete functions in traditional differential calculations because it would result in a derivative value of 0 for each discrete point.

Here, we unify the concepts of both *Differential* and *Difference* in TGD by expressing the first-order Tao General Difference of a discrete signal as the first-order Tao General Differential (Formula (12)) of the corresponding step function (Formula (72)) at sampling locations:

$$\begin{aligned}
 X'_{\text{TGD}}(n; w, N) &\triangleq \hat{f}'_{\text{TGD}}\left(n; w, N + \frac{1}{2}\right) \\
 &= \frac{\int_0^{N+\frac{1}{2}} \hat{f}(n+t)w(t) dt - \int_0^{N+\frac{1}{2}} \hat{f}(n-t)w(t) dt}{2 \int_0^{N+\frac{1}{2}} tw(t) dt} \\
 &= C_1 \int_{-N-\frac{1}{2}}^{N+\frac{1}{2}} \hat{f}(n+t)T(-t) dt \\
 &= C_1 \sum_{i=-N}^N \int_{i-\frac{1}{2}}^{i+\frac{1}{2}} \hat{f}(n+t)T(-t) dt \\
 &= C_1 \sum_{i=-N}^N X(n+i) \int_{i-\frac{1}{2}}^{i+\frac{1}{2}} T(-t) dt \\
 &= C_1 \left(\hat{T} * X\right)(n)
 \end{aligned} \tag{73}$$

where  $C_1$  is the normalization constant, and  $\hat{T}$  is the interval integral of the 1st-order TGD operator  $T$ , which is a discrete sequence with  $2N + 1$  elements. Here, we call  $\hat{T}$  as the *First-order Discrete Tao General Difference Operator* (1st-order Discrete TGD Operator), and  $N$  as the *kernel size*.

$$C_1 = \frac{1}{2 \int_0^{N+\frac{1}{2}} tw(t) dt} \tag{74}$$

$$\hat{T}(i) = \int_{i-\frac{1}{2}}^{i+\frac{1}{2}} T(t) dt, \quad i = -N, -N+1, \dots, N-1, N \tag{75}$$

Similarly, we express the second-order Tao General Difference (TGD) of a discrete signal as the second-order Tao General Differential (Formula (13)) of the corresponding step function at sampling locations:

$$\begin{aligned}
 X''_{\text{TGD}}(n; w, N) &\triangleq \hat{f}''_{\text{TGD}}\left(n; w, N + \frac{1}{2}\right) \\
 &= C_2 \int_{-N-\frac{1}{2}}^{N+\frac{1}{2}} \hat{f}(n+t)R(-t) dt \\
 &= C_2 \sum_{i=-N}^N X(n+i) \int_{i-\frac{1}{2}}^{i+\frac{1}{2}} R(-t) dt \\
 &= C_2 \left(\hat{R} * X\right)(n)
 \end{aligned} \tag{76}$$

where  $C_2$  is the normalization constant, and  $\hat{R}$  is the interval integral of the 2nd-order TGD operator  $R$ , which is a discrete sequence with  $2N + 1$  elements. Here, we call  $\hat{R}$  as the *Second-order Discrete Tao General Difference Operator* (2nd-order Discrete TGD Operator).

$$C_2 = \frac{1}{\int_0^{N+\frac{1}{2}} t^2 w(t) dt} \tag{77}$$

$$\hat{R}(i) = \int_{i-\frac{1}{2}}^{i+\frac{1}{2}} R(t) dt, \quad i = -N, -N+1, \dots, N-1, N \tag{78}$$

Formula (73) and (76) manifest the Difference-by-Convolution in discrete TGD calculation. This method involves convolving the discrete signal  $X$  with the operator. The linearity of the convolution calculation confirms the linearity of

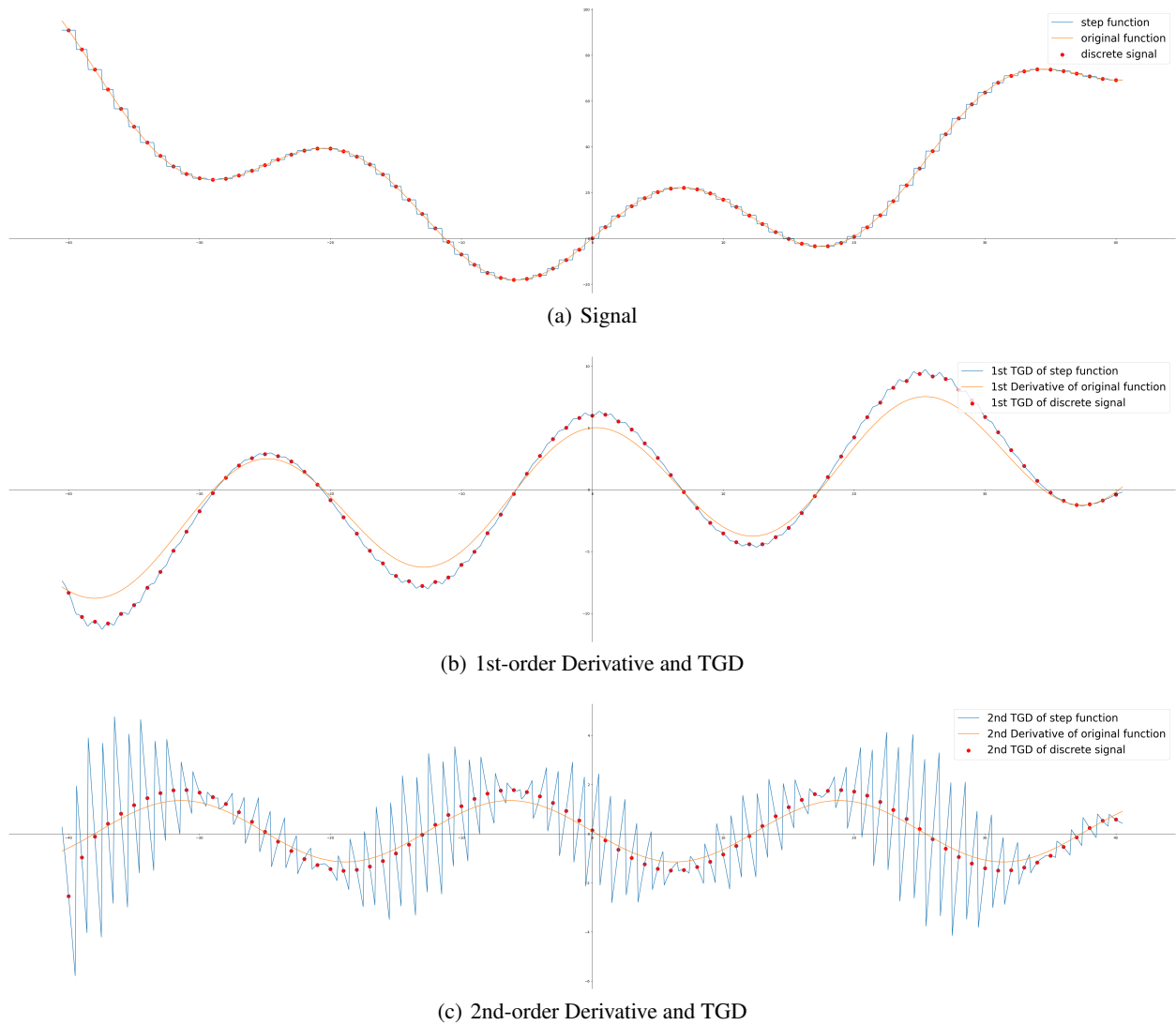


Figure 22: Schematic diagram of discrete TGD calculation. The discrete signal is sampled from the original signal equidistantly, containing 80 value points. We choose the Gaussian kernel function with a discrete operator having 11 elements.

discrete TGD, that is, the TGD of any linear combination of discrete signals is equal to the same linear combination of the TGD of the discrete signals:

$$\begin{aligned} (aX + bY)'_{\text{TGD}} &= aX'_{\text{TGD}} + bY'_{\text{TGD}} \\ (aX + bY)''_{\text{TGD}} &= aX''_{\text{TGD}} + bY''_{\text{TGD}} \end{aligned} \quad (79)$$

where  $a$  and  $b$  are real numbers.

We take an example to deepen the understanding of discrete TGD. Suppose we have a continuous signal  $f$  (orange curve in Figure 22.a), and we can easily get the derivative of  $f$  (orange curve in Figure 22.b and 22.c) via the differentiation formulas:

$$\begin{aligned} f(x) &= 20 \sin\left(\frac{x}{4}\right) + \frac{x^2}{20} \\ f'(x) &= 5 \cos\left(\frac{x}{4}\right) + \frac{x}{10} \\ f''(x) &= -\frac{5}{4} \sin\left(\frac{x}{4}\right) + \frac{1}{10} \end{aligned} \quad (80)$$

The discrete signal (red points in Figure 22.a) is obtained by sampling the function with a sampling interval  $\Delta = 1$ . Theoretically, it is impossible to reconstruct the original continuous signal from the sampled discrete signal. Here, we simply fit the continuous step function with the discrete points (blue curve in Figure 22.a) for TGD calculation (blue curve in Figure 22.b and 22.c).

The TGD of the discrete signal is defined as the Tao General Differential value of the corresponding step function at the sampling position. In practice, we can directly acquire the discrete TGD results by convolving the discrete signal and the discrete TGD operators ( $\hat{T}$  and  $\hat{R}$ ) directly. Notably, the discrete TGD values exhibit a positive correlation with the derivative values (Figure 22). Therefore, it is perfectly feasible to use TGD to characterize the variation of discrete signals without knowing the expression of the original function.

TGD unifies the concepts of both traditional *Differential* of continuous functions and *Difference* of discrete functions, and we do not distinguish between the two in the following. When discrete TGD is mentioned, it refers to Tao General Difference.

### 3.2 One-Dimensional Discrete TGD Operators

Recalling the expressions for TGD operator  $T$  (Formula (16)) and  $R$  (Formula (19)), we can further expressed Formula (75) and (78) in the following form:

$$\hat{T}(i) = \begin{cases} \int_{i-\frac{1}{2}}^{i+\frac{1}{2}} w(-t) dt > 0 & i = -N, -N+1, \dots, -1 \\ \int_{-\frac{1}{2}}^0 w(-t) dt + \int_0^{\frac{1}{2}} -w(t) dt = 0 & i = 0 \\ \int_{i-\frac{1}{2}}^{i+\frac{1}{2}} -w(t) dt < 0 & i = 1, 2, \dots, N \end{cases} \quad (81)$$

$$\hat{R}(i) = \begin{cases} \int_{i-\frac{1}{2}}^{i+\frac{1}{2}} w(-t) dt > 0 & i = -N, -N+1, \dots, -1 \\ \int_{-\frac{1}{2}}^{\frac{1}{2}} w(|t|) dt - 2 \int_{-\frac{1}{2}}^{\frac{1}{2}} \delta(t) dt = 2 \int_0^{\frac{1}{2}} w(t) dt - 2 < 0 & i = 0 \\ \int_{i-\frac{1}{2}}^{i+\frac{1}{2}} w(t) dt > 0 & i = 1, 2, \dots, N \end{cases} \quad (82)$$

And we have  $\hat{T}(i) = -\hat{T}(-i)$ ,  $\hat{R}(i) = \hat{R}(-i)$ . Besides, from Formula (20), it is clear that:

$$\begin{aligned} \sum_{i=-N}^N \hat{T}(i) &= \int_{-N-\frac{1}{2}}^{N+\frac{1}{2}} T(t) dt = 0 \\ \sum_{i=-N}^N \hat{R}(i) &= \int_{-N-\frac{1}{2}}^{N+\frac{1}{2}} R(t) dt = 0 \end{aligned} \quad (83)$$

which means that for constant signals, the TGD results are constant at 0. After normalizing the discrete TGD operator here by adjusting the normalization constant ( $C_1$  and  $C_2$ ), it follows:

$$\left| \sum_{i=-N}^{-1} \hat{T}(i) \right| = \left| \sum_{i=1}^N \hat{T}(i) \right| = \left| \sum_{i=-N}^{-1} \hat{R}(i) \right| = \left| \sum_{i=1}^N \hat{R}(i) \right| = 1 \quad (84)$$

where  $|\cdot|$  denotes the absolute value. Combining Formula (83) and Formula (84), we get  $\hat{T}(0) = 0$  and  $\hat{R}(0) = -2$ . Furthermore, as the kernel function  $w$  for constructing the TGD operators  $T$  and  $R$  satisfies the Monotonic Constraint, we have:

$$\begin{aligned} |\hat{T}(i)| > |\hat{T}(j)| > 0, \quad 0 < |i| < |j| \leq N \\ \hat{R}(i) > \hat{R}(j) > 0, \quad 0 < |i| < |j| \leq N \end{aligned} \quad (85)$$

Towards practicality and simplicity, the discrete operator weights can be obtained through a direct discrete sampling of the kernel function without the requirement for intricate interval integration (Formula (81) and Formula (82)). As shown in Figure 23, if the kernel size is much larger than the sampling step, meaning that  $N$  is significantly larger than 1, then the interval integral of a kernel function is equal to the discrete sampling of another kernel function having the same form. Therefore, we can obtain the discrete TGD operators in the following way:

$$\hat{T}(i) = \begin{cases} \frac{T(i)}{|\sum_{j=-N}^{-1} T(j)|} = \frac{w(-i)}{\sum_{j=1}^N w(j)} & i = -N, -N+1, \dots, -1 \\ 0 & i = 0 \\ \frac{T(i)}{|\sum_{j=1}^N T(j)|} = \frac{-w(i)}{\sum_{j=1}^N w(j)} & i = 1, 2, \dots, N-1, N \end{cases} \quad (86)$$

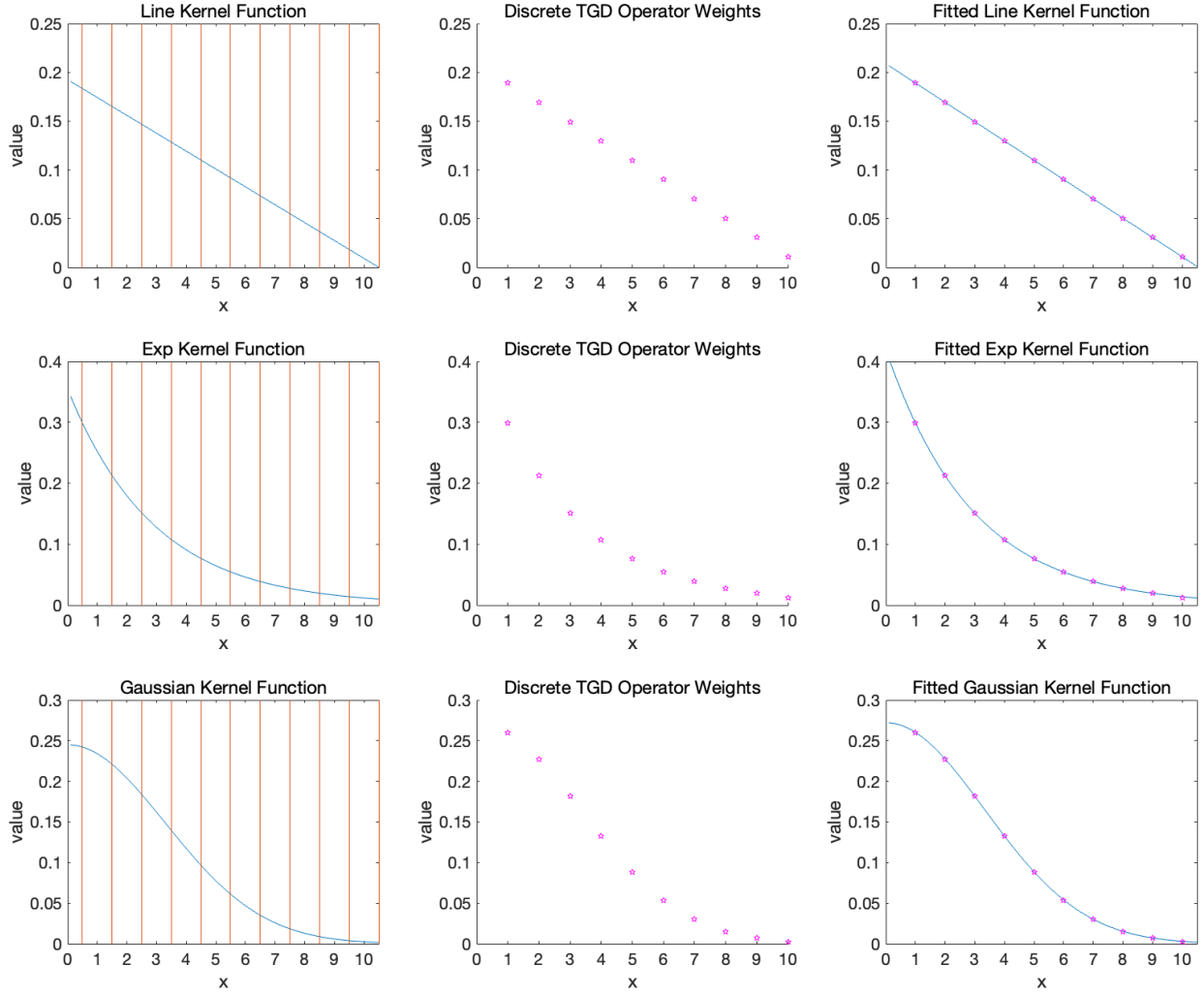


Figure 23: Schematic diagram of discrete TGD operator weight value acquisition. Since the Weibull kernel function is similar in shape to the Exponential kernel function, and the Landau kernel function is similar in shape to the Gaussian kernel function, we choose the simpler exponential and Gaussian as examples. First column: the initially selected kernel function, where the area between two adjacent red lines is the integral interval for obtaining the weight of the discrete TGD operator. Second column: the weight value of the discrete TGD operator obtained by segmental integrating the initial kernel function, which has been normalized to sum to 1. Third column: the weight value of the discrete TGD operator obtained by segmental integration is equivalent to the sampled value from another kernel function of the same form.

$$\hat{R}(i) = \begin{cases} \frac{R(i)}{|\sum_{j=-N}^{-1} R(j)|} = \frac{w(-i)}{\sum_{j=1}^N w(j)} & i = -N, -N+1, \dots, -1 \\ -2 & i = 0 \\ \frac{R(i)}{|\sum_{j=1}^N R(j)|} = \frac{w(i)}{\sum_{j=1}^N w(j)} & i = 1, 2, \dots, N-1, N \end{cases} \quad (87)$$

where  $w$  is the kernel function of TGD, which can be found in Section 1.3 for specific examples.

Finally, the discrete TGD operators  $\hat{T}$  and  $\hat{R}$  with  $2N + 1$  elements have the following form.

$$\begin{aligned} \hat{T} &= [\hat{w}_N \quad \hat{w}_{N-1} \quad \dots \quad \hat{w}_1 \quad 0 \quad -\hat{w}_1 \quad \dots \quad -\hat{w}_{N-1} \quad -\hat{w}_N] \\ \hat{R} &= [\hat{w}_N \quad \hat{w}_{N-1} \quad \dots \quad \hat{w}_1 \quad -2 \quad \hat{w}_1 \quad \dots \quad \hat{w}_{N-1} \quad \hat{w}_N] \end{aligned} \quad (88)$$

where:

$$\hat{w}_i = \frac{w(i)}{\sum_{j=1}^N w(j)}, \quad i = 1, 2, \dots, N-1, N \quad (89)$$

and:

$$\begin{aligned} \sum_{i=1}^N \hat{w}_i &= 1 \\ \hat{w}_i &> \hat{w}_j, \quad 0 < i < j \leq N \end{aligned} \quad (90)$$

In practical applications, it is generally acceptable to ignore the normalization factors ( $C_1$  and  $C_2$ ) and compute the discrete TGD through convolution after obtaining the operators ( $\hat{T}$  and  $\hat{R}$ ).

Here, we provide several examples of discrete TGD operators. First of all, let us consider a special case where the kernel size of TGD is exactly equal to the discrete step, i.e.,  $N = 1$ . According to Formula (86), (87) and (88), regardless of the kernel function used, only a unique operator is obtained:

$$\begin{aligned} \hat{T} &= [1 \quad 0 \quad -1] \\ \hat{R} &= [1 \quad -2 \quad 1] \end{aligned} \quad (91)$$

These are the traditional first-order and second-order central difference. However, the requirement “ $N$  is significantly larger than 1” is not met and the *Monotonic Constraint* is broken. This means that the central difference is not discrete TGD and does not have the properties of TGD operators, such as noise suppression.

Actually, the contribution of TGD is to provide larger-size operators constructed using specialized kernel functions. We showcase examples of 1st- and 2nd-order discrete TGD operators constructed with linear, exponential, Gaussian kernel functions, and kernel size  $N = 5$  and 7 respectively, as seen in Formula (92) and (93). These TGD operators can be conveniently used as convolution kernels for discrete TGD calculation.

$$\begin{aligned} \hat{T}_{\text{line}} &= \frac{1}{35} [1 \quad 4 \quad 7 \quad 10 \quad 13 \quad 0 \quad -13 \quad -10 \quad -7 \quad -4 \quad -1] \\ \hat{T}_{\text{exp}} &= \frac{1}{42} [1 \quad 2 \quad 4 \quad 11 \quad 24 \quad 0 \quad -24 \quad -11 \quad -4 \quad -2 \quad -1] \\ \hat{T}_{\text{Gaussian}} &= \frac{1}{62} [1 \quad 4 \quad 12 \quad 25 \quad 40 \quad 0 \quad -40 \quad -25 \quad -12 \quad -4 \quad -1] \\ \hat{R}_{\text{line}} &= \frac{1}{35} [1 \quad 4 \quad 7 \quad 10 \quad 13 \quad -70 \quad 13 \quad 10 \quad 7 \quad 4 \quad 1] \\ \hat{R}_{\text{exp}} &= \frac{1}{42} [1 \quad 2 \quad 4 \quad 11 \quad 24 \quad -84 \quad 24 \quad 11 \quad 4 \quad 2 \quad 1] \\ \hat{R}_{\text{Gaussian}} &= \frac{1}{62} [1 \quad 4 \quad 12 \quad 20 \quad 25 \quad -124 \quad 25 \quad 20 \quad 12 \quad 4 \quad 1] \end{aligned} \quad (92)$$

$$\begin{aligned} \hat{T}_{\text{line}} &= \frac{1}{91} [1 \quad 5 \quad 9 \quad 13 \quad 17 \quad 21 \quad 25 \quad 0 \quad -25 \quad -21 \quad -17 \quad -13 \quad -9 \quad -5 \quad -1] \\ \hat{T}_{\text{exp}} &= \frac{1}{42} [1 \quad 2 \quad 4 \quad 8 \quad 16 \quad 33 \quad 67 \quad 0 \quad -67 \quad -33 \quad -16 \quad -8 \quad -4 \quad -2 \quad -1] \\ \hat{T}_{\text{Gaussian}} &= \frac{1}{131} [1 \quad 3 \quad 8 \quad 18 \quad 32 \quad 50 \quad 64 \quad 0 \quad -64 \quad -50 \quad -32 \quad -18 \quad -8 \quad -3 \quad -1] \\ \hat{R}_{\text{line}} &= \frac{1}{91} [1 \quad 5 \quad 9 \quad 13 \quad 17 \quad 21 \quad 25 \quad -182 \quad 25 \quad 21 \quad 17 \quad 13 \quad 9 \quad 5 \quad 1] \\ \hat{R}_{\text{exp}} &= \frac{1}{131} [1 \quad 2 \quad 4 \quad 8 \quad 16 \quad 33 \quad 67 \quad -262 \quad 67 \quad 33 \quad 16 \quad 8 \quad 4 \quad 2 \quad 1] \\ \hat{R}_{\text{Gaussian}} &= \frac{1}{178} [1 \quad 3 \quad 8 \quad 18 \quad 32 \quad 50 \quad 64 \quad -356 \quad 64 \quad 50 \quad 32 \quad 18 \quad 8 \quad 3 \quad 1] \end{aligned} \quad (93)$$

### 3.3 High-Dimensional Discrete TGD and Operators

Now let us direct our attention toward the high-dimensional scenario. Similar to the one-dimensional case, we transform the discrete signal into a continuous function by representing it as a step function, where each constant piece corresponds

to a discrete value point. For a  $m$ -dimensional discrete signal  $X$ , the corresponding step function can be expressed as follows:

$$\hat{f}(x_1, x_2, \dots, x_m) \triangleq X(n_1, n_2, \dots, n_m) \quad x_i \in (n_i - \frac{1}{2}, n_i + \frac{1}{2}] \quad (94)$$

where  $n_i \in \mathbb{Z}$ . We express the TGD of the discrete signal as the TGD (Formula (51) and (55)) of the corresponding step function (Formula (94)) at sampling locations:

$$\begin{aligned} \frac{\partial_{\text{TGD}} X}{\partial \mathbf{v}}(n_1, n_2, \dots, n_m) &\triangleq \frac{\partial_{\text{TGD}} \hat{f}}{\partial \mathbf{v}}(n_1, n_2, \dots, n_m) \\ \frac{\partial_{\text{TGD}}^2 X}{\partial \mathbf{v}^2}(n_1, n_2, \dots, n_m) &\triangleq \frac{\partial_{\text{TGD}}^2 \hat{f}}{\partial \mathbf{v}^2}(n_1, n_2, \dots, n_m) \end{aligned} \quad (95)$$

It is easily obtained that the TGD of a high-dimensional discrete signal remains equal to the convolution of the discrete signal with high-dimensional discrete TGD operators, obeying *Difference-by-Convolution*:

$$\begin{aligned} \hat{T}(i_1, i_2, \dots, i_m) &= \int_{i_m - \frac{1}{2}}^{i_m + \frac{1}{2}} \dots \int_{i_1 - \frac{1}{2}}^{i_1 + \frac{1}{2}} \tilde{T}(x_1, x_2, \dots, x_m) dx_1 \dots dx_m \\ \hat{R}(i_1, i_2, \dots, i_m) &= \int_{i_m - \frac{1}{2}}^{i_m + \frac{1}{2}} \dots \int_{i_1 - \frac{1}{2}}^{i_1 + \frac{1}{2}} \tilde{R}(x_1, x_2, \dots, x_m) dx_1 \dots dx_m \\ i_j &= -N, -N + 1, \dots, N - 1, N \quad j = 1, 2, \dots, m \end{aligned} \quad (96)$$

where  $\tilde{T}$  and  $\tilde{R}$  are multivariate 1st- and 2nd-order TGD operators (See Section 2), and  $N$  is the *kernel size*. And each discrete TGD operator is composed of  $(2N + 1)^m$  elements. When the kernel size is substantially larger than the sampling step, the interval integral of  $\tilde{T}$  and  $\tilde{R}$  is approximately equal to the discrete sampling of  $\tilde{T}$  and  $\tilde{R}$ . Therefore, in practice, the discrete operator weights can be directly obtained by sampling the multivariate TGD operators without the need for intricate interval integration, as long as the sampled values are meaningful.

$$\begin{aligned} \hat{T}(i_1, i_2, \dots, i_m) &= \tilde{T}(i_1, i_2, \dots, i_m) \\ \hat{R}(i_1, i_2, \dots, i_m) &= \tilde{R}(i_1, i_2, \dots, i_m) \\ \widehat{\text{LoT}}(i_1, i_2, \dots, i_m) &= \text{LoT}(i_1, i_2, \dots, i_m) \end{aligned} \quad (97)$$

These operators are normalized to the sum of 0, which is derived directly by Formula (58) and (69). This guarantees that the TGD value remains constant at 0 for constant signals.

$$\begin{aligned} \sum_{i_m=-N}^N \dots \sum_{i_1=-N}^N \hat{T}(i_1, i_2, \dots, i_m) &= 0 \\ \sum_{i_m=-N}^N \dots \sum_{i_1=-N}^N \hat{R}(i_1, i_2, \dots, i_m) &= 0 \\ \sum_{i_m=-N}^N \dots \sum_{i_1=-N}^N \widehat{\text{LoT}}(i_1, i_2, \dots, i_m) &= 0 \end{aligned} \quad (98)$$

As discussed in Section 2.4, the orthogonal constructed operators can decouple dimensions to expedite calculations. Here, we demonstrate the 2D discrete TGD operators obtained using orthogonal TGD operators, with **violet** representing positive values and **blue** representing negative values. Without loss of generality, we display the case in which the  $x$ -axis direction is the differential direction.

$$\hat{T}_x = \begin{bmatrix} \hat{w}_{-N,-N} & \dots & \hat{w}_{-N,-1} & 0 & -\hat{w}_{-N,1} & \dots & -\hat{w}_{-N,N} \\ \hat{w}_{-N+1,-N} & \dots & \hat{w}_{-N+1,-1} & 0 & -\hat{w}_{-N+1,1} & \dots & -\hat{w}_{-N+1,N} \\ \dots & \dots & \dots & \dots & \dots & \dots & \dots \\ \hat{w}_{-1,-N} & \dots & \hat{w}_{-1,-1} & 0 & -\hat{w}_{-1,1} & \dots & -\hat{w}_{-1,N} \\ \hat{w}_{0,-N} & \dots & \hat{w}_{0,-1} & 0 & -\hat{w}_{0,1} & \dots & -\hat{w}_{0,N} \\ \hat{w}_{1,-N} & \dots & \hat{w}_{1,-1} & 0 & -\hat{w}_{1,1} & \dots & -\hat{w}_{1,N} \\ \dots & \dots & \dots & \dots & \dots & \dots & \dots \\ \hat{w}_{N-1,-N} & \dots & \hat{w}_{N-1,-1} & 0 & -\hat{w}_{N-1,1} & \dots & -\hat{w}_{N-1,N} \\ \hat{w}_{N,-N} & \dots & \hat{w}_{N,-1} & 0 & -\hat{w}_{N,1} & \dots & -\hat{w}_{N,N} \end{bmatrix} \quad (99)$$

$$\widehat{R}_x = \begin{bmatrix} \widehat{w}_{-N,-N} & \cdots & \widehat{w}_{-N,-1} & -\widehat{w}_{-N,0} & \widehat{w}_{-N,1} & \cdots & \widehat{w}_{-N,N} \\ \widehat{w}_{-N+1,-N} & \cdots & \widehat{w}_{-N+1,-1} & -\widehat{w}_{-N+1,0} & \widehat{w}_{-N+1,1} & \cdots & \widehat{w}_{-N+1,N} \\ \cdots & \cdots & \cdots & \cdots & \cdots & \cdots & \cdots \\ \widehat{w}_{-1,-N} & \cdots & \widehat{w}_{-1,-1} & -\widehat{w}_{-1,0} & \widehat{w}_{-1,1} & \cdots & \widehat{w}_{-1,N} \\ \widehat{w}_{0,-N} & \cdots & \widehat{w}_{0,-1} & -\widehat{w}_{0,0} & \widehat{w}_{0,1} & \cdots & \widehat{w}_{0,N} \\ \widehat{w}_{1,-N} & \cdots & \widehat{w}_{1,-1} & -\widehat{w}_{1,0} & \widehat{w}_{1,1} & \cdots & \widehat{w}_{1,N} \\ \cdots & \cdots & \cdots & \cdots & \cdots & \cdots & \cdots \\ \widehat{w}_{N-1,-N} & \cdots & \widehat{w}_{N-1,-1} & -\widehat{w}_{N-1,0} & \widehat{w}_{N-1,1} & \cdots & \widehat{w}_{N-1,N} \\ \widehat{w}_{N,-N} & \cdots & \widehat{w}_{N,-1} & -\widehat{w}_{N,0} & \widehat{w}_{N,1} & \cdots & \widehat{w}_{N,N} \end{bmatrix} \quad (100)$$

where:

$$\begin{aligned} \widehat{w}_{-i,-j} &= \widehat{w}_{-i,j} = \widehat{w}_{i,-j} = \widehat{w}_{i,j} > 0 \\ \widehat{w}_{i,|j|} &> \widehat{w}_{i,|k|} \quad 0 < |j| < |k| \leq N \\ \widehat{w}_{|i|,j} &> \widehat{w}_{|k|,j} \quad 0 < |i| < |k| \leq N \\ \widehat{w}_{i,0} &= \sum_{j=-N}^{-1} \widehat{R}_x(i,j) + \sum_{j=1}^N \widehat{R}_x(i,j) \end{aligned} \quad (101)$$

And the unified form of the 2D discrete LoT operators are:

$$\widehat{\text{LoT}} = \begin{bmatrix} \widehat{w}_{-N,-N} & \cdots & \widehat{w}_{-N,-1} & \widehat{w}_{-N,0} & \widehat{w}_{-N,1} & \cdots & \widehat{w}_{-N,N} \\ \widehat{w}_{-N+1,-N} & \cdots & \widehat{w}_{-N+1,-1} & \widehat{w}_{-N+1,0} & \widehat{w}_{-N+1,1} & \cdots & \widehat{w}_{-N+1,N} \\ \cdots & \cdots & \cdots & \cdots & \cdots & \cdots & \cdots \\ \widehat{w}_{-1,-N} & \cdots & \widehat{w}_{-1,-1} & \widehat{w}_{-1,0} & \widehat{w}_{-1,1} & \cdots & \widehat{w}_{-1,N} \\ \widehat{w}_{0,-N} & \cdots & \widehat{w}_{0,-1} & -\widehat{w}_{0,0} & \widehat{w}_{0,1} & \cdots & \widehat{w}_{0,N} \\ \widehat{w}_{1,-N} & \cdots & \widehat{w}_{1,-1} & \widehat{w}_{1,0} & \widehat{w}_{1,1} & \cdots & \widehat{w}_{1,N} \\ \cdots & \cdots & \cdots & \cdots & \cdots & \cdots & \cdots \\ \widehat{w}_{N-1,-N} & \cdots & \widehat{w}_{N-1,-1} & \widehat{w}_{N-1,0} & \widehat{w}_{N-1,1} & \cdots & \widehat{w}_{N-1,N} \\ \widehat{w}_{N,-N} & \cdots & \widehat{w}_{N,-1} & \widehat{w}_{N,0} & \widehat{w}_{N,1} & \cdots & \widehat{w}_{N,N} \end{bmatrix} \quad (102)$$

where:

$$\begin{aligned} \widehat{w}_{-i,-j} &= \widehat{w}_{-i,j} = \widehat{w}_{i,-j} = \widehat{w}_{i,j} > 0 \\ \widehat{w}_{i,|j|} &> \widehat{w}_{i,|k|} \quad 0 < |j| < |k| \leq N \\ \widehat{w}_{|i|,j} &> \widehat{w}_{|k|,j} \quad 0 < |i| < |k| \leq N \\ \sum_{i=-N}^N \sum_{j=-N}^N \widehat{\text{LoT}}(i,j) &= 0 \end{aligned} \quad (103)$$

In addition, by choosing different multivariate TGD operators, high-dimensional discrete signals can be calculated for directional TGD, partial TGD, and Laplace TGD. Likewise, Sobel operator, Sobel-Feldman operator, Scharr operator, and Laplacian operator can be derived from the formulas for  $N=1$ . However, these classic operators are not discrete TGD operators and lack the properties of TGD operators, such as noise suppression.

Similarly, the classic discrete differential operators, such as the Sobel operator [23], Sobel-Feldman operator [24], Scharr operator [25], and Laplacian operator [26], can be derived from the Formula (99), (101) for  $N = 1$ . However, these classic operators are not discrete TGD operators, and lack the properties of TGD operators such as noise suppression (Figure 38).

Here, we present several examples of 2D discrete TGD operators orthogonal constructed with the Gaussian kernel function and kernel size  $N = 6$ , including 1st- and 2nd-order discrete TGD operators ( $\widehat{T}_x$  and  $\widehat{R}_x$ ) in the  $x$ -axis direction. We obtain them by sampling and normalizing the orthogonal TGD operators, respectively. Additionally, we provide two examples of discrete TGD operators oriented 45 degrees from the  $x$ -axis ( $\widehat{T}_{45'}$  and  $\widehat{R}_{45'}$ ). An anisotropic discrete LoT operator ( $\widehat{\text{LoT}}$ ) is also provided. The operator values can be found in Formula (104) to (108). By adjusting the kernel function and its parameters, a wide variety of discrete TGD operators can be constructed to satisfy varying task requirements.

More intuitively, Figure 24 presents a visual representation of the above four operators, in which red and blue respectively indicate positive and negative values. The darker the color, the larger the absolute value. Figure 25 provides a schematic diagram of 3D discrete TGD operators with a size of  $15 \times 15 \times 15$  ( $N = 7$ ), which are used for partial TGD calculation when the  $z$ -variable is involved. These discrete TGD operators can be used as convolution kernels for discrete TGD

calculation, as well as serve downstream tasks including video or image sequence gradient calculations in computer vision. And the excellent performance of discrete TGD operators will be verified in subsequent experiments.

$$\widehat{T}_x = \begin{bmatrix} 1 & 3 & 7 & 16 & 27 & 37 & 0 & -37 & -27 & -16 & -7 & -3 & -1 \\ 3 & 11 & 28 & 58 & 98 & 133 & 0 & -133 & -98 & -58 & -28 & -11 & -3 \\ 10 & 33 & 84 & 174 & 292 & 398 & 0 & -398 & -292 & -174 & -84 & -33 & -19 \\ 26 & 83 & 211 & 435 & 729 & 994 & 0 & -994 & -729 & -435 & -211 & -83 & -26 \\ 56 & 174 & 442 & 912 & 1529 & 2085 & 0 & -2085 & -1529 & -912 & -442 & -174 & -56 \\ 99 & 311 & 788 & 1625 & 2725 & 3715 & 0 & -3715 & -2725 & -1625 & -788 & -311 & -99 \\ 153 & 478 & 1211 & 2496 & 4184 & 5705 & 0 & -5705 & -4184 & -2496 & -1211 & -478 & -153 \\ 99 & 311 & 788 & 1625 & 2725 & 3715 & 0 & -3715 & -2725 & -1625 & -788 & -311 & -99 \\ 56 & 174 & 442 & 912 & 1529 & 2085 & 0 & -2085 & -1529 & -912 & -442 & -174 & -56 \\ 26 & 83 & 211 & 435 & 729 & 994 & 0 & -994 & -729 & -435 & -211 & -83 & -26 \\ 10 & 33 & 84 & 174 & 292 & 398 & 0 & -398 & -292 & -174 & -84 & -33 & -19 \\ 3 & 11 & 28 & 58 & 98 & 133 & 0 & -133 & -98 & -58 & -28 & -11 & -3 \\ 1 & 3 & 7 & 16 & 27 & 37 & 0 & -37 & -27 & -16 & -7 & -3 & -1 \end{bmatrix} \quad (104)$$

$$\widehat{R}_x = \begin{bmatrix} 1 & 3 & 7 & 16 & 27 & 37 & -182 & 37 & 27 & 16 & 7 & 3 & 1 \\ 3 & 11 & 28 & 58 & 98 & 133 & -662 & 133 & 98 & 58 & 28 & 11 & 3 \\ 10 & 33 & 84 & 174 & 292 & 398 & -1982 & 398 & 292 & 174 & 84 & 33 & 19 \\ 26 & 83 & 211 & 435 & 729 & 994 & -4956 & 994 & 729 & 435 & 211 & 83 & 26 \\ 56 & 174 & 442 & 912 & 1529 & 2085 & -10396 & 2085 & 1529 & 912 & 442 & 174 & 56 \\ 99 & 311 & 788 & 1625 & 2725 & 3715 & -18526 & 3715 & 2725 & 1625 & 788 & 311 & 99 \\ 153 & 478 & 1211 & 2496 & 4184 & 5705 & -28454 & 5705 & 4184 & 2496 & 1211 & 478 & 153 \\ 99 & 311 & 788 & 1625 & 2725 & 3715 & -18526 & 3715 & 2725 & 1625 & 788 & 311 & 99 \\ 56 & 174 & 442 & 912 & 1529 & 2085 & -10396 & 2085 & 1529 & 912 & 442 & 174 & 56 \\ 26 & 83 & 211 & 435 & 729 & 994 & -4956 & 994 & 729 & 435 & 211 & 83 & 26 \\ 10 & 33 & 84 & 174 & 292 & 398 & -1982 & 398 & 292 & 174 & 84 & 33 & 19 \\ 3 & 11 & 28 & 58 & 98 & 133 & -662 & 133 & 98 & 58 & 28 & 11 & 3 \\ 1 & 3 & 7 & 16 & 27 & 37 & -182 & 37 & 27 & 16 & 7 & 3 & 1 \end{bmatrix} \quad (105)$$

$$\widehat{T}_{45'} = \begin{bmatrix} 0 & -1 & -2 & -6 & -11 & -17 & -21 & -20 & -18 & -12 & -7 & -3 & -1 \\ 1 & 0 & -9 & -21 & -39 & -60 & -75 & -78 & -67 & -48 & -28 & -14 & -3 \\ 2 & 9 & 0 & -59 & -111 & -172 & -220 & -233 & -204 & -150 & -92 & -28 & -7 \\ 6 & 21 & 59 & 0 & -261 & -410 & -532 & -575 & -518 & -392 & -150 & -48 & -12 \\ 11 & 39 & 111 & 261 & 0 & -805 & -1069 & -1184 & -1101 & -518 & -204 & -67 & -18 \\ 17 & 60 & 172 & 410 & 805 & 0 & -1791 & -2047 & -1184 & -575 & -233 & -78 & -20 \\ 21 & 75 & 220 & 532 & 1069 & 1791 & 0 & -1791 & -1069 & -532 & -220 & -75 & -21 \\ 20 & 78 & 233 & 575 & 1184 & 2047 & 1791 & 0 & -805 & -410 & -172 & -60 & -17 \\ 18 & 67 & 204 & 518 & 1101 & 1184 & 1069 & 805 & 0 & -261 & -111 & -39 & -11 \\ 12 & 48 & 150 & 392 & 518 & 575 & 532 & 410 & 261 & 0 & -59 & -21 & -6 \\ 7 & 28 & 92 & 150 & 204 & 233 & 220 & 172 & 111 & 59 & 0 & -9 & -2 \\ 3 & 14 & 28 & 48 & 67 & 78 & 75 & 60 & 39 & 21 & 9 & 0 & -1 \\ 1 & 3 & 7 & 12 & 18 & 20 & 21 & 17 & 11 & 6 & 2 & 1 & 0 \end{bmatrix} \quad (106)$$

$$\widehat{R}_{45'} = \begin{bmatrix} -1 & 1 & 2 & 6 & 11 & 17 & 21 & 20 & 18 & 12 & 7 & 3 & 1 \\ 1 & -22 & 9 & 21 & 39 & 60 & 75 & 78 & 67 & 48 & 28 & 14 & 3 \\ 2 & 9 & -171 & 59 & 111 & 172 & 220 & 233 & 204 & 150 & 92 & 28 & 7 \\ 6 & 21 & 59 & -903 & 261 & 410 & 532 & 575 & 518 & 392 & 150 & 48 & 12 \\ 11 & 39 & 111 & 261 & -3318 & 805 & 1069 & 1184 & 1101 & 518 & 204 & 67 & 18 \\ 17 & 60 & 172 & 410 & 805 & -8656 & 1791 & 2047 & 1184 & 575 & 233 & 78 & 20 \\ 21 & 75 & 220 & 532 & 1069 & 1791 & -16500 & 1791 & 1069 & 532 & 220 & 75 & 21 \\ 20 & 78 & 233 & 575 & 1184 & 2047 & 1791 & -8656 & 805 & 410 & 172 & 60 & 17 \\ 18 & 67 & 204 & 518 & 1101 & 1184 & 1069 & 805 & -3318 & 261 & 111 & 39 & 11 \\ 12 & 48 & 150 & 392 & 518 & 575 & 532 & 410 & 261 & -903 & 59 & 21 & 6 \\ 7 & 28 & 92 & 150 & 204 & 233 & 220 & 172 & 111 & 59 & -171 & 9 & 2 \\ 3 & 14 & 28 & 48 & 67 & 78 & 75 & 60 & 39 & 21 & 9 & -22 & 1 \\ 1 & 3 & 7 & 12 & 18 & 20 & 21 & 17 & 11 & 6 & 2 & 1 & -1 \end{bmatrix} \quad (107)$$

$$\widehat{\text{LoT}} = \begin{bmatrix} 1 & 3 & 7 & 16 & 27 & 37 & 41 & 37 & 27 & 16 & 7 & 3 & 1 \\ 3 & 9 & 24 & 50 & 84 & 115 & 128 & 115 & 84 & 50 & 24 & 9 & 3 \\ 7 & 24 & 62 & 128 & 215 & 293 & 325 & 293 & 215 & 128 & 62 & 24 & 7 \\ 16 & 50 & 128 & 264 & 443 & 604 & 670 & 604 & 443 & 264 & 128 & 50 & 16 \\ 27 & 84 & 215 & 443 & 743 & 1013 & 1124 & 1013 & 743 & 443 & 215 & 84 & 27 \\ 37 & 115 & 293 & 604 & 1013 & 1382 & 1532 & 1382 & 1013 & 604 & 293 & 115 & 37 \\ 41 & 128 & 325 & 670 & 1124 & 1532 & -49596 & 1532 & 1124 & 670 & 325 & 128 & 41 \\ 37 & 115 & 293 & 604 & 1013 & 1382 & 1532 & 1382 & 1013 & 604 & 293 & 115 & 37 \\ 27 & 84 & 215 & 443 & 743 & 1013 & 1124 & 1013 & 743 & 443 & 215 & 84 & 27 \\ 16 & 50 & 128 & 264 & 443 & 604 & 670 & 604 & 443 & 264 & 128 & 50 & 16 \\ 7 & 24 & 62 & 128 & 215 & 293 & 325 & 293 & 215 & 128 & 62 & 24 & 7 \\ 3 & 9 & 24 & 50 & 84 & 115 & 128 & 115 & 84 & 50 & 24 & 9 & 3 \\ 1 & 3 & 7 & 16 & 27 & 37 & 41 & 37 & 27 & 16 & 7 & 3 & 1 \end{bmatrix} \quad (108)$$

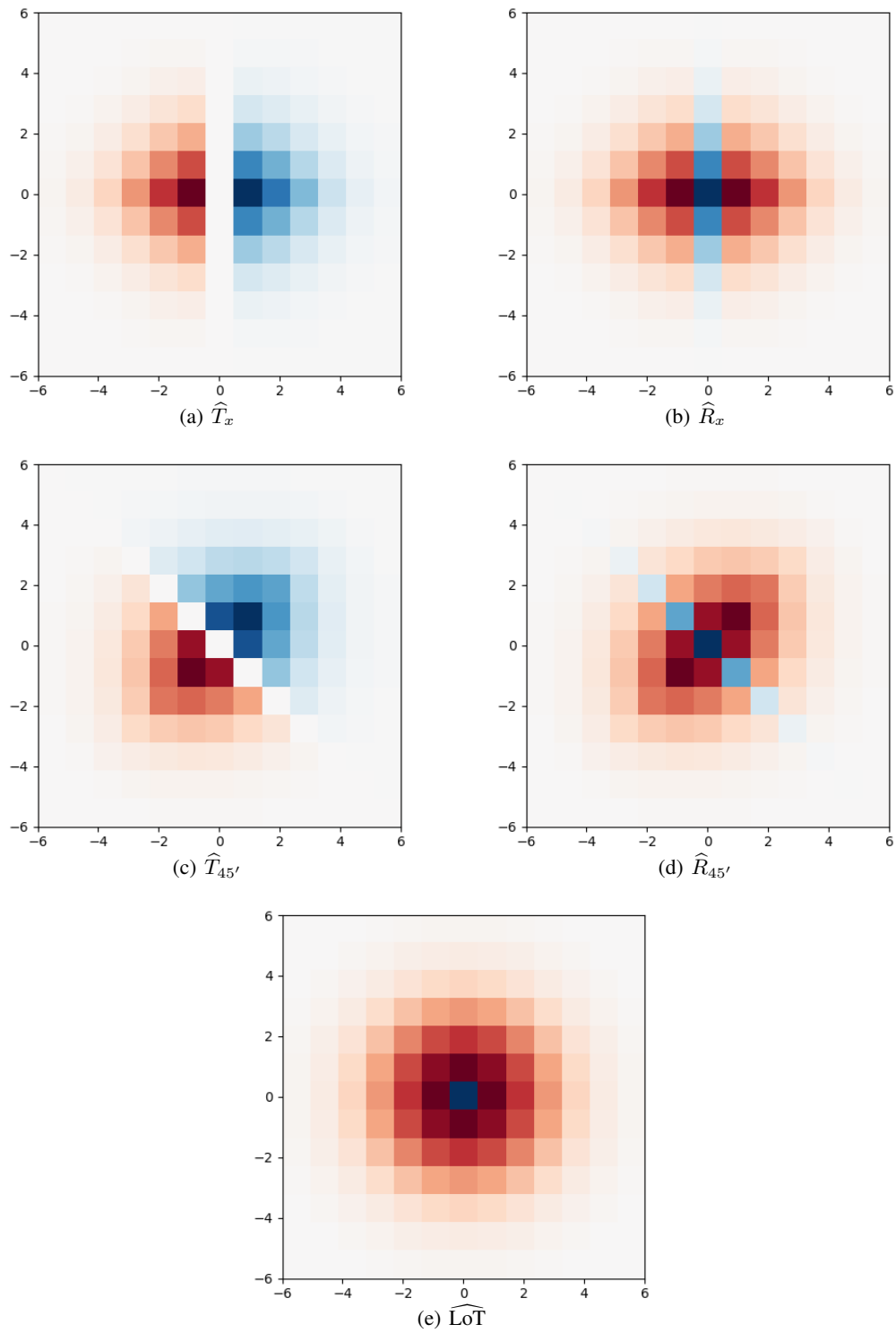
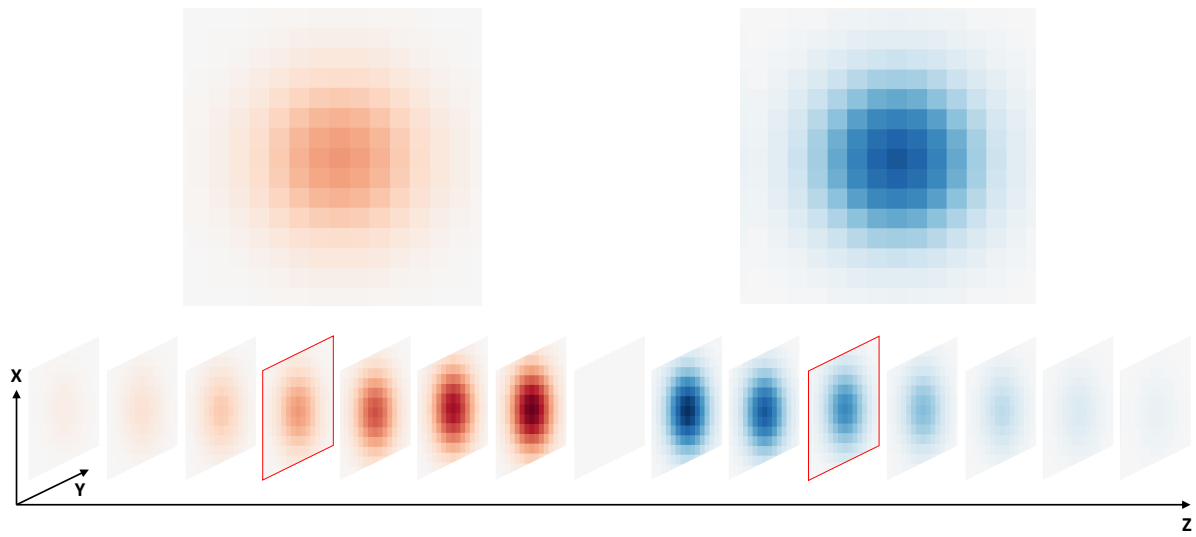
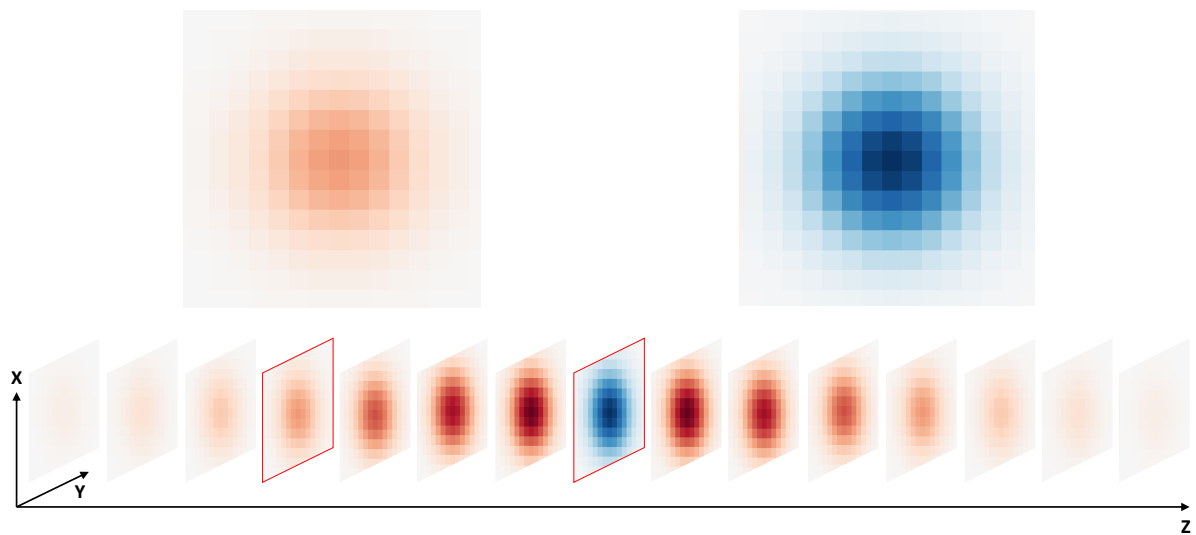


Figure 24: Visualization of a 2D discrete TGD operators. The operator values can be found in Formula (104) to (108).



(a) 3D 1st-order discrete TGD operator  $\hat{T}_z$



(b) 3D 2nd-order discrete TGD operator  $\hat{R}_z$

Figure 25: Visualization of a 3D discrete TGD operators based on the orthogonal construction method. The red box marks the cross-section of the operator for the enlarged visualization.

## 4 The Application of TGD in Signal Denoise

### 4.1 TGD-Based Signal Denoise Algorithm

In signal processing, sampling is the reduction of a continuous-time signal to a discrete-time signal, in which the inevitable noise overlays complex irregularities and corrupts the signals. Denoising is the process of extracting signals from a combination of signals and noise, thus preserving critical information that is essential in various applications. The smoothing assumption is reasonable for discrete signals<sup>2</sup> and it enables pattern forecast and provides both flexible and robust data analysis [27]. In this sense, in the context of one-dimensional data, signal smoothing and signal denoising can be used interchangeably [28].

Among a plethora of data smoothing techniques, the most intuitive method is probably moving average [29] or convolution smoothing [30]. To form a smoothed sequence, each noisy datum is replaced with a weighted average of its neighboring data. In terms of implementation, the noisy sequence is convolved with a smoothing kernel such as the Gaussian [31]. From a frequency point of view, convolution smoothing is low-pass filtering, which occurs in the frequency domain, and the smoothing kernel represents the impulse response of the filter. Normally, the signal is band-limited, and the noise mainly appears in the high-frequency domain. Therefore, a low-pass filter can effectively eliminate most of the noise. Low-pass filtering inspires the Fourier thresholding technique [32], which eliminates the high-frequency components that fall below a certain threshold, as they are likely to be noise.

Alongside the Fourier transform, the wavelet transform is another effective tool in signal processing that decomposes the input sequence into local oscillatory components [33]. And wavelet shrinkage [31, 34], like Fourier thresholding, modifies wavelet coefficients based on specific criteria to achieve noise suppression for noisy sequences.

A one-dimensional data denoising approach that utilizes singular-value decomposition (SVD) has recently gained considerable popularity [28]. The process begins with mapping the noisy signal to a partial circulant matrix. By using the singular-value decomposition of the matrix, components associated with the signal can be identified by reviewing the total variations of left singular vectors. A smoothed sequence is then reconstructed based on the low-rank approximation of the matrix containing only the signal components.

Lastly, a noteworthy mainstream technique is the total variation (TV) denoising [35, 36]. Unlike the aforementioned methods, TV denoising directly accounts for the continuity of the discrete signal, i.e., the difference between adjacent points. Specifically, given a noisy signal  $X = (x_1, \dots, x_N) \in \mathbb{R}^N$  of size  $N \geq 1$ , and we want to efficiently compute the denoised signal  $Y^* \in \mathbb{R}^N$ , defined implicitly as the solution to the minimization problem:

$$\underset{Y \in \mathbb{R}^N}{\text{minimize}} \sum_{i=1}^N (Y[i] - X[i])^2 + \lambda \left( \sum_{i=1}^{N-1} |Y[i+1] - Y[i]|^p \right)^{\frac{1}{p}} \quad (109)$$

where the regularization parameter  $\lambda \geq 0$ , and determines the similarity between the output signal and the input signal. Notice, when using  $\ell_1$  norm with  $p = 1$ , the function to minimize is strongly convex, and the solution  $Y^*$  to the problem exists and is unique whatever the noisy signal  $X$ . Some improved work [37, 38] recommend the use of  $\ell_2$  norm in place of  $\ell_1$  norm, resulting in improved performance, even though it leads to a non-convex optimization problem.

Actually, Formula (109) only imposes a constraint on the continuity of the sequence without any stipulations on its “derivative”. Consequently, TV denoising only approximates the output signal to a  $C^0$  function<sup>3</sup>, which is continuous but may lack smoothness due to its derivative not being continuous. Mathematically, a function must be smooth if its derivative is continuous. Therefore, intuitively, imposing a continuity constraint on the “derivative” of a discrete signal would result in a smoother denoised signal:

$$\underset{Y \in \mathbb{R}^N}{\text{minimize}} \sum_{i=1}^N (Y[i] - X[i])^2 + \lambda \left( \sum_{i=1}^{N-1} |Y'[i+1] - Y'[i]|^p \right)^{\frac{1}{p}} \quad (110)$$

However, the current forward, backward, and central difference schemes are all sensitive to noise. And the resulting difference sequence has an even lower signal-to-noise ratio (SNR). Therefore, smoothing a noisy difference sequence is more challenging than directly smoothing the given noisy signal.

<sup>2</sup>Mathematically, a discrete signal refers to an ordered sequence of real-valued numbers sampled from a smooth signal, while inevitable noise overlays the signal with complex irregularities that cause discontinuities.

<sup>3</sup>Consider an open set  $U$  on the real line and a function  $f$  defined on  $U$  with real values.  $k$  is a non-negative integer. The function  $f$  is said to be a  $C^k$  function if the derivatives  $f', \dots, f^{(k)}$  exist and are continuous on  $U$ . If  $f$  is a  $C^k$  function, then  $f$  must be a  $C^{k-1}$  function [39].

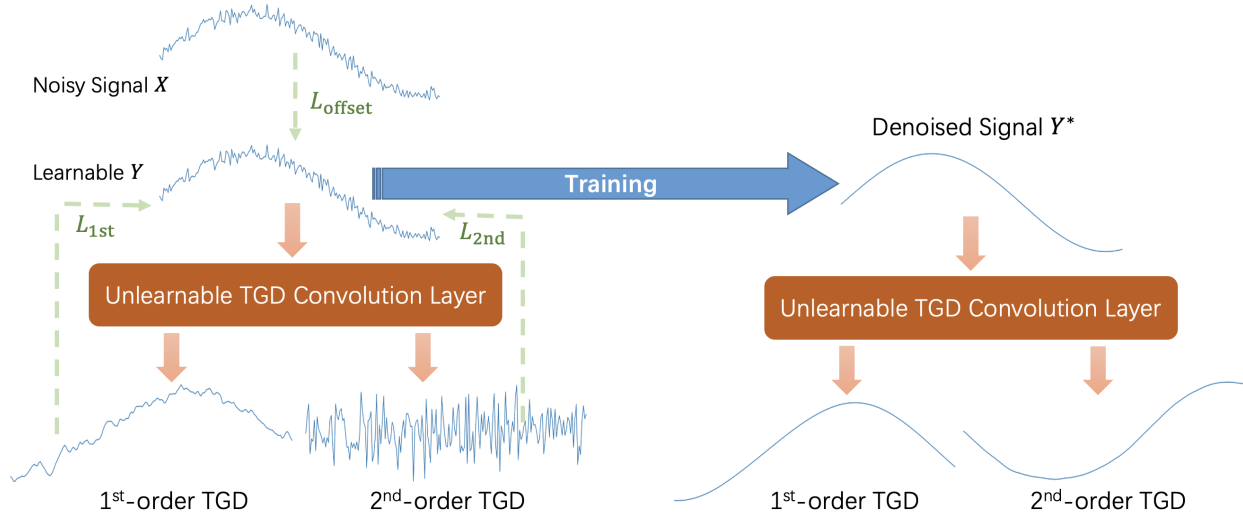


Figure 26: Schematic diagram of TGD-based signal denoise algorithm.

Improving the smoothness of denoised signals is a great challenge in the absence of robust noise-resistant methods for calculating discrete signal “derivative”. Fortunately, TGD can serve as a derivative representation of discrete signals, which extends the computational interval and offers some noise immunity. Moreover, the continuity of the General Difference results in sequence smoothness. Therefore, we can enhance the smoothness of the denoised signal by constraining the continuity of TGD. Naturally, the new minimization problem for our TGD-based signal denoise algorithm is expressed as follows:

$$\begin{aligned} \underset{Y \in \mathbb{R}^N}{\text{minimize}} \quad & \sum_{i=1}^N (Y[i] - X[i])^2 + \lambda_{1\text{st}} \left( \sum_{i=1}^{N-1} |Y'_{\text{TGD}}[i+1] - Y'_{\text{TGD}}[i]|^p \right)^{\frac{1}{p}} \\ & + \lambda_{2\text{nd}} \left( \sum_{i=1}^{N-1} |Y''_{\text{TGD}}[i+1] - Y''_{\text{TGD}}[i]|^p \right)^{\frac{1}{p}} \end{aligned} \quad (111)$$

where the regularization parameter  $\lambda_{1\text{st}} \geq 0$  and  $\lambda_{2\text{nd}} \geq 0$ . When  $\lambda_{1\text{st}} > 0$  and  $\lambda_{2\text{nd}} = 0$ , the first-order TGD of the output signal is required continuous and the denoised signal approximates a  $C^1$  function. When  $\lambda_{2\text{nd}} > 0$ , the first- and second-order TGDs of the output signal are required continuous and the denoised signal approximates a  $C^2$  function.

Although Formula (111) is non-convex, the Difference-by-Convolution mode of TGD helps us to solve this problem using a neural network with only a single convolutional layer. Figure 26 shows the schematic diagram of the TGD-based denoising algorithm. In terms of implementation, we first set the given noisy signal  $X$  of size  $N \geq 1$  as a learnable parameter matrix  $Y$  in the neural network. Then we give  $N_{1\text{st}}$  1D first-order discrete TGD operators and  $N_{2\text{nd}}$  second-order discrete TGD operators (examples in Formula (93)), and set them as non-learnable weights to a convolutional layer  $Conv$  with input channel of 1 and output channel of  $N_{1\text{st}} + N_{2\text{nd}}$ . TGD results are calculated by feeding the learnable matrix  $Y$  to the convolutional layer<sup>4</sup>:

$$\begin{aligned} Z &= Conv(Y) \\ Y'_{\text{TGD}} &= Z[1 : N_{1\text{st}}] \\ Y''_{\text{TGD}} &= Z[N_{1\text{st}} + 1 : N_{1\text{st}} + N_{2\text{nd}}] \end{aligned} \quad (112)$$

Next, we convert Formula (111) into loss functions for training the learnable denoised signal  $Y$ , which includes three parts: first-order TGD continuity loss  $L_{1\text{st}}$ , second-order TGD continuity loss  $L_{2\text{nd}}$ , and sampling point offset loss

<sup>4</sup>The batch dimension is ignored here to simplify the representation.

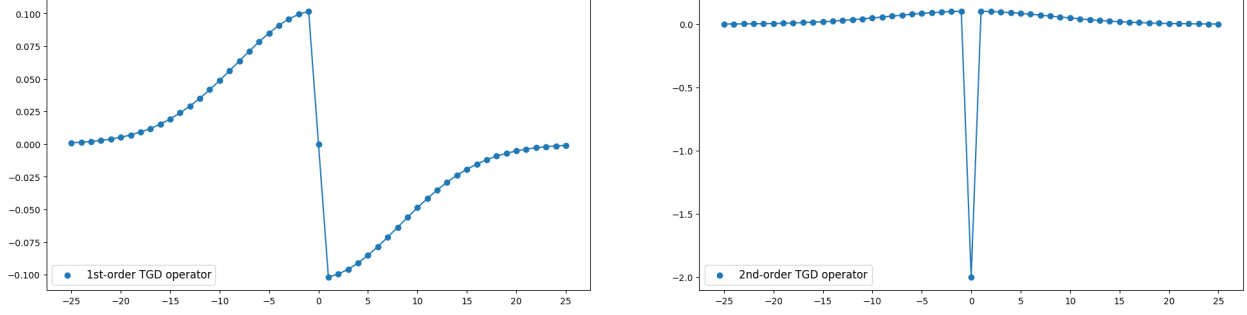


Figure 27: The discrete TGD operators used in the denoising experiments with size of 51, which are constructed based on the Gaussian kernel function.

$L_{\text{offset}}$ :

$$\begin{aligned}
 L_{1\text{st}} &= \sum_{i=1}^{N_{1\text{st}}} \left( \sum_{j=1}^{N-1} |Y'_{\text{TGD}}[i, j] - Y'_{\text{TGD}}[i, j+1]|^p \right)^{\frac{1}{p}} \\
 L_{2\text{nd}} &= \sum_{i=1}^{N_{2\text{nd}}} \left( \sum_{j=1}^{N-1} |Y''_{\text{TGD}}[i, j] - Y''_{\text{TGD}}[i, j+1]|^p \right)^{\frac{1}{p}} \\
 L_{\text{offset}} &= \sum_{i=1}^N (Y[i] - X[i])^2
 \end{aligned} \tag{113}$$

And the final loss function is expressed as follows:

$$L_{\text{final}} = \lambda_{1\text{st}} L_{1\text{st}} + \lambda_{2\text{nd}} L_{2\text{nd}} + \lambda_{\text{offset}} L_{\text{offset}} \tag{114}$$

where  $\lambda_{1\text{st}}$ ,  $\lambda_{2\text{nd}}$  and  $\lambda_{\text{offset}}$  are loss factors.  $L_{1\text{st}}$  and  $L_{2\text{nd}}$  contribute to the continuity of the TGD results for the denoised signal, resulting in a smoother denoised signal. Besides,  $L_{\text{offset}}$  facilitates the retention of similarity between the original and denoised signals. Iteratively optimizing the loss function yields the final denoised signal.

## 4.2 Experiments and Analysis

### 4.2.1 Qualitative Experiments

Let's take two examples to demonstrate the training process and the effectiveness of the TGD-based denoise algorithm. In a noisy environment, two discrete sequences were sampled from two smooth functions, respectively:

$$X_1(n) = 20 \sin\left(\frac{n}{40}\right) + \frac{n^2}{20000} + \delta(n), \quad n = 0, 1, \dots, 1000 \tag{115}$$

$$X_2(n) = \arctan\left(\frac{n-500}{40}\right) + \frac{n^2}{20000} + \delta(n), \quad n = 0, 1, \dots, 1000 \tag{116}$$

where  $\delta$  is the noise.

Since the value ranges of  $X_1$  and  $X_2$  are different, we add Gaussian noise with mean  $\mu = 0$  and different variances,  $\sigma = 2$  to  $X_1$ , and  $\sigma = 0.2$  to  $X_2$ . The  $\ell_2$  norm is chosen in loss  $L_{1\text{st}}$  and  $L_{2\text{nd}}$ . We eliminate square root calculations and use the sum of squares directly as the loss to speed up the training process. This allows  $L_{\text{offset}}$ ,  $L_{1\text{st}}$  and  $L_{2\text{nd}}$  to be formally consistent. As for loss factors, we choose  $\lambda_{1\text{st}} = 1$ ,  $\lambda_{2\text{nd}} = 10$  and  $\lambda_{\text{offset}} = 0.01$ . In training, we use the Adam optimizer with a learning rate of 0.01. The learnable denoised signal is trained for 100,000 epochs. Using the StepLR strategy, the learning rate decays to 10% of the current whenever the number of training epochs reaches 10,000. One first-order TGD operator and a second-order TGD operator of sizes 51 are used (Figure 27). Due to the effect of padding in the convolution, we actually sampled 1,200 data points and discarded 100 points each before and after, keeping only the remaining part in the middle. The training process is shown in Figure 28 and 29. When the result converges, we get a smooth denoised signal that approximates a  $C^2$  function.

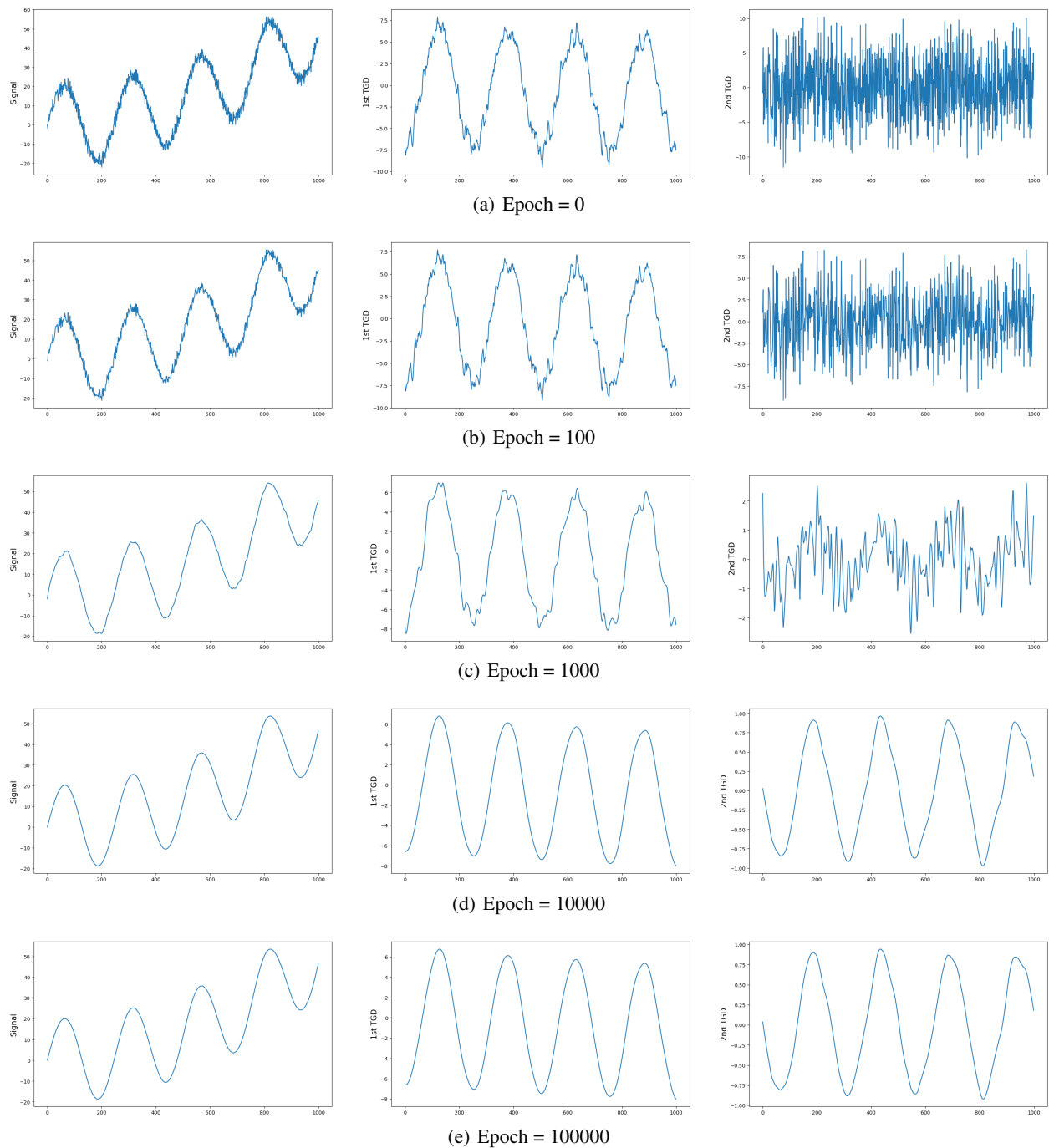


Figure 28: The training process for noisy signal  $X_1$ . The left column shows the current denoised signal. The middle column shows the first-order TGD results of the current denoised signal, and the rightmost column shows the second-order TGD results of the current denoised signal.

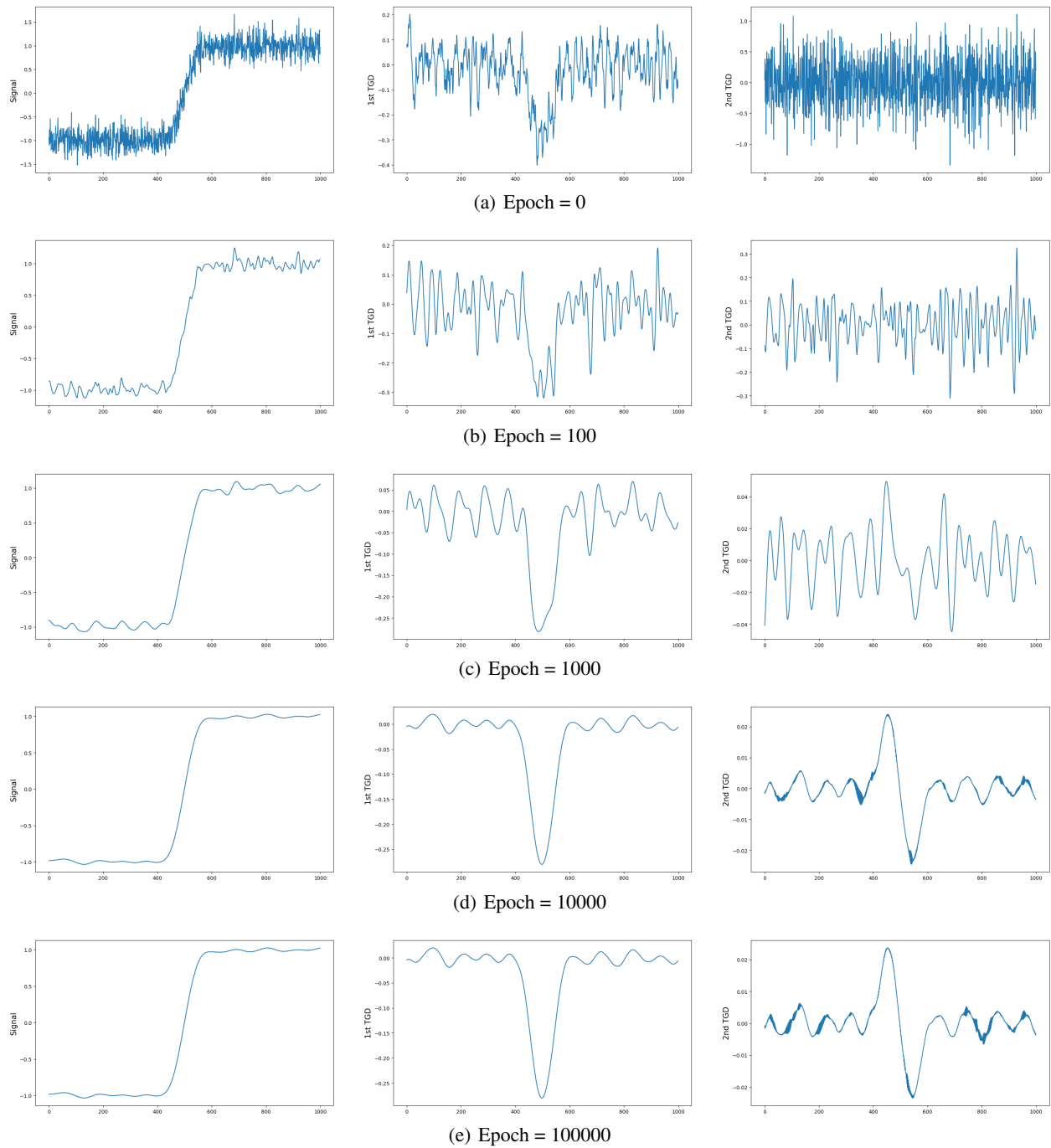


Figure 29: The training process for noisy signal  $X_2$ . The left column shows the current denoised signal. The middle column shows the first-order TGD results of the current denoised signal, and the rightmost column shows the second-order TGD results of the current denoised signal.

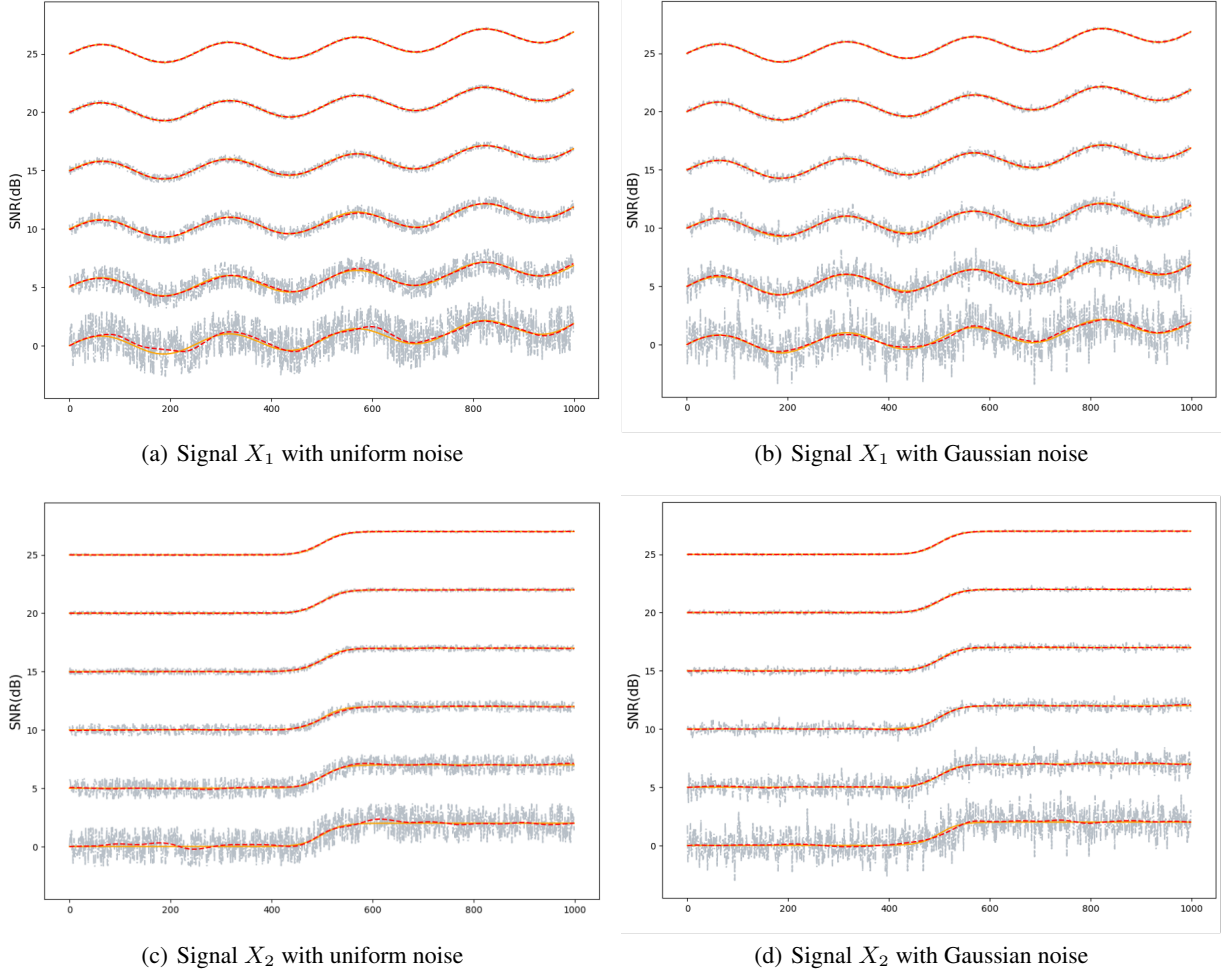


Figure 30: Illustration of the smoothing effect on the noise-corrupted signals with various SNRs. The noise obeys a uniform and normal distribution, respectively. The gray dashed line is the noisy signal, the orange line is the ground truth, and the red dashed line is the denoised approximation.

Further, we investigate the denoising ability of the TGD-based denoise algorithm for different noise levels. The TGD-based denoise algorithm only attaches smoothness assumptions to the original signal and does not rely on prior knowledge of the noise. Here, the signals are contaminated by adding respectively two types of noise, namely uniform and normal, to produce noisy sequences. The amount of the contamination is controlled by the signal-to-noise ratio (SNR) ranging from 0 to 25 dB, which is defined as:

$$\text{SNR}_{\text{db}} = 10 \log_{10} \frac{P(X_{\text{signal}})}{P(X_{\text{noise}})} \quad (117)$$

where the power  $P$  of a signal  $X$  is measure via:

$$P(X) = \frac{1}{N} \sum_{i=1}^N X[i]^2 \quad (118)$$

Figure 30 displays the denoising results, using the same training settings as previously mentioned. The TGD-based algorithm is nonparametric and capable of removing any additive noise. The results indicate that the smooth signal recovery is effective and little distortion occurs in different noise environments, even at an SNR of 0 dB.

### 4.2.2 Quantitative Experiments

Following a qualitative analysis of the effectiveness of the TGD-based denoise algorithm, we then provide a quantitative comparison of the proposed TGD-based algorithm with previous methods. For evaluation metrics, we use mainstream measures, including RMSE, PSNR, and SSIM.

The root-mean-square error (RMSE) is a common metric used to quantify the differences between predicted and true values. RMSE is always non-negative, and a value of 0 would indicate a perfect fit. The RMSE of the original signal with respect to a denoised signal is determined as the square root of the mean squared error:

$$\text{RMSE}(X, Y) = \sqrt{\frac{1}{N} \sum_{i=1}^N (X[i] - Y[i])^2} \quad (119)$$

The peak signal-to-noise ratio (PSNR) is a metric used to measure the level of noise present in a signal. Specifically, it is the ratio of the maximum possible signal power to the power of corrupting noise that may affect its fidelity. Typically, a higher PSNR value indicates less signal distortion from the noise. The PSNR is defined as:

$$\text{PSNR}(X, Y) = 20 \log_{10} \left( \frac{\text{MAX}}{\text{RMSE}(X, Y)} \right) \quad (120)$$

where MAX is the maximum possible value of the signal.

The structural similarity index measure (SSIM) is employed to determine the similarity between two signals [40]. The formula below can be used to compute the SSIM, where  $\mu$  represents the mean value and  $\sigma^2$  is the variance,  $\sigma_{XY}$  is the covariance of the two signals:

$$\text{SSIM}(X, Y) = \frac{(2\mu_X\mu_Y + c_1)(2\sigma_{XY} + c_2)}{(\mu_X^2 + \mu_Y^2 + c_1)(\sigma_X^2 + \sigma_Y^2 + c_2)} \quad (121)$$

where  $c_1 = (k_1L)^2$ ,  $c_2 = (k_2L)^2$ , and  $k_1 = 0.01$ ,  $k_2 = 0.03$  by default.  $L$  is the dynamic range of signal values.

Four classical denoising methods are compared with the proposed TGD-based denoise algorithm, including Gaussian smoothing, wavelet shrinkage, SVD, and TV denoising, respectively. The noisy signals used in experiments are given by Formula (115) and (116), where Gaussian noise is added. The experimental setup used in the proposed algorithm keeps the same as that used in the qualitative analysis. To be consistent with the TGD-based algorithm, we also use size 51 for the Gaussian smoothing kernel. When applying the wavelet shrinkage, the *db8* is adopted to perform the decomposition and the level is 5. The wavelet transform is carried out with *Pywavelets* package [41]. The TV is based on the algorithm for one-dimensional data in Ref. [36]<sup>5</sup>, and the regularization parameter is selected to be 4.47<sup>6</sup>. The SVD is based on the algorithm in Ref. [28]<sup>7</sup>, where the rows of the constructed matrix are 300.

Denoise algorithms are evaluated and compared quantitatively in Table 1. The best results are bolded while the second-best results are underlined. The lowest RMSE and highest PSNR are achieved by the TGD-based denoise algorithm, while also maintaining a satisfactory SSIM score. The results indicate that the TGD-based algorithm performs better than other mainstream methods, resulting in almost no signal distortion between the denoised and original signals.

Table 1: Performance comparison of different denoise methods. We added Gaussian noise with different variance,  $\sigma = 2$  to  $X_1$ , and  $\sigma = 0.2$  to  $X_2$ . The best results are bolded while the second-best results are underlined.

Metric		Gaussian [31]	Wavelet [31]	TV [36]	SVD [28]	TGD (ours)
Signal $X_1$	RMSE	0.3926	0.3568	0.8432	<u>0.2715</u>	<b>0.2480</b>
	PSNR	42.71	43.54	36.07	<u>45.91</u>	<b>46.70</b>
	SSIM	0.9420	0.9743	0.6325	<b>0.9926</b>	<u>0.9900</u>
Signal $X_2$	RMSE	0.0368	0.0285	0.0258	<u>0.0242</u>	<b>0.0228</b>
	PSNR	28.69	30.92	31.76	<u>32.33</u>	<b>32.82</b>
	SSIM	0.9714	0.9907	0.9745	<u>0.9962</u>	<b>0.9963</b>

<sup>5</sup><https://github.com/MrCredulous/1D-MCTV-Denoising>

<sup>6</sup>Suggested in the reference implementation, the regularization parameter  $\lambda = \sqrt{0.5N}/5$ , where  $N$  is the length of signals.

<sup>7</sup><https://github.com/nerdull1/denoise>

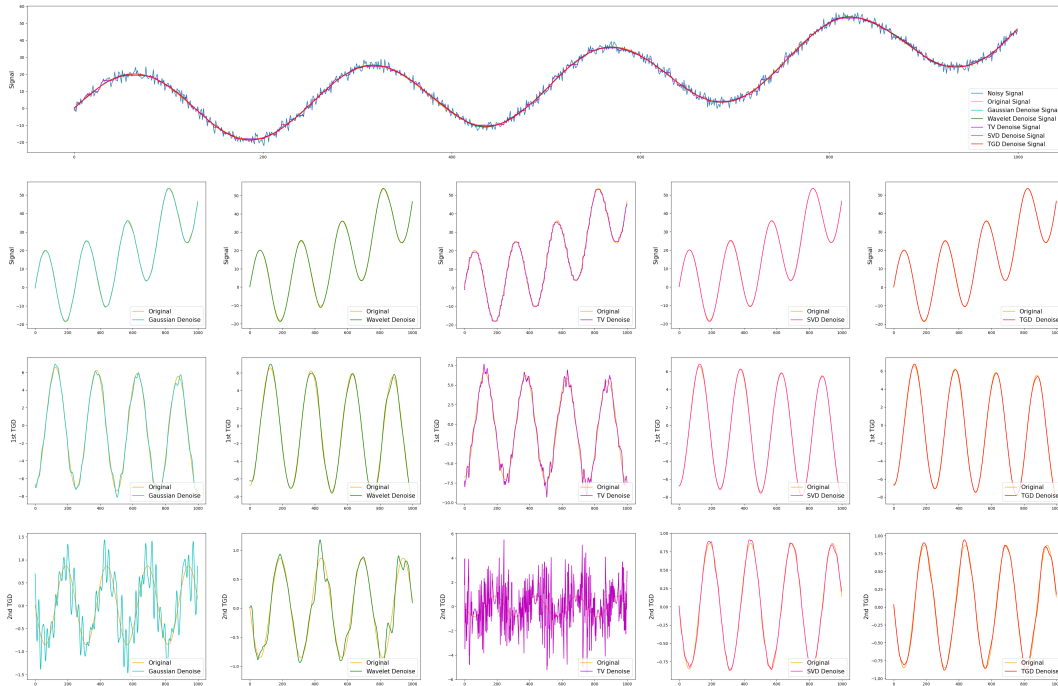


Figure 31: Performance comparison of different denoise methods. We added Gaussian noise with variance  $\sigma = 2$  to  $X_1$ . Denoising methods include: Gaussian convolutional smoothing, wavelet shrinkage, total variation (TV), singular-value decomposition (SVD), and the proposed TGD-based denoise method. The original smooth signal as well as the denoised signal, and their TGD results are compared separately.

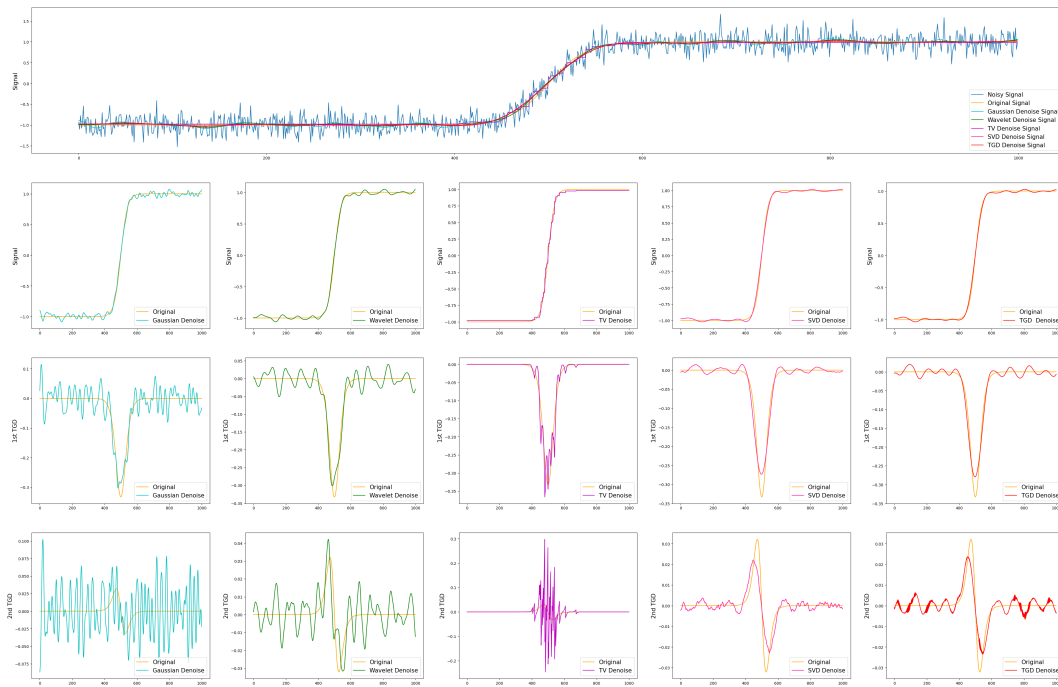


Figure 32: Performance comparison of different denoise methods. We added Gaussian noise with variance  $\sigma = 0.2$  to  $X_2$ . Denoising methods include: Gaussian convolutional smoothing, wavelet shrinkage, total variation (TV), singular-value decomposition (SVD), and the proposed TGD-based denoise method. The original smooth signal as well as the denoised signal, and their TGD results are compared separately.

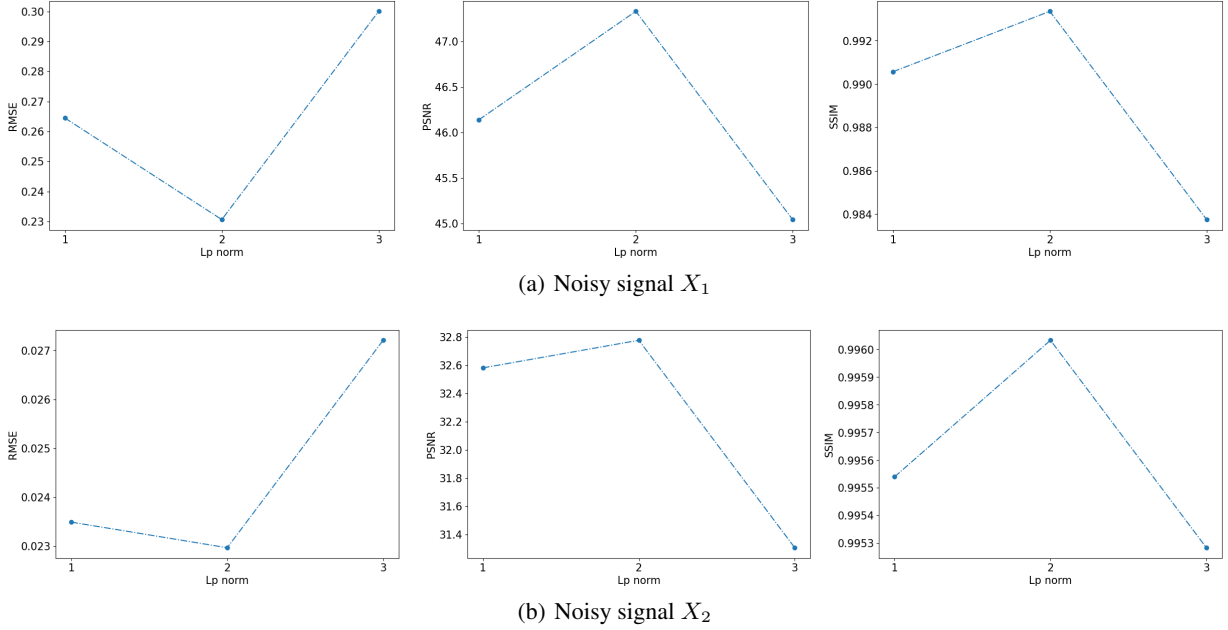


Figure 33: Comparison of the smoothing effect with different  $\ell_p$  norm. Since the loss value may change, we adjusted the loss factor accordingly. The experimental results suggest that the  $\ell_2$  norm would be a good choice.

Figure 31 and 32 further visualize the comparison between the output denoised signals and original signals. The continuity of the denoised signals is achieved by all methods, but the TV denoise algorithm fails to maintain the continuity of the first-order TGD. This aligns with theoretical analysis showing that a continuous function does not necessarily need to be derivable/smooth. Due to the exchangeability of the convolution, calculating the TGD after Gaussian smoothing of the noisy signal is equivalent to Gaussian smoothing of the TGD for the noisy signal. As the SNR of the derivative is lower than that of the noisy signal, Gaussian smoothing does not guarantee continuity in the TGD, particularly second-order TGD, causing the denoised signal to not approximate a  $C^2$  function. The continuity of the first- and second-order TGDs is better with wavelet shrinkage denoising than with Gaussian, but still lagged behind the proposed TGD-based algorithm. The closest performance to the proposed algorithm is the SVD denoising method, where they both obtain a signal that approximates a  $C^2$  function. However, the TGD-based algorithm is optimal regarding quantitative metrics.

### 4.2.3 Ablation Experiments

In the ablation experiments, the noisy signals are obtained from Formula (115) and (116), where Gaussian noise with  $\sigma = 2$  is added to  $X_1$ , and  $\sigma = 0.2$  to  $X_2$ . First, we compare the smoothing effects of different  $\ell_p$  norms in the loss function, including  $p = 1, 2$ , and 3. The experimental setup employed in the TGD-based algorithm remains consistent with that used in the qualitative analysis. It is worth pointing out that, the difference in the  $\ell_p$  norms results in variations in the loss magnitude, hence the need to adjust the loss factor for each  $p$  choice. The outcomes of RMSE, PSNR, and SSIM metrics are depicted in Figure 33. Based on the quantitative results, the  $\ell_2$  norm seems to be a better choice.

Next, we do the ablation analysis for loss factors. Figure 34 illustrates the denoising effect of various loss factors applied to noisy signal  $X_1$ . The first three rows compare the degree of continuity constraints. For  $\lambda_{1st} > 0$  and  $\lambda_{2nd} = 0$ , the first-order TGD of the output signal is continuous, but the second-order TGD fluctuates drastically. Conversely, for  $\lambda_{2nd} > 0$ , the output signals' second-order TGDs are continuous, and resulting denoised signals resemble a  $C^2$  function. In such cases, it is preferable to apply continuity constraints to both first- and second-order TGDs, rather than just the latter. The final two lines demonstrate the impact of varying  $\lambda_{offset}$ . For  $\lambda_{offset} = 0$ , no correlation is needed between the denoised signal and the noisy signal, resulting in severe distortion. At this stage, the optimal solution is for both first- and second-order TGD to be constant values, leading to a constant or linear denoised signal. When  $\lambda_{offset}$  is relatively large, the denoised signal fits the noisy signal as closely as possible, making it hard to maintain derivative continuity in a high-noise setting. Hence,  $\lambda_{offset}$  should be decreased accordingly when the SNR is low.

Lastly, we examine the influence of TGD operator size on smoothing performance. When the operator size is relatively small, the difference computation becomes highly sensitive to noise. The corresponding difference sequence is severely

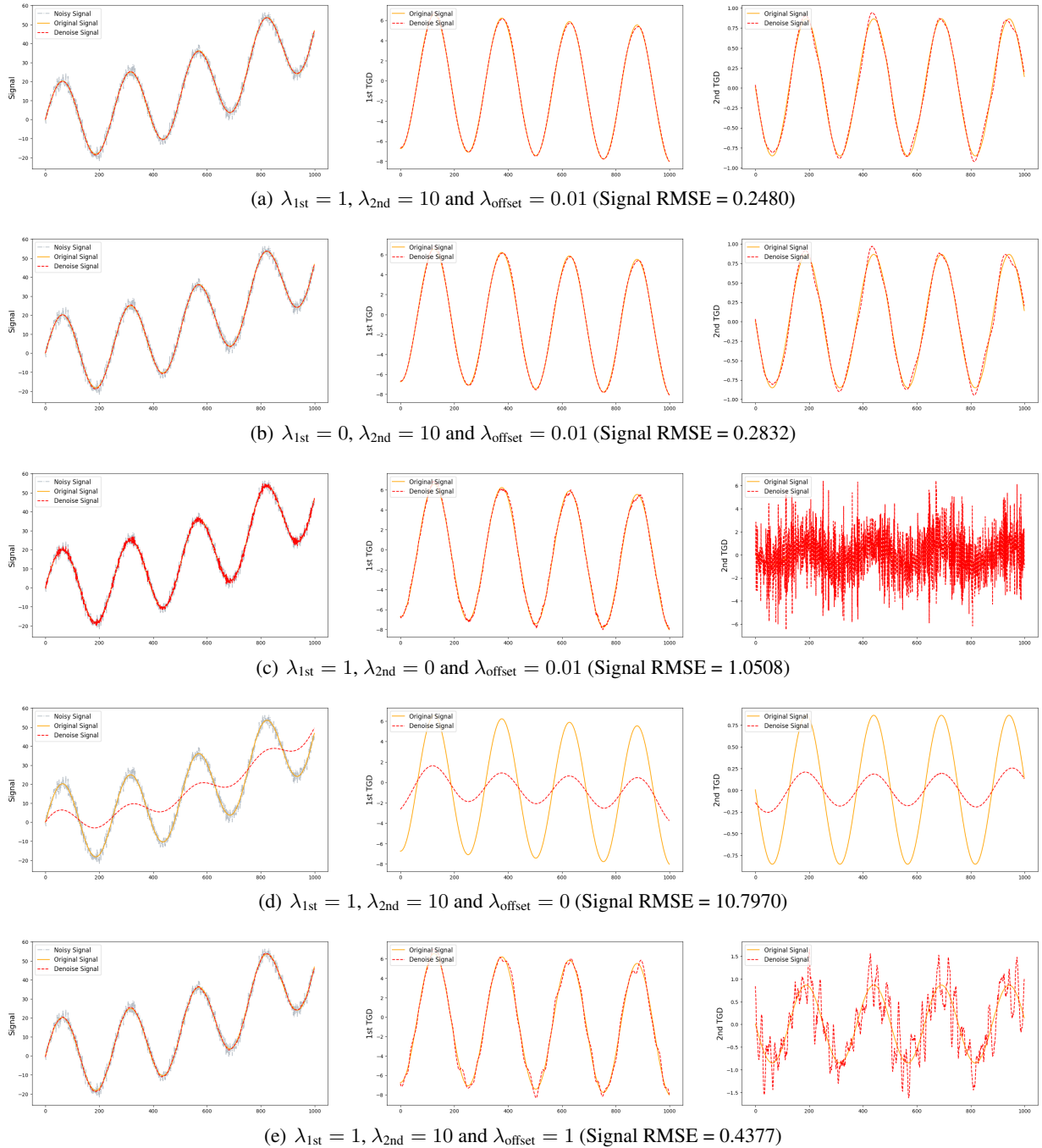


Figure 34: Comparison of the smoothing effect with different loss factors. The results show that simultaneous consideration of the complete loss is beneficial for denoising.

distorted, resulting in poor smoothing. Moreover, increasing the operator size is not always feasible since it tends to lead to a global operation. This, in turn, can distort the signal if it results in excessive smoothness. Additionally, long padding causes spurious patterns of variation at both ends of the signal, which is undesirable. These align with the experimental results depicted in Figure 35, where the TGD-based denoise algorithm's performance initially improves as the operator size increases but then deteriorates. Optimal overall performance is achieved when the operator size is approximately 51. If the signal sequence length is short, the TGD convolution kernel size should be correspondingly reduced.

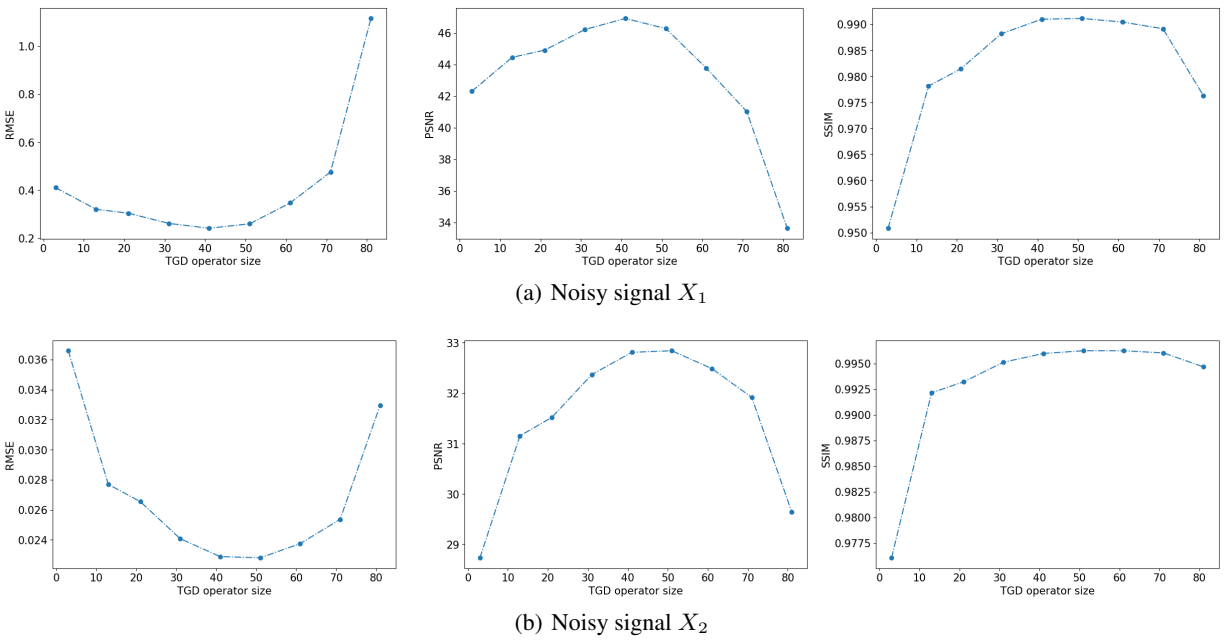


Figure 35: Comparison of the smoothing effect with various TGD operator sizes, from 3 to 81. It can be seen that the denoising effect gets better and then worse as the operator size increases, and the smoothing effect is satisfactory when the operator size is around 51.

## 5 The Application of TGD in Computer Vision

Theoretically, edge refers to places in the image where there appears to be a jump in brightness value. These transitions correspond to peaks in the first-order derivative or zero-crossings in the second-order derivative of intensity [42, 43, 20]. Thus, determining an image's first- or second-order derivative and identifying the precise location of extremas or zero-crossings constitute the fundamental basis for image edge detection. The prevalent techniques for edge detection fall into two categories [44]: gradient-based and Laplacian-based approaches, which correspond to the computation of an image's first- and second-order derivatives, respectively.

As previously mentioned in Section 2.3, LoT and LoG operators differ in the proximity of their zero-crossings, which are adjacent to the center in LoT and in the vicinity of the center in LoG (see Figure 15). A similar behavior can be observed in first-order difference operators, extremas are adjacent to the center in the first-order TGD operator, while in the vicinity of the center in the first-order Gaussian derivative operator (see Figure 36). In a discrete setting, the size of first- and second-order difference convolution kernels larger than  $13 \times 13$  highlights this distinction.

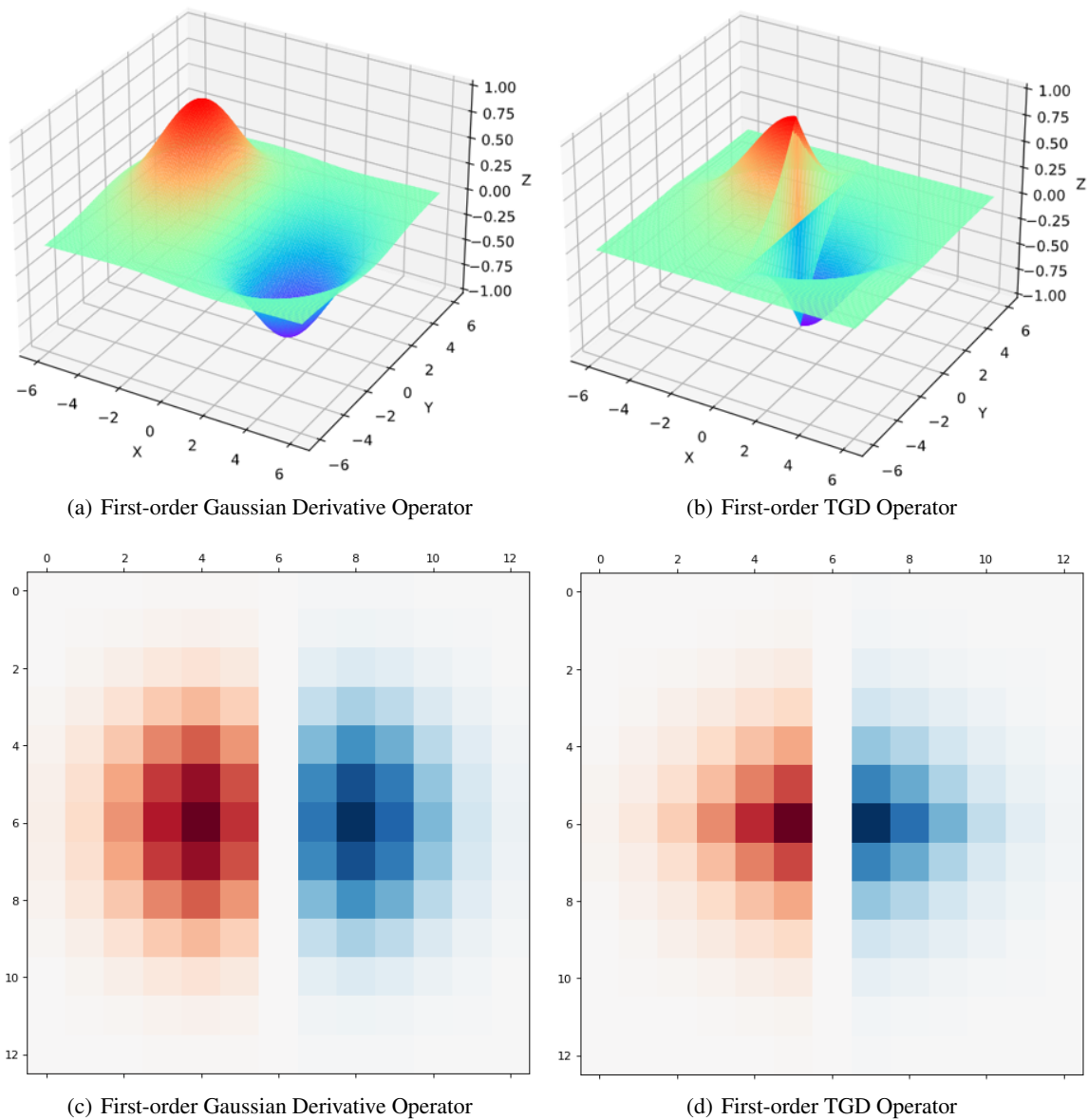


Figure 36: The first-order Gaussian derivative operator and TGD operator, whose kernel function is Gaussian.

**Algorithm 1** First-order TGD-based Edge Detection Algorithm

**Input:** Gray image  $I$ , first-order discrete TGD operators in four directions  $\widehat{T}_{0^\circ}, \widehat{T}_{45^\circ}, \widehat{T}_{90^\circ}, \widehat{T}_{135^\circ}$ , high threshold  $highThr$  and low threshold  $lowThr$  for Double-threshold Selection.

**Output:** Edge position  $E$  and edge orientation  $D$

- 1:  $dx = I * \widehat{T}_{0^\circ}$
- 2:  $d_{45^\circ} = I * \widehat{T}_{45^\circ}$
- 3:  $dy = I * \widehat{T}_{90^\circ}$
- 4:  $d_{135^\circ} = I * \widehat{T}_{135^\circ}$
- 5:  $Grad = (\sqrt{dx^2 + dy^2} + \sqrt{d_{45^\circ}^2 + d_{135^\circ}^2}) / 2$
- 6:  $\Theta = \arctan(dy/dx)$
- 7:  $NMS = \text{Non-Maximum Suppression}(Grad, \Theta)$
- 8:  $E = \text{Double-Threshold Selection}(NMS, lowThr, highThr)$
- 9:  $D = \text{Matrix Element Multiplication}(E, \Theta)$
- 10: **return**  $E, D$

In this section, we introduce TGD into image gradient computation and propose first- and second-order TGD-based edge detection algorithms, with reference to classical approaches. We demonstrate that the drift phenomena in edge location is associated with the deviation of the local extrema (in first-order) and zero-crossing (in second-order) from their center. Visual inspections reveal that the main energy (two peaks) of the first-order Gaussian derivative operator expands alongside kernel size growth, violating the Monotonic Constraint, thereby inducing detection drift in localizing edges, particularly noticeable for large kernel sizes ( $\geq 13 \times 13$ ). This drift becomes more pronounced as the kernel size increases. In comparison, the main energy (two peaks) of the first-order TGD operator adheres to the Monotonic Constraint and is invariably centered within the convolution kernel, ensuring precise edge localization even at large kernel sizes. This analysis holds true for the zero-crossings in the LoG and LoT operators. Additionally, we expand the TGD-based algorithm to perform 3D spatio-temporal edge detection in image sequences or videos.

### 5.1 First-order TGD-based Image Edge Detection

In computer vision, the classic edge detection method is proposed by John Canny [45], which consists of four stages in OpenCV<sup>8</sup>: Noise reduction via Gaussian smoothing, Finding the intensity gradient of the image via Sobel operators, Non-maximum Suppression, and Hysteresis Thresholding (or called Double-Threshold Selection). As the first-order TGD operators are naturally robust to noise in the difference calculation, we replace the first two stages of the Canny algorithm with a single TGD convolution stage to form the three-stage first-order TGD-based edge detection algorithm. Figure 37 shows the whole algorithm flowchart, and the pseudo-code is presented in Algorithm 1.

In the subsequent experiments, we utilize the 2D first-order discrete TGD operators obtained by the rotational construction method (Sec.2.3). The kernel function employs the exponential function (Sec.1.3.2) and the cosine function is used for the rotation weights. For a fair comparison, we maintain a consistent size for the convolution kernel in both the Canny and TGD-based edge detection algorithms, while leaving the other aspects of the algorithms unaltered.

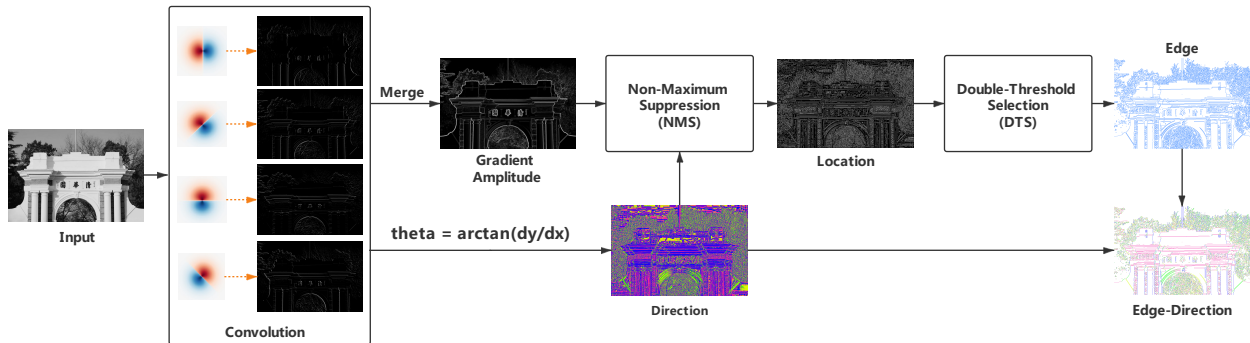
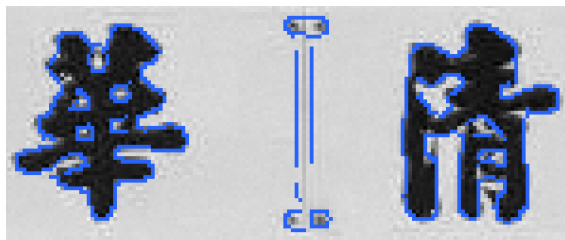


Figure 37: Flowchart of edge detection algorithm based on first-order TGD.

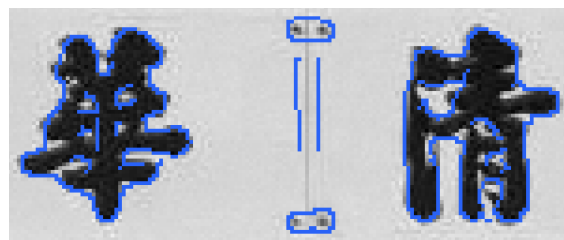
<sup>8</sup>[https://docs.opencv.org/master/d7/de1/tutorial\\_js\\_canny.html](https://docs.opencv.org/master/d7/de1/tutorial_js_canny.html)



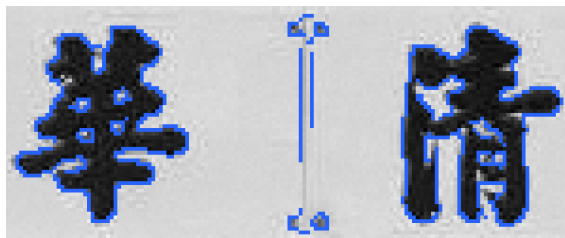
(a) Nature Image



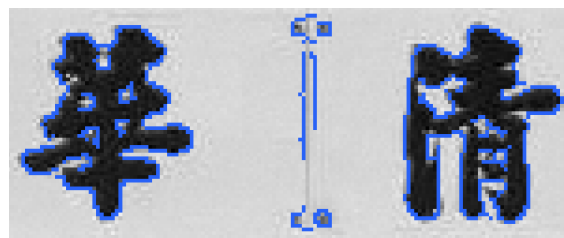
(b) Canny  $13 \times 13$



(c) Canny  $17 \times 17$

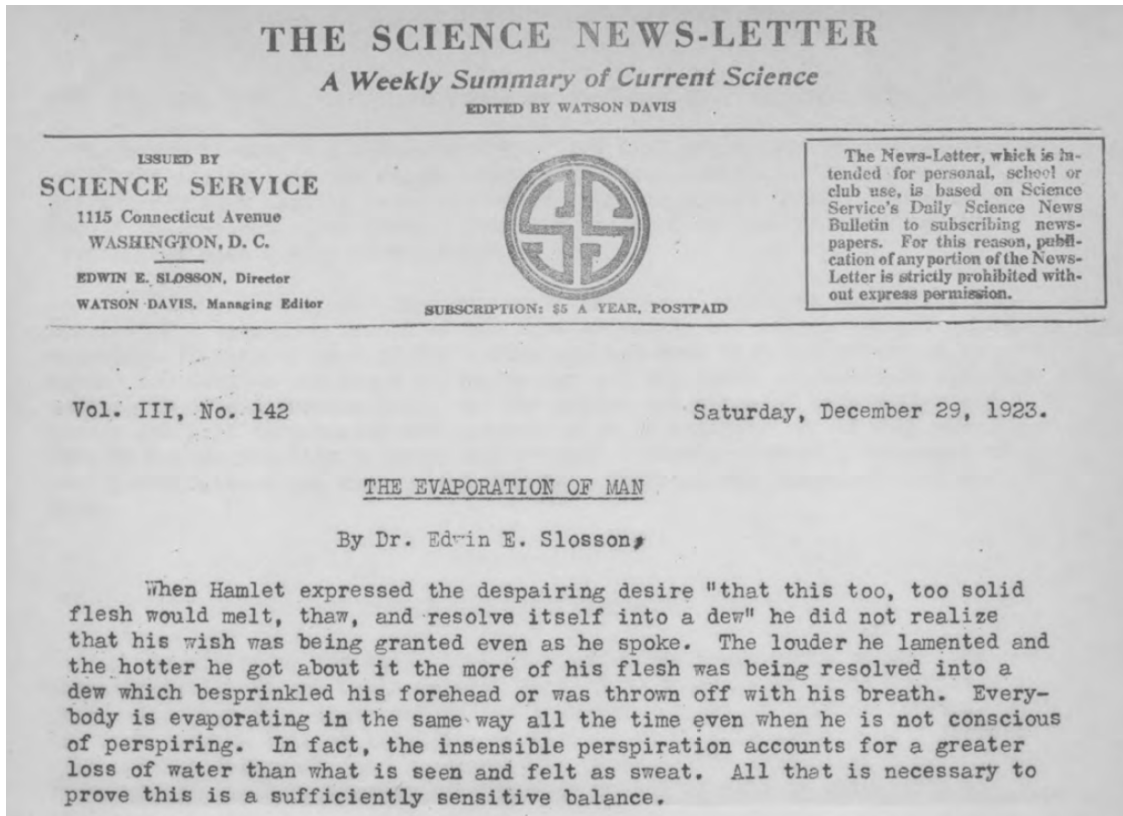


(d) TGD  $13 \times 13$



(e) TGD  $17 \times 17$

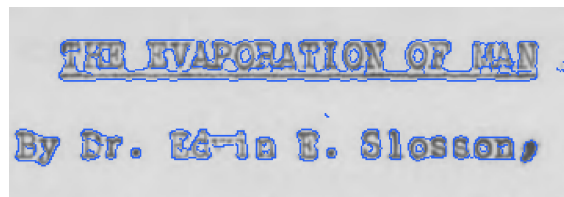
Figure 38: Edge detection results: (a) original nature image; (b - e) detected edges by Canny and TGD algorithms, in which the edges detected by Canny algorithm have one-pixel drift at the kernel size  $13 \times 13$ , and two pixels drift at the kernel size  $17 \times 17$ .



(a) Texture Image



(b) Canny  $13 \times 13$



(c) Canny  $17 \times 17$



(d) TGD  $13 \times 13$



(e) TGD  $17 \times 17$

Figure 39: Edge detection results: (a) original texture image; (b - e) detected edges by Canny and TGD algorithms, in which the edges detected by Canny algorithm have one-pixel drift at the kernel size  $13 \times 13$ , and two pixels drift at the kernel size  $17 \times 17$ .



Figure 40: Edge orientation map obtained by  $17 \times 17$  first-order TGD operators in four directions, which are indicated in color arrows.

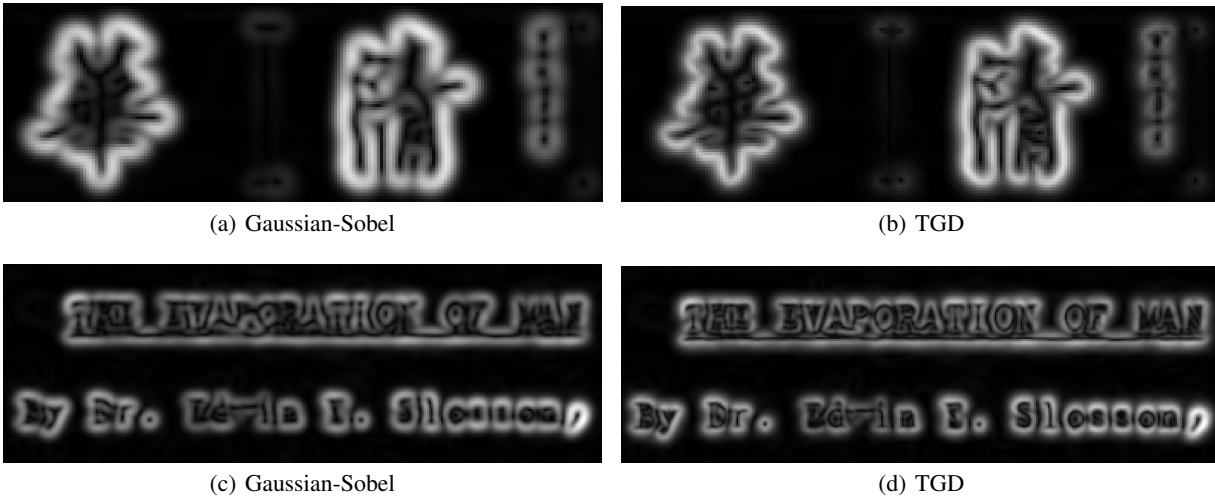


Figure 41: Comparison of gradient magnitudes in detail: (a,c) plot of gradient magnitude computed by  $17 \times 17$  first-order Gaussian-Sobel derivative operators; (b,d) plot of gradient magnitude computed by  $17 \times 17$  first-order TGD operators. The gradient magnitude values are positive and normalized, and the whiter the color in the visualization represents the larger the value.

In the theoretical analysis (Sec.1.2), we point out that Gaussian first-order derivative fails to satisfy *Unbiasedness* constrains, and produces drifting localization of detected edges with increasing kernel size. This is consistent with the experimental results shown in Figure 38 and 39, in which the local details of edge localization detected by Canny operator have drift with one to two pixels. In contrast, the first-order TGD operators, employing the same kernel size as that of Canny, enable accurate localization with good noise reduction performance.

The edge location map is derived from the gradient amplitude calculations produced by the first-order derivatives. Figure 41 provides a comparison of the gradient amplitudes obtained through first-order Gaussian derivative operators in Canny and first-order TGD operators. Notably, there is significant outward expansion of the local extremes in the gradient amplitude map calculated by the first-order Gaussian derivative operators. This expansion is detrimental to accurate recognition of Chinese characters (Figure 41.a) and English letters (Figure 41.c). In contrast, the results yielded via the first-order TGD operators are reliable, and the local gradient extremes are concentrated toward the edges and precisely located. Such reliable and accurate gradient information is crucial for downstream tasks, as it can serve as an essential image feature beyond edge detection.

## 5.2 Second-order TGD-based Image Edge Detection

The LoG operator, also known as the Laplacian of Gaussian (Figure 15 Left), provides a two-dimensional isotropic measure of the second-order derivative of an image. This operator brings highlighted regions of rapid intensity changes, making it a popular edge detection tool. The LoG-based edge detection method involves two steps: firstly, the image is convolved with the LoG operator and filtered with a threshold, then the zero-crossings are scanned in the results of convolution [46, 22, 47].

The edge detection algorithm based on the LoT operator follows the traditional two-stage LoG-based method, where the LoG operator is replaced by the directional LoT operator (Sec.2.3, Figure 24). Since the edge orientation is orthogonal to the gradient direction, which has the largest response, the edge orientation can be determined by comparing the response of multiple second-order directional TGD operators. However, due to the isotropism of LoG, the edge orientation cannot be obtained as in the gradient-based method (Figure 40). Algorithm 2 presents the pseudo-code

**Algorithm 2** Second-order TGD-based Edge Detection Algorithm

**Input:** Gray image  $I$ , second-order discrete TGD operators in four directions  $\widehat{R}_{0'}$ ,  $\widehat{R}_{45'}$ ,  $\widehat{R}_{90'}$ ,  $\widehat{R}_{135'}$ , LoT operator  $\widehat{R}_{\text{Laplacian}}$ , Laplacian threshold  $LoTThr$ .

**Output:** Edge position  $E$  and edge orientation  $D$

- 1:  $Grad_L = I * \widehat{R}_{\text{Laplacian}}$
- 2:  $Grad_L[abs(Grad_L) < LoTThr] = 0$
- 3:  $d_{0'} = I * \widehat{R}_{0'}$
- 4:  $d_{45'} = I * \widehat{R}_{45'}$
- 5:  $d_{90'} = I * \widehat{R}_{90'}$
- 6:  $d_{135'} = I * \widehat{R}_{135'}$
- 7:  $\Theta(x, y) = \text{argmax}(d_{0'}, d_{45'}, d_{90'}, d_{135'})$
- 8:  $E = \text{Find Zero-Crossing}(Grad_L)$
- 9:  $D = \text{Matrix Element Multiplication}(E, \Theta)$
- 10: **return**  $E, D$

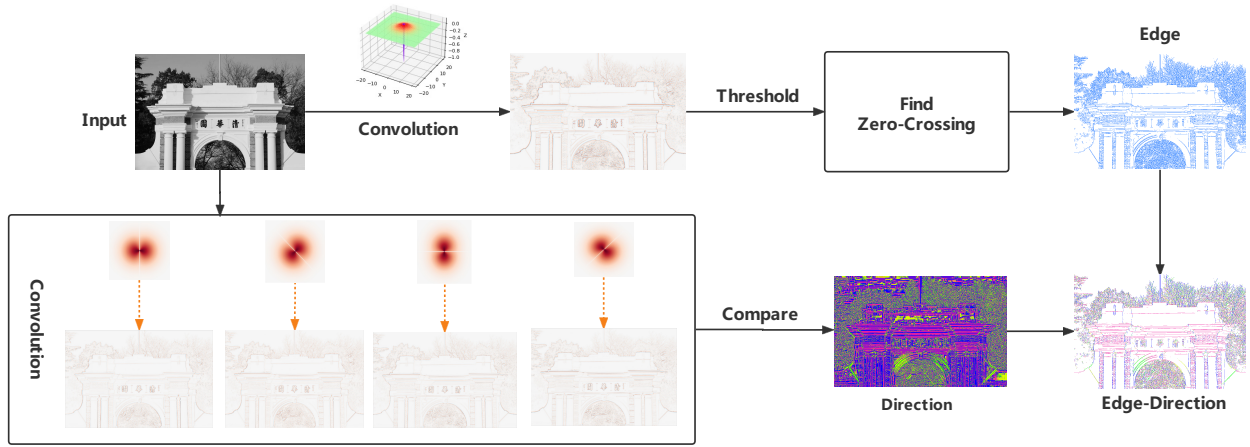


Figure 42: Flowchart of edge detection algorithm based on second-order TGD.

of the LoT-based edge detection algorithm, and Figure 42 shows the whole algorithm flowchart. In the subsequent experiments, the Gaussian kernel function is used to construct the LoT operator.

Figure 43 presents the detection results of the  $13 \times 13$  and  $17 \times 17$  LoG and LoT for a natural image with localized edge details. Obviously, the LoG operator exhibits localization drift, whereas the LoT operator produces accurate localization for very fine details.

The LoT operator's advantages are more pronounced in text. The detection details illustrate that the edges detected by the LoG operator severely shift due to significant loss of high-frequency signals, such as the punctuation mark “.” and the horizontal of the letter “T”. Since only the center is negative, the LoT operator is not sensitive to the kernel size during convolution. For images with black text on a white background, edges are either black-and-white adjacent white pixels or black pixels. The gradient-based edge detection algorithm typically detects the text outline (white pixels) as the edges (Figure 39.e), while the LoT-based edge detection algorithm locates the text itself (black pixels) as the edges (Figure 44.d). Therefore, the LoT operator is ideal for detecting text edges.

Figure 45 illustrates the edge orientation obtained through four-directional orthogonal constructed second-order TGD operators. The detected orientation is the same as the physical edge orientation. Additionally, we observe that both the rotational and orthogonal constructed second-order TGD operators produce similar results.

Figure 46 shows the convolution results of the  $17 \times 17$  LoG and LoT that have been normalized (divided by the maximum positive value), where positive values are red and negative values are blue. The image edges are located at the zero-crossings (white) between red and blue regions. The results indicate that the convolution energy obtained from the LoT operator is precisely concentrated at the edges. In contrast, the convolution energy obtained from the LoG operator spreads away from the edges, causing edge localization drift. This disparity stems fundamentally from the different convolution kernels used. The Monotonic Constraint, which states that only the center weights should be negative

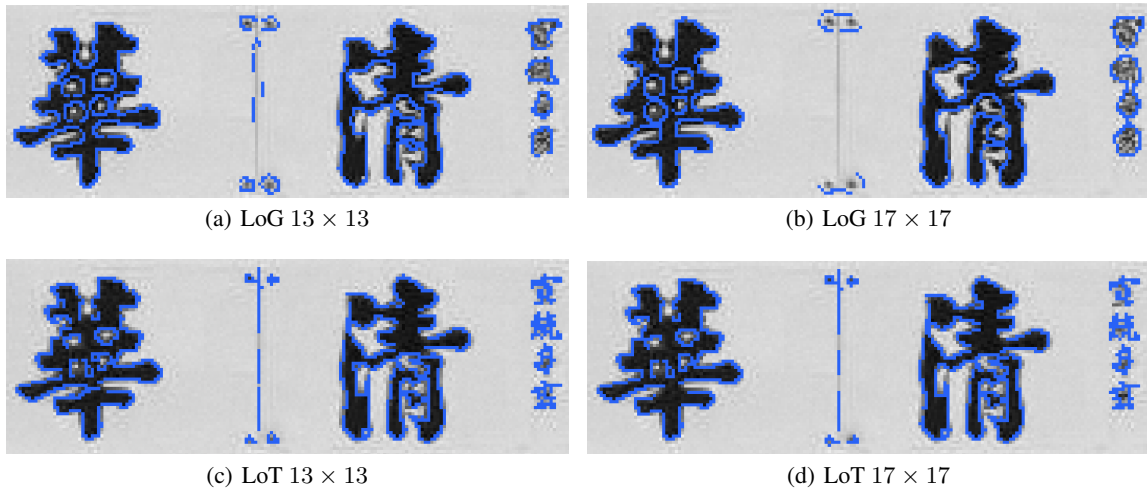


Figure 43: Edge detection: the local detection details of the LoG and LoT operators. The original natural image is shown in Figure 38.

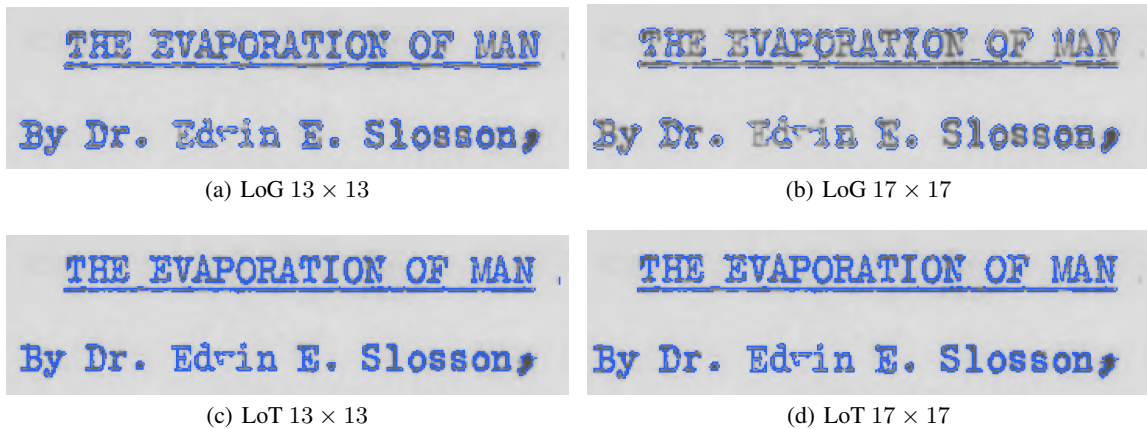


Figure 44: Edge detection results: (a-d) the local detection details of the LoG and LoT operators. The original texture image is shown in Figure 39.



Figure 45: Edge orientation map obtained by  $17 \times 17$  second-order TGD operators in four directions, which are indicated in color arrows.

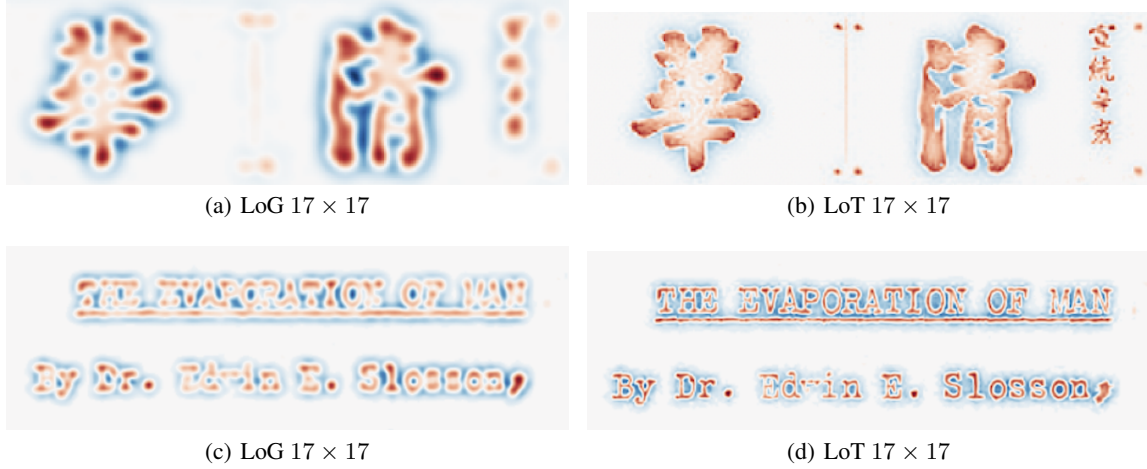


Figure 46: Comparison of convolution results: (a,c) convolution results of  $17 \times 17$  LoG operator; (b,d) convolution results of  $17 \times 17$  LoT operator.

(Figure 15), ensures the accuracy of edge localization in the LoT operator. Conversely, the LoG operator contains a large number of negative values near the center of the convolution kernel, which triggers the edge localization drift observed in previous studies [48, 49].

### 5.3 TGD-based 3D Edge Detection

The definition of an edge can be expanded from 2D images to 3D image sequences like videos, where there is a jump change in brightness value, corresponding to local extrema points of the gradient. Due to TGD's ability to compute gradients for 3D discrete sequences, the TGD-based edge detection method can be extended naturally to the 3D case. Here, we introduce the TGD-based 3D edge detection algorithm, which is presented in Figure 47, and its pseudo-code is described in Algorithm 3.

---

#### Algorithm 3 TGD-based 3D Edge Detection Algorithm

---

**Input:** Gray image sequence  $I$ , 3D first-order discrete TGD operators in  $x$ - and  $y$ -directions  $\hat{T}_x, \hat{T}_y$ , 1D first- and second-order discrete TGD operator in  $t$ -direction  $\hat{T}_t, \hat{R}_t$ , motion threshold  $Thr_1$  and  $Thr_2$ , high and low threshold  $highThr, lowThr$  for Double-threshold Selection.

**Output:** Motion edge locations  $M$ , Static edge locations  $S$ , and merge visualization  $V$ .

- 1:  $dx = I * \hat{T}_x$
  - 2:  $dy = I * \hat{T}_y$
  - 3:  $dt = I * \hat{T}_t$
  - 4:  $d^2t = I * \hat{R}_t$
  - 5:  $Grad = \sqrt{dx^2 + dy^2}$
  - 6:  $\Theta_{xy} = \arctan(dy/dx)$
  - 7:  $NMS = \text{Non-Maximum Suppression}(Grad, \Theta_{xy})$
  - 8:  $S = \text{Double-Threshold Selection}(NMS, lowThr, highThr)$
  - 9:  $M = |dt| > Thr_1 \text{ or } |d^2t| > Thr_2$
  - 10:  $V = \text{HSV Visualization}(\Theta_{xy}, M, S)$
  - 11: **return**  $M, S, V$
- 

Our algorithm comprises three parts. The first part detects local extrema points of the gradient on the  $xy$  plane, using the first-order TGD-based image edge detection algorithm. However, our approach incorporates 3D TGD operators to obtain partial TGD in the  $x$ - and  $y$ -directions, enabling the algorithm to capture background details shielded by moving objects. We refer to this type of edge as *Static edge*, where a jump in brightness value occurs in the spatial domain. The second part is motion detection, whereby pixels exhibiting 1D first- or second-order TGD larger than

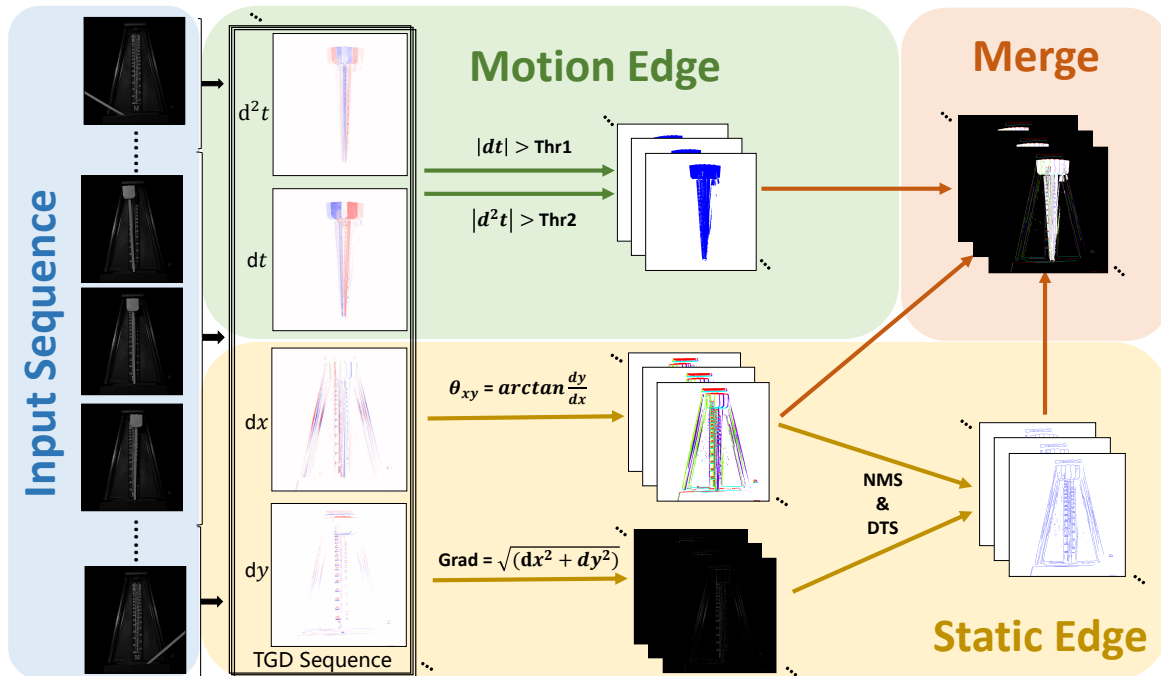


Figure 47: Flowchart of TGD-based 3D edge detection algorithm.

the corresponding threshold along the  $t$ -axis are marked out<sup>9</sup>. Although these pixels differ from ordinary *static edges*, a substantial brightness change along the  $t$ -axis implies the occurrence of motion. We refer to these sensitive pixels marked out in this part as *Motion edge*, where sharp changes occur in pixel values over time. It is worth noting that the central weight value of the first-order TGD operator is 0, indicating that it is only aware of previous and subsequent states but not the current state. Thus, we combine it with second-order TGD to complete motion detection. Additionally, we use the HSV space to visualize edge directions, which we combine with gradient directions.

In our experiments, we adopt the TGD operators acquired using the orthogonal construction method (Sec.2.4). The 3D TGD operators in the  $x$ - and  $y$ -directions employ the Gaussian kernel function (Sec.1.3.3), while the 1D TGD operators in the  $t$ -direction use the linear kernel function (Sec.1.3.1). Their kernel sizes are  $15 \times 15 \times 15$  and  $1 \times 1 \times 15$ , respectively. Additionally, we scale the time dimension by either copying or skipping frames.

Figure 48 shows the result of TGD-based 3D edge detection. In the video we recorded, a pendulum constantly swings back and forth in the foreground with a complex background. Since the pendulum moves quickly, we slow down the motion of the swinging pendulum by copying frames while maintaining a frame sequence length of 15 that is used for calculating TGD. Here, the number of effective frames is 5 since we create 3 copies for each frame. The positions of the pendulum at five different moments and the correct static edge locations and orientations are all well obtained. Though discontinuity of the motion edge is observed, the main reason for this phenomenon is too small a difference in brightness between the moving object and the background.

We further analyze some special elements of the detected edges in Figure 48. Shadows may be marked as motion edges due to a variation in brightness over time. Figure 49.a illustrates the motion edges generated by the shadow. As observed in the local screenshots of input frames (second and third columns), the movement of the pendulum produces a shadow on the background. This results in a variation of the brightness values at that particular spatial location over time. Specifically, the pendulum's movement produces a specific response on the time-direction TGD with the background transitioning from dim to light, then back to dim. Additionally, the appearance and disappearance of the shadow produce a modification in the background color, transitioning from light to dim and then back to light. As a result, the pendulum and the shadow engender opposing positive and negative responses, which are represented as red and blue in the TGD response. Figure 49.b displays the static edges of the moving object and the hidden object. The TGD responses in the  $x$ - and  $y$ -directions of the input frame sequence might be identical to the weighted summation of

<sup>9</sup>Motion detection needs to operate at the pixel level. 3D TGD operators, with the effect of spatial smoothing, may result in wrongly identifying static pixels as motion pixels. Hence, we suggest using 1D TGD operators.

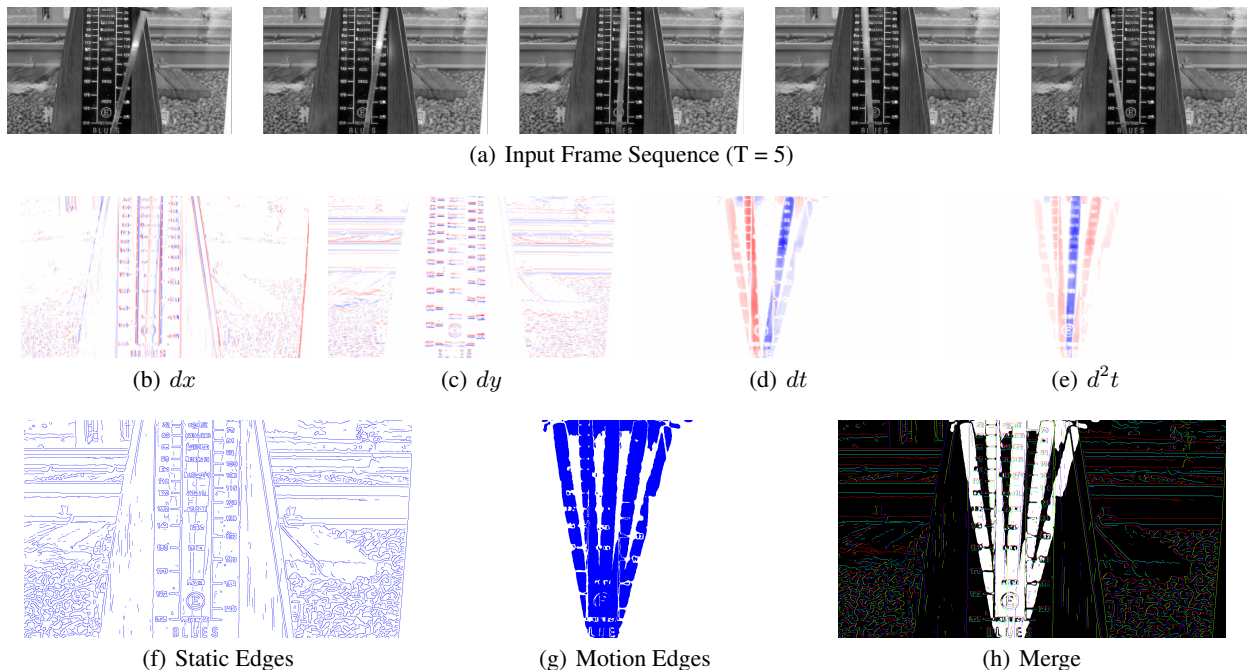


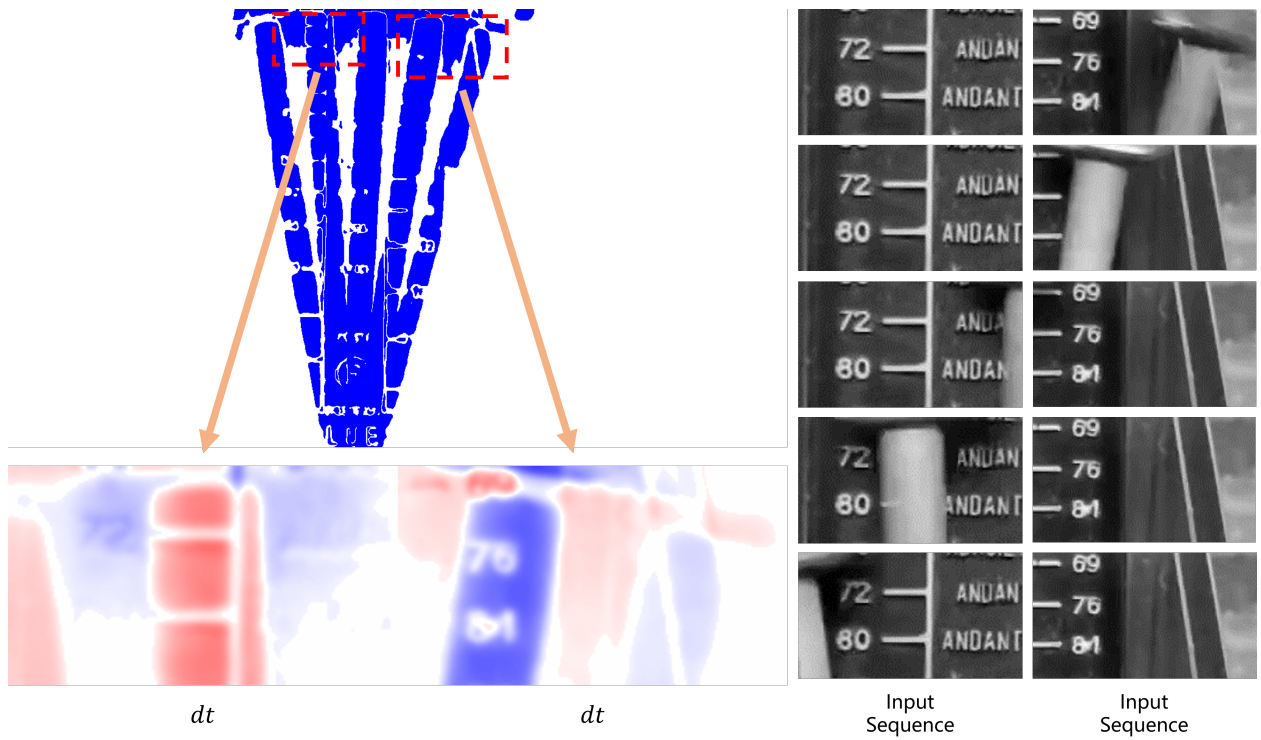
Figure 48: 3D Edge detection results: (a) Input frame sequence, where T represents the number of effective frames; (b-e) first- and second-order TGD; (f) static edges; (g) motion edges; (h) merged visualization via HSV space.

the TGD responses of the individual frames. For moving objects that exist at different locations in different frames, their TGD responses at those locations result in a weak superposition effect on the final outcome. The further away from the intermediate frames, the weaker the superposition effect becomes. Likewise, for the background that is occluded and then reappears, its TGD responses are superimposed on the final response. This exposes itself in the identification of static edges (The letter “E”). It is conceivable that the TGD responses are accommodating to the occluded background and might be helpful in the future for detecting motion-obscured video objects and segmenting activities.

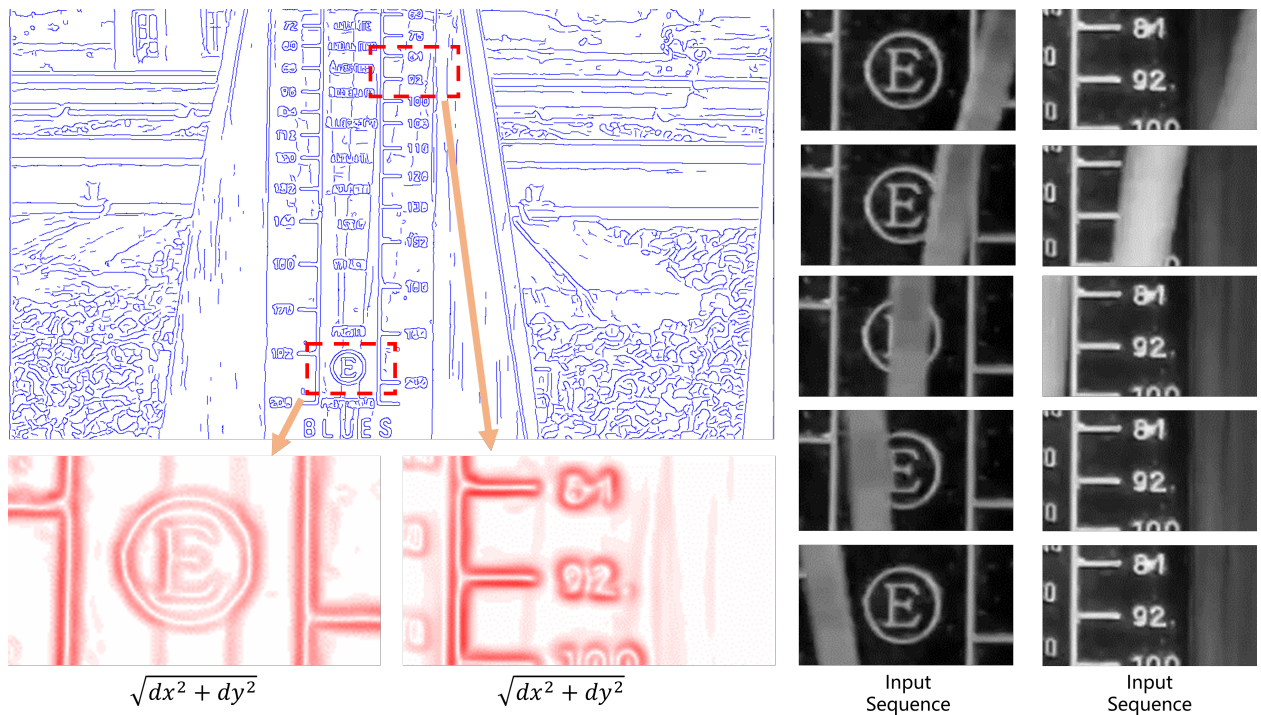
Let us analyze the algorithm under more ideal conditions. Figure 50 shows the 3D TGD-based edge detection of a swinging pendulum in front of a plain black background. Surface treatment is applied to the pendulum in order to avoid specular reflection and maintain consistent surface brightness. Additionally, we avoid the interference of shadows. This setup allows for a more idealistic analysis of our algorithm. By copying each frame 15, 5, and 3 times, we scale the number of effective frames to 1, 3, and 5, respectively. Note that when only one effective frame is available, the input sequence is constant, then TGD-based 3D edge detection is equivalent to the corresponding image edge detection on the center frame (Figure 50.h). With moving objects in the input frame sequence, the TGD-based algorithm detects the moving parts effectively, generating the same static edge results as those in the constant frame sequence. As the number of effective frames increases, we could detect more motion edges, and some static edges that are not present in the intermediate frame could be identified. This is because moving objects in different positions in each frame cause physical edges to overlap in the final results, producing identified static edges. Occluded physical edges that are partially exposed may also overlap in the final results, producing detected static edges.

Moreover, TGD results along the time axis can provide a deeper understanding of motion, beyond detecting the brightness fluctuation at a particular location to ascertain if a moving object is passing through. Here we assume that the moving object is brighter than the background. As shown in Figure 51, we select three cases, with each comprising five effective frames. The orange arrows indicate the pendulum’s moving direction. For the second-order TGD, moving objects within the intermediate frame generate negative responses (blue), while moving objects in other frames generate positive responses (red). In contrast, the first-order TGD detects moving objects in previous frames, producing negative responses (blue), and moving objects in forthcoming frames, producing positive responses (red). Further the frames away from the intermediate frame, the more the intensity of the response reduces<sup>10</sup>. Combining this information would further enable the inference of motion direction, which is crucial in various downstream applications.

<sup>10</sup>This is caused by the Monotonic Constraint of TGD.



(a) Motion edges of shadows



(b) Static edges of moving objects and obscured objects

Figure 49: Special case description of the detected edge.

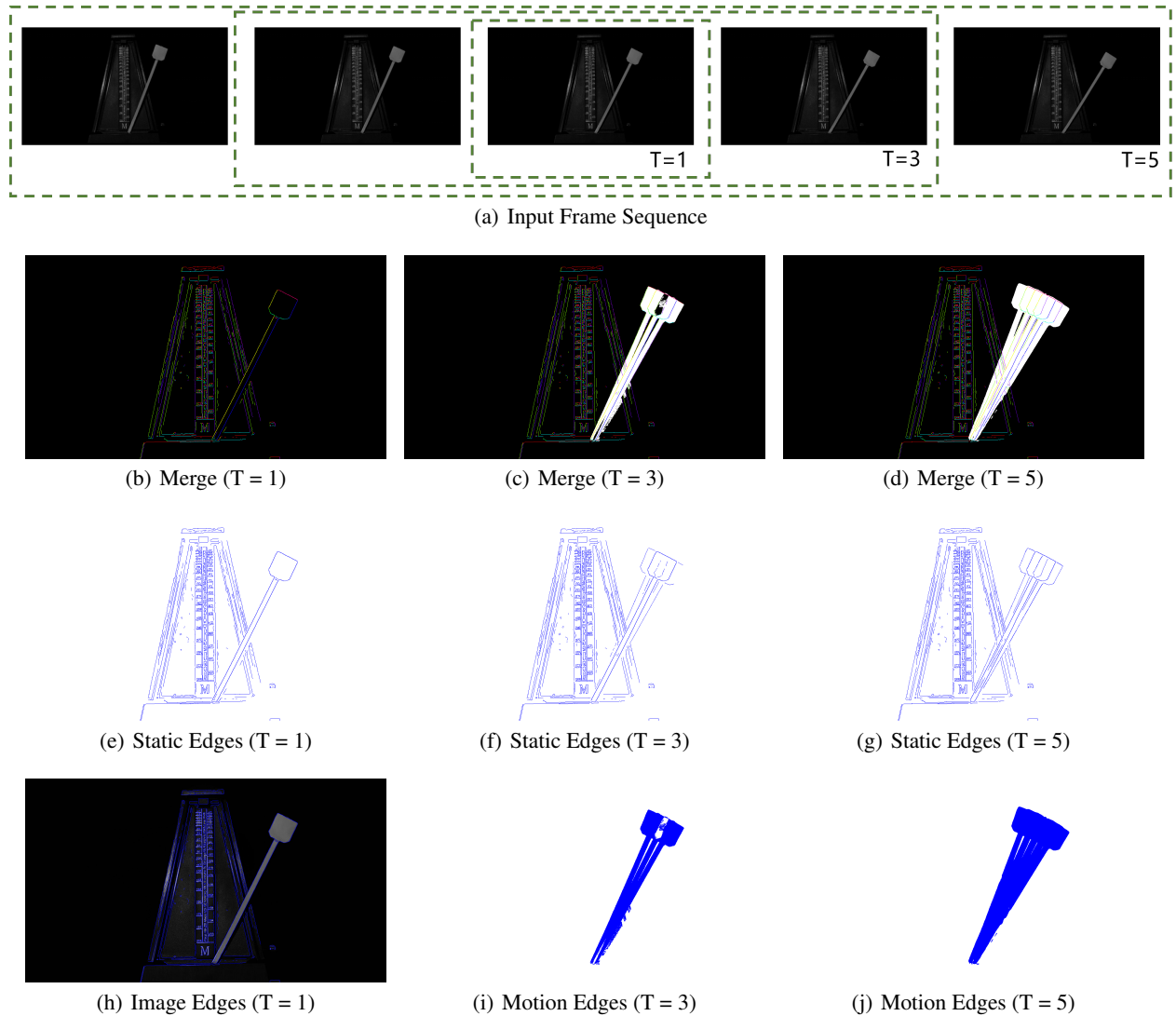


Figure 50: 3D Edge detection results: (a) Input frame sequence, where T represents the number of effective frames; (b-d) merged visualization via HSV space; (e-g) static edges; (h) static edges of the constant frame sequence are equivalent to image edges; (i-j) motion edges.

Finally, we deploy our algorithm to the  $xyz$  space rather than a video. Detection is performed on consecutive computerized tomography (CT) frames. Figure 52 demonstrates that the location as well as the changes in the organs are well detected. In the CT segment used for the experiment, the human exterior skin remains essentially unchanged, while the chest cavity volume changes (white area in subfigure h). The larger the white area, the greater the range of change and the faster the rate of change. Moreover, both the thoracic and lumbar spine show slight variations along the  $z$ -axis. It may be possible to deploy TGD to track changes in normal patients and use this information to identify abnormal patients. Characterizing changes in CT scans may provide potential benefits for medical diagnosis, which requires further collaborative research within various disciplines.

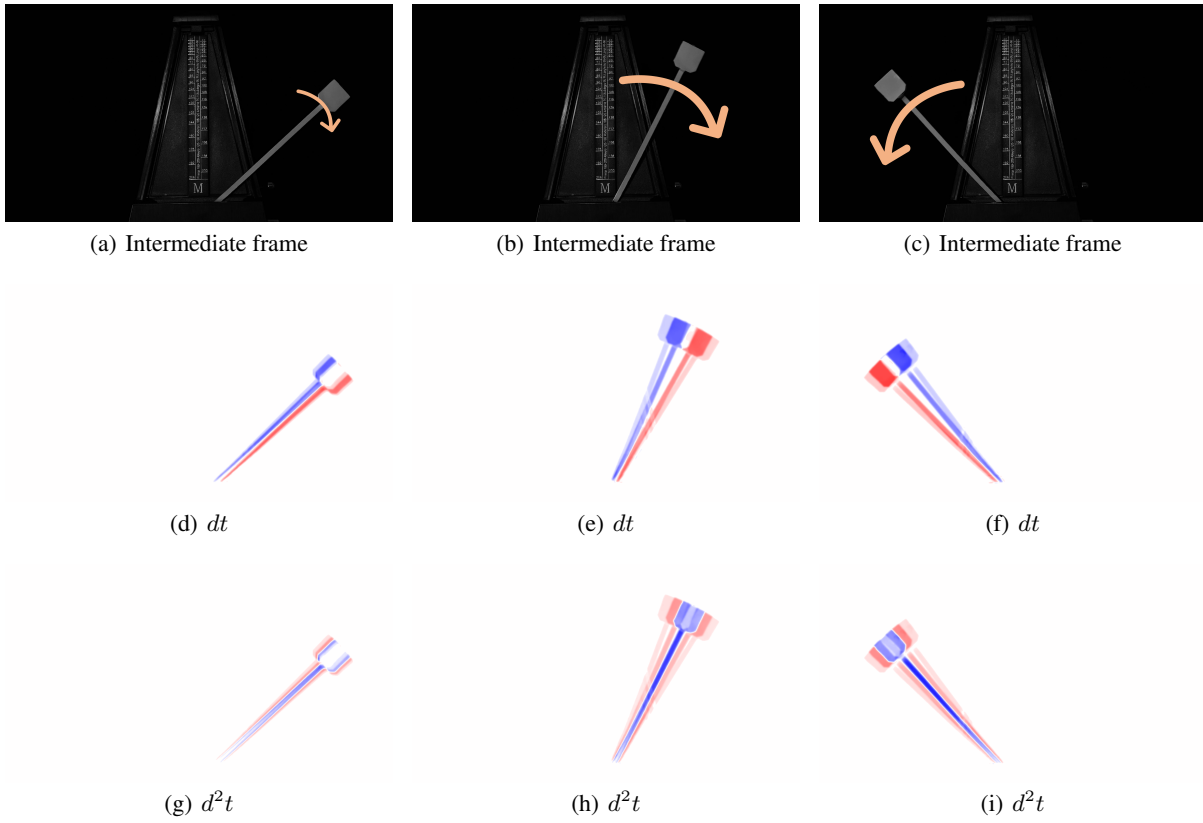


Figure 51: The correlation results of motion direction and partial TGD.

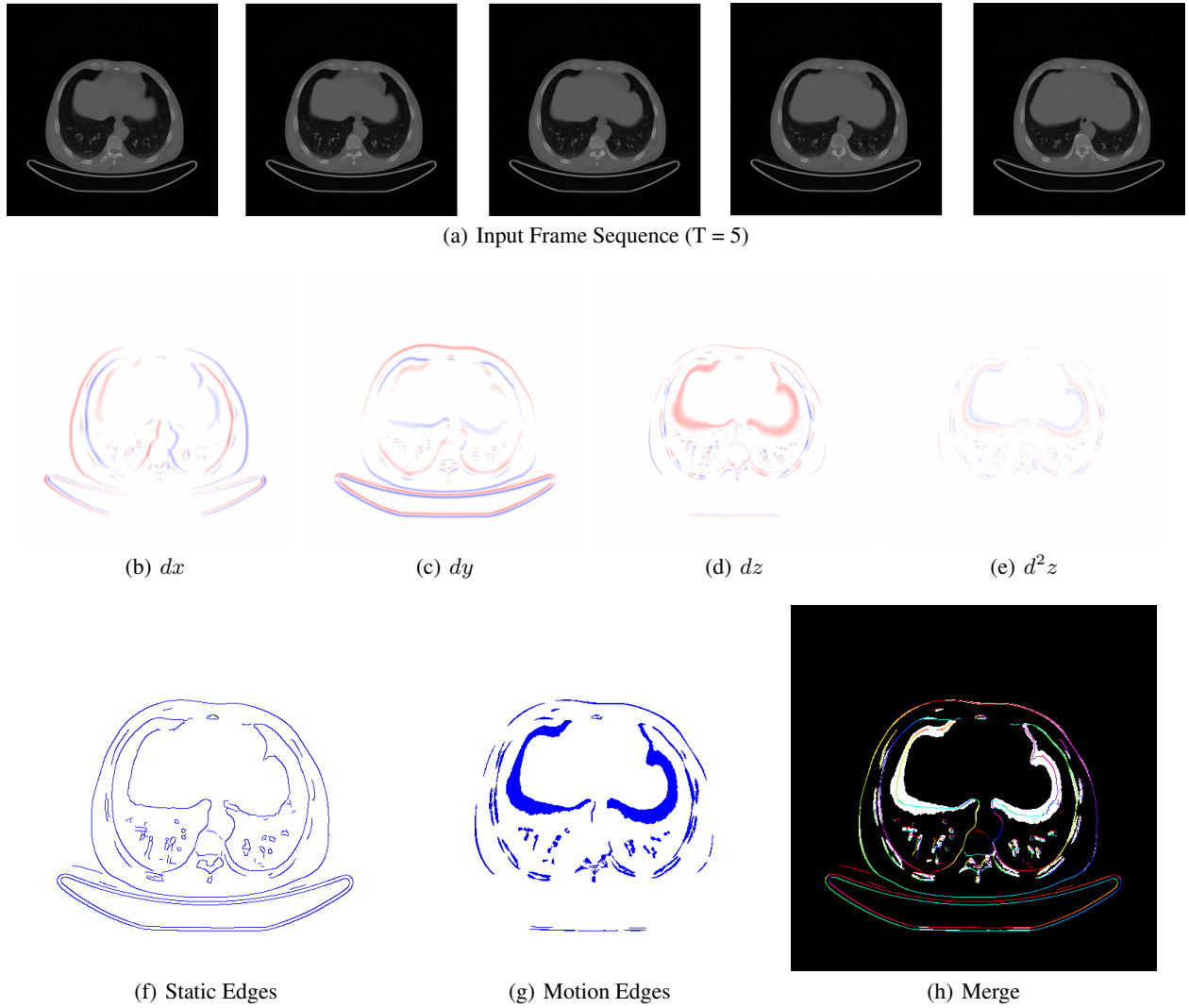


Figure 52: 3D Edge detection results: (a) Input frame sequence, where T represents the number of effective frames; (b-e) first- and second-order TGD; (f) static edges; (g) motion edges; (h) merged visualization via HSV space.

## 6 Conclusion and Outlook

Calculus is built upon the fundamental concepts of infinitesimal and limit. However, modern numerical analysis fails to conform to these basic concepts, that is, all calculations are discrete and have a finite interval. To address this issue, we begin by proposing the Tao Derivative, and subsequently derive Tao General Differential and Tao General Difference computed in a finite interval, collectively referred to as TGD. TGD can be realized by convolution, namely, Differential-by-Convolution and Difference-by-Convolution, which aligns with current numerical analysis practices.

We introduce multiple TGD operators and exhibit their exceptional performance through signal processing experiments, especially operators constructed by the orthogonal method that combines good performance and fast computation. Building upon the continuity principles of the first- and second-order TGD, we actively implement a single-layer one-dimensional convolution network and successfully reduce signal noise with satisfactory results. Likewise, two-dimensional TGD operators exhibit excellent performance in edge detection and noise suppression during image processing. Furthermore, three-dimensional TGD operators are capable of performing space-time coordinated analysis and can serve as a pioneering method in the field of numerical analysis.

TGD is developed based on the requirements of signal processing, and two constraints are also introduced according to these needs during deduction. Our extensive experiments have verified the excellent performance of TGD. From a mathematical point of view, there may be some lack of rigor in the discussion and deduction, and warrant further examination of the influence of Tao Derivative and General Differential on calculus. For instance, does the idea of transcending the bound of infinitesimal help in the integral? We anticipate that a more rigorous discourse and proof from mathematicians would advance the study of calculus in a finite interval. Additionally, we expect that our colleagues in the fields of numerical analysis, signal processing and computer vision will develop superior performing difference operators based on Tao General Difference, leading to greater advancement in numerical analysis.

## References

- [1] Ulisse Dini. *Fondamenti per la teorica della funzioni di variabili reali*. T. Nistri e C., Pisa, 1878.
- [2] Jonathan M. Borwein and Adrian S. Lewis. *Convex Analysis and Nonlinear Optimization: Theory and Examples*. Springer New York, NY, New York, 2 edition, 2000. Available online from <https://doi.org/10.1007/978-0-387-31256-9>.
- [3] C Lanczos. Applied analysis prentice hall. *New York*, 1956.
- [4] C. Lanczos. *Applied Analysis*. Dover Books on Mathematics. Dover Publications, 1988.
- [5] Charles W Groetsch. Lanczos' generalized derivative. *The American mathematical monthly*, 105(4):320–326, 1998.
- [6] Ginés R Pérez Teruel. A new class of generalized lanczos derivatives. *Palestine Journal of Mathematics*, 7(1):211–221, 2018.
- [7] Darrell L Hicks and Lorie M Liebrock. Lanczos' generalized derivative: insights and applications. *Applied mathematics and computation*, 112(1):63–73, 2000.
- [8] Andrej Liptaj. Maximal generalization of lanczos' derivative using one-dimensional integrals. *arXiv preprint arXiv:1906.04921*, 2019.
- [9] LM Milne-Thomson. The calculus of finite differences. *MacMillan and Co. Ltd., London*, 1933.
- [10] George Boole. *Calculus of finite differences*. BoD–Books on Demand, Paris, 2022. (Reprint of the original, first published in Cambridge, 1860).
- [11] Ronghua Li, Zhongying Chen, and Wei Wu. *Generalized difference methods for differential equations: numerical analysis of finite volume methods*. CRC Press, 6000 Broken Sound Parkway Northwest, 2000.
- [12] Sadri Hassani. Dirac delta function. In *Mathematical methods*, pages 139–170. Springer, 2009.
- [13] Tom M Apostol. *Calculus: one-variable calculus, with an introduction to linear algebrar*. Blaisdell Publishing, Waltham, 1967.
- [14] Michael Spivak. Calculus, publish or perish. *Inc., Houston, Texas*, 1994.
- [15] Robert Carmignani. Distributional inequalities and landau's proof of the weierstrass theorem. *Journal of Approximation Theory*, 20(1):70–76, 1977.
- [16] Arthur J Hallinan Jr. A review of the weibull distribution. *Journal of Quality Technology*, 25(2):85–93, 1993.
- [17] Horst Rinne. *The Weibull distribution: a handbook*. CRC press, 6000 Broken Sound Parkway Northwest, 2008.
- [18] Richard Courant and Fritz John. *Introduction to calculus and analysis I*. Springer Science & Business Media, 233 Spring Street New York, 2012.
- [19] Robert Wrede and Murray Spiegel. *Schaum's Outline of Advanced Calculus*. McGraw-Hill Education, 501 Bell Street Dubuque, 2010.
- [20] David Marr and Ellen Hildreth. Theory of edge detection. *Proceedings of the Royal Society of London. Series B. Biological Sciences*, 207(1167):187–217, 1980.
- [21] Hui Kong, Hatice Cinar Akakin, and Sanjay E Sarma. A generalized laplacian of gaussian filter for blob detection and its applications. *IEEE transactions on cybernetics*, 43(6):1719–1733, 2013.
- [22] Xin Wang. Laplacian operator-based edge detectors. *IEEE transactions on pattern analysis and machine intelligence*, 29(5):886–890, 2007.
- [23] Richard O. Duda and Peter E. Hart. *Pattern classification and scene analysis*. A Wiley-Interscience publication. Wiley, 111 River Street Hoboken, 1973.
- [24] Jerome A. Feldman, Gary M. Feldman, Gilbert Falk, Gunnar Grape, J. Pearlman, Irwin Sobel, and Jay M. Tenenbaum. The stanford hand-eye project. In Donald E. Walker and Lewis M. Norton, editors, *Proceedings of the 1st International Joint Conference on Artificial Intelligence, Washington, DC, USA, May 7-9, 1969*, pages 521–526, Burlington, 1969. William Kaufmann.
- [25] Azriel Rosenfeld. Review: B. jähne, h. haussecker, and p. geissler, eds., handbook of computer vision and applications. 1. sensors and imaging. 2. signal processing and pattern recognition. 3. systems and applications. *Artif. Intell.*, 120(2):271–273, 2000.
- [26] Tinku Acharya and Ajoy K Ray. *Image processing: principles and applications*. John Wiley & Sons, 111 River Street Hoboken, 2005.

- [27] Jeffrey S Simonoff. *Smoothing methods in statistics*. Springer Science & Business Media, 233 Spring Street New York, 2012.
- [28] XC Chen, Yu A Litvinov, M Wang, Q Wang, and YH Zhang. Denoising scheme based on singular-value decomposition for one-dimensional spectra and its application in precision storage-ring mass spectrometry. *Physical Review E*, 99(6):063320, 2019.
- [29] Rob J. Hyndman. Moving averages. In Miodrag Lovric, editor, *International Encyclopedia of Statistical Science*, pages 866–869. Springer, 233 Spring Street New York, 2011.
- [30] RM Clark. Non-parametric estimation of a smooth regression function. *Journal of the Royal Statistical Society: Series B (Methodological)*, 39(1):107–113, 1977.
- [31] Tom O’Haver. A pragmatic introduction to signal processing. *University of Maryland at College Park*, 2023.
- [32] George C Huang. Noise reduction by adaptive threshold in digital signal processing. In *1974 IEEE Electromagnetic Compatibility Symposium Record*, pages 1–7. IEEE, 1974.
- [33] Yves Meyer. *Wavelets and Operators: Volume 1*. Number 37. Cambridge university press, Shaftesbury Road Cambridge, CB2 8BS United Kingdom, 1992.
- [34] Carl Taswell. The what, how, and why of wavelet shrinkage denoising. *Computing in science & engineering*, 2(3):12–19, 2000.
- [35] Leonid I Rudin, Stanley Osher, and Emad Fatemi. Nonlinear total variation based noise removal algorithms. *Physica D: nonlinear phenomena*, 60(1-4):259–268, 1992.
- [36] Laurent Condat. A direct algorithm for 1-d total variation denoising. *IEEE Signal Processing Letters*, 20(11):1054–1057, 2013.
- [37] Jordan Frecon, Nelly Pustelnik, Nicolas Dobigeon, Herwig Wendt, and Patrice Abry. Bayesian selection for the 12-potts model regularization parameter: 1-d piecewise constant signal denoising. *IEEE Transactions on Signal Processing*, 65(19):5215–5224, 2017.
- [38] Ivan Selesnick, Alessandro Lanza, Serena Morigi, and Fiorella Sgallari. Non-convex total variation regularization for convex denoising of signals. *Journal of Mathematical Imaging and Vision*, 62(6-7):825–841, 2020.
- [39] Frank W Warner. *Foundations of differentiable manifolds and Lie groups*, volume 94. Springer Science & Business Media, 233 Spring Street New York, 1983.
- [40] Ryan Moore, Soundararajan Ezekiel, and Erik Blasch. Denoising one-dimensional signals with curvelets and contourlets. In *NAECON 2014-IEEE National Aerospace and Electronics Conference*, pages 189–194. IEEE, 2014.
- [41] Gregory Lee, Ralf Gommers, Filip Waselewski, Kai Wohlfahrt, and Aaron O’Leary. Pywavelets: A python package for wavelet analysis. *Journal of Open Source Software*, 4(36):1237, 2019.
- [42] David Marr. Early processing of visual information. *Philosophical Transactions of the Royal Society of London. B, Biological Sciences*, 275(942):483–519, 1976.
- [43] David Marr and Tomaso Poggio. A computational theory of human stereo vision. *Proceedings of the Royal Society of London. Series B. Biological Sciences*, 204(1156):301–328, 1979.
- [44] Vikram Mutneja Dharampal. Methods of image edge detection: A review. *J Electr Electron Syst*, 4(2), 2015.
- [45] John F. Canny. A computational approach to edge detection. *IEEE Trans. Pattern Anal. Mach. Intell.*, 8(6):679–698, 1986.
- [46] Vincent Torre and Tomaso A. Poggio. On edge detection. *IEEE Trans. Pattern Anal. Mach. Intell.*, 8(2):147–163, 1986.
- [47] Phillip A Mlsna and Jeffrey J Rodriguez. Gradient and laplacian edge detection. In *The Essential Guide to Image Processing*, pages 495–524. Elsevier, Amsterdam, 2009.
- [48] Steve R Gunn. Edge detection error in the discrete laplacian of gaussian. In *Proceedings 1998 International Conference on Image Processing. ICIP98 (Cat. No. 98CB36269)*, volume 2, pages 515–519. IEEE, 1998.
- [49] Steve R Gunn. On the discrete representation of the laplacian of gaussian. *Pattern Recognition*, 32(8):1463–1472, 1999.